1.1 mm Bolocam Observations of the Sunyaev Zel'dovich Increment in Abell 1835

by

Piers F. Horner

A thesis submitted to

Cardiff University

for the degree of

Doctor of Philosophy

October 2010

ProQuest LLC
789 East Eisenhower Parkway
P.O. Box 1346
Ann Arbor, MI 48106-1346

DECLARATION

This work has not previously been accepted in substance for any degree and is not being concurrently submitted in candidature for any degree.

Signed ..... Date 7th April 2011

STATEMENT 1

This thesis is being submitted in partial fulfilment of the requirements for the degree of PhD.

Signed ..... Date 7th April 2011.

STATEMENT 2

The work presented in this thesis is all my own and carried out under the supervision of Prof. Phil Mauskopf with the following exceptions: The SCUBA images presented in Chapters 8 and 9 were obtained by researchers at the JCMT, kindly provided by M. Zemcov. The subsequent analysis of the maps was carried out by myself with advice from M. Zemcov. A number of the figures in Chapters 2 and 8 are also reproduced from other papers. Where this is the case, the orginal source of the figures is fully cited.

Signed ..... Date 7th April 2011.

STATEMENT 3

I hereby give consent for my thesis, if accepted, to be available for photocopying and for inter-library loan, and for the title and summary to be made available to outside organisations.

Signed ..... Date 7th April 2011.

STATEMENT 4

I hereby give consent for my thesis, if accepted, to be available for photocopying and for inter-library loans after expiry of a bar on access previously approved by the Graduate Development Committee.

Signed ..... Date .....

ACKNOWLEDGMENTS

The work presented in this thesis could not have been completed without the support and guidance of a large number of people whose influence I wish to acknowledge here.

I would first like to thank my supervisor Professor Philip Mauskopf for the patience and support he has provided throughout my PhD. He has a broad and extensive knowledge of an impressive range of different topics in physics and astronomy which have provided the backbone to the project. His enthusiasm has been continuous, even during periods when my progress was achingly slow, and he has furnished me with a number of tremendous opportunities to learn and study in a range of amazing locations. The only small regret I have in this context was that the weather on Mauna Kea was *just* too good.

Acknowledgments need to be made to members of the Bolocam collaboration who have assisted in providing technical advice and critical reviews of this work at various stages. In particular I wish to thank Sunil Golwala; James Aguirre, and Jack Sayers for their support. A special mention should also be made of Mike Zemcov, who generously provided access to SCUBA data and help on analysis issues.

Thanks also to Simon Doyle who not only provided me with a computer (which I *have* used!), but has also been my continuous resource for LaTeX knowledge while writing, and who bailed me out on the Pampa la Bola. His willingness to offer help whenever it was required is a testament to Irish generosity.

I wish to thank the large number of people who have made my time studying in Cardiff so special and who have provided much needed human contact inside and outside department during and following long days spent in front of the computer. These include Paul Hargreaves; Nicola Whitehouse; Dmitry Morozov; Ben Connell (aka Fizzy McPhysics); Simon Morris; Vijay Krishnan; Giorgio Savini; Beverley Holman; Brian Patton; Sarah Roberts; Chris Dodd; Vanessa Stroud; all those who trained at Park Place TaeKwon Do; all those who worked at Nandos St. Davids 2 (in particular the management at the restaurant, who gave me every opportunity to take as much time off as was necessary to complete my writing). Last, but by no means least, thanks to all my friends in Act One, in particular Joy-Aisling (Flannegan) Brown and Rebecca Hill, without whom I don't know what state I would be in. This list is by no means exhaustive and there are no doubt people that I have forgotten to include. To those I have missed I offer my apologies - I can try to make it up to you somehow.

Finally, I wish to extend massive thanks to my parents Paul and Lucy Horner (as well as the *other* L&P). Without their love, support and encouragement over the past twenty-seven years I would never have made it this far. They have engendered me with a fascination and desire to understand all aspects of the Universe in which we exist that has guided me through my education. Just as importantly, they have taught me that education is fundamentally about the development of an individual, not just a means of gaining qualifications. To them I owe the biggest debt of gratitude.

ABSTRACT

Over recent years, there has been an increasing level of interest in the cosmological significance of observations of the Sunyaev Zel'dovich (SZ) effect in galaxy clusters. Although the SZ effect has been known about for around fifty years, observations of it have only become mainstream recently. The SZ effect refers to the redistribution of energy of Cosmic Microwave Background (CMB) photons due to inverse Compton scattering off populations of free electrons, most commonly in galaxy clusters. The SZ acts as an artificial 'emitter' or 'absorber' along the line of sight to a cluster once other backgrounds have been removed. SZ measurements suffer from a range of systematic effects that have made observations in the region of the spectrum where the SZ simulates an 'emitter' (above $\sim$ 220 GHz) particularly challenging. Nevertheless, the scientific potential of large-scale SZ surveys is large. In particular, the SZ distortion to the CMB is independent of redshift and limited only by the mass of the clusters being observed. This makes SZ surveys useful for making detailed observations of the evolution of large-scale structure of the Universe, which depends sensitively on cosmological parameters. Knowledge of the spectrum of the SZ effect can also be used to constrain the peculiar velocity of galaxy clusters, which has the potential to provide information about the nature of dark energy. This thesis describes the observation, mapping and detailed analysis of the cluster Abell 1835 at 1.1 mm, where the SZ acts as an 'emitter'. An estimate of the SZ emission from Abell 1835 is obtained and combined with other measurements of the cluster to generate a spectrum, from which one of the most precise limits on a cluster's peculiar velocity to date is obtained.

Contents

List of Figures

List of Tables

Chapter 1

Introduction

The discovery of the Cosmic Microwave Background (CMB) in 1965 by Penzias and Wilson [156] revolutionized our view of the Universe. It provided the most decisive evidence in support of the so-called Big Bang model of the Universe, in which the Universe initially existed in an extremely small, hot and dense phase before expanding into the cosmos we see today. Prior to the discovery of the CMB, there had been many years of controversy over the interpretation of observations by Vesto Slipher and, later, Edwin Hubble that appeared to imply that the Universe was expanding [101]. Two alternative explanations for the expansion were proposed: the Big Bang [1] theory, and the Steady-state hypothesis - in which it was proposed that the Universe had existed for an infinite time and that matter was continually being created in the regions of the Universe that were being evacuated during the expansion (e.g. [97]).

[1]The title of 'The Big Bang' was coined by Fred Hoyle - one of the original proponents of the alternative Steady State hypothesis - on the BBC radio programme 'Third Programme', broadcast in 1949. Although it is frequently claimed to have been used in a derogatory sense, Hoyle insisted that the term was used only to illustrate the concept more clearly for radio listeners.

One of the most striking features of the CMB is its extreme uniformity. In the original discovery paper, Penzias and Wilson report an excess noise of 3.5 ± 1.0K, which appeared to be isotropic and unpolarized to within the sensitivity of the instrument being used. This excess noise had been predicted by [59] as a signature of the Big Bang. Although Steady State theory also predicted a background of radiation, formed by the scattering of the light from stars by galactic dust, it was unable to account for the extreme uniformity of the CMB or the lack of appreciable polarization (which would be expected to be produced by scattering processes). This, along with a large body of evidence that supported the Big Bang theory over Steady-state (including, for example, the variation of radio source counts with distance and the observed abundance of the lighter elements Hydrogen, Helium and Lithium, which can be predicted accurately from Big Bang nucleosynthesis models), led to the Big Bang theory being adopted as the standard cosmological paradigm.

In 1992, results from Far-InfraRed Absolute Spectrophotometer (FIRAS) in the satellite COBE (Cosmic Background Explorer) demonstrated that the CMB spectrum was an almost perfect blackbody with temperature of 2.735 K [83, 136], while the Differential Microwave Radiometer (DMR) instrument on the same telescope measured variations in the CMB on the level of roughly one part in 100,000 [199]. These observations are viewed as the 'final' confirmation of the Big Bang scenario, since the near-perfect blackbody was very hard to reconcile with the Steady-state hypothesis, but had a natural explanation in the Big Bang theory, as radiation emitted when the Universe was extremely small and dense. The COBE results are also generally accepted to have represented the beginning of precision observational cosmology, which has subsequently become one of the biggest fields in current astrophysical research.

The uniformity of the CMB also appeared to confirm one of cosmology's most basic assumptions - the so-called 'cosmological principle' - which states that the Universe is homogenous and isotropic on large scales. A Universe that is completely homogenous, however, could never evolve into a structured Universe such as the one we see today. The variations found by COBE offer a way out of this conundrum. These 'anisotropies' in the CMB are believed to represent variations in the radiation density at the time of recombination (when the photons that make up the CMB were first released), which also map variations in the gravitational potential during that period.

It is currently believed that shortly after the Universe began it underwent a period of extremely rapid expansion, referred to as 'inflation'. Quantum mechanical variations in the distribution of all the constituents of the Universe were mapped onto 'large' scales as a result of this expansion, and seeded the variations in the matter distribution required to form large-scale structure (LSS). Although this inflation was very quick, it is thought to have only lasted for a brief period of time, after which the Universe is believed to have been reheated by some mechanism before continuing to expand (albeit at a far slower rate than during inflation).

At this time, the Universe was hot enough that simple atoms could not form, and the baryonic matter in it existed as a soup of free atomic nuclei; protons; neutrons, and electrons. Free electrons couple strongly to photons and, as a result, the early Universe is believed to have been opaque. This had the effect of 'trapping' photons in the regions in which they were produced. Once inflation had ended baryonic matter would have begun to fall into the gravitational potentials produced by variations in the dark matter density [2] , but the pressure from photons

[2]Dark matter is a form of matter thought to make up roughly 21% of the Universe's mass. As its name suggests, it is not thought to interact with light and so must be observed by the effects of its gravitational influence. The exact nature of this dark matter is not currently understood.

coupled to the baryonic matter would have resisted this collapse. The competing effects of gravitational collapse and photon pressure is expected to have set up acoustic oscillations in the baryonic matter that continued up to recombination, producing over-dense and under-dense regions on a varity of scales. At recombination the temperature of the Universe dropped below that required to ionize Hydrogen and the free electrons are expected to have combined with atomic nuclei to produce neutral atoms. As a result, the Universe became transparent over a short period of time and the support of photon pressure against gravitational collapse was removed. The large-scale structure we see in the Universe today could then begin to form.

Not only do the anisotropies in the CMB provide evidence for how structure may have formed in the Universe, it is also thought that the distribution of power from anisotropies on different scales (the so-called power spectrum of anisotropies) can tell us about fundamental parameters that characterize the Universe. The overall scale of the CMB power spectrum, for example, is thought to provide information about the curvature of the Universe. This is because the physical scale of the oscillations that correspond to peaks in the power spectrum can be predicted from the simple physical model discussed above and compared to its observed angular size (for a full discussion of the physics behind CMB anisotropies see [100] or [63]).

It is unsurprising, therefore, that research into the anisotropies of the CMB have been the main aim of observational cosmology in recent times. Studies of the CMB power spectrum by satellites such as the Wilkinson Microwave Anisotropy Probe (WMAP) [17] and the Balloon Observations of Millimetric Extragalactic Radiation and Geophysics (BOOMERanG) project [55] have precisely measured

the form of the CMB power spectrum up to multipoles $l \sim 500$. [3] Current missions, such as the Planck satellite, are set to map the CMB power spectrum at even higher resolution [212], and researchers have begun to study the polarization of CMB photons, which have the ability to tell us about so-called tensor fluctuations (gravitational waves) in the early Universe - a potentially important test of different inflationary models [99, 231] .

Increasing efforts are, however, now being made to study so-called 'secondary anisotropies' in the CMB which are not caused by acoustic oscillations in the early Universe. These anisotropies are, in general, a result of CMB photons interacting with matter during their passage through space following recombination (for a review, see [2]). Although the total background power spectrum (which refers to the power spectrum that is actually observed by an instrument, i.e. including contributions from the CMB as well as from sources of secondary anisotropies) is dominated at larger angular scales by CMB, secondary anisotropies can dominate at small scales.

Principal among these are anisotropies caused by the Sunyaev Zel'dovich (SZ) effect, which dominates the total background power spectrum for multipoles of $l \sim$ 2000 - 3000 and above. The effect was originally suggested by Rashid Sunyaev and Yakov Zel'dovich in the 1970's [204, 205] and occurs when CMB photons inverse Compton scatter off free electrons located in the inter-cluster medium (ICM) of galaxy clusters. The statistical probability of a CMB photon gaining energy during these interactions is found to be greater than the probability that it will lose energy. As a result, CMB photons interacting with a population of free electrons will experience a net redistribution of energy from lower to higher frequencies,

[3] multipole moments are a measurement of angular scale. Higher moments correspond to smaller angular scale. $l \sim 200$ corresponds to an angular scale of $\sim 1°$.)

resulting in a distortion of their spectrum.

The exact form of the distortion depends upon the velocity distribution of the electrons. Indeed, when the SZ effect was first proposed, it was regarded as one way of investigating the nature of the thermal distribution of electrons in clusters. It soon became clear, however, that this could be accomplished much better using X-ray observations. Indeed contemporary observations by, for example, the *Chandra* X-ray satellite have revealed that the structure of clusters can be extremely complicated. Gravitational interactions can strip gas from individual galaxies [130] (alternatively, see [114]), while 'cavities' created by radio jets have also been observed [193].

As the standard model of cosmology began to take shape, however, it became evident that the SZ effect could become a useful tool for cosmological research in at least two important ways.

Firstly, SZ and X-ray emission from a cluster can be used to produce an estimate of its angular diameter distance, D_A. This, combined with the redshift of the cluster, can then be used to deduce Hubble's constant, H_0, for a given form for the cosmological deceleration parameter, q_0 [23]. For a large sample of galaxy clusters at various redshifts it should, therefore, be possible to constrain the evolution of H_0 with with time, providing an independent means of testing the hypothesis that spacetime in recent epochs has been accelerating (an idea first proposed on the basis of studies of distant supernovae, e.g. [159]).

Secondly, one of the fundamental tests of our cosmological model is the evolution of large-scale structure (LSS) in the Universe, which is critically dependent upon the values of the cosmological parameters. Theoreticians have been successful

in recent years in conducting detailed computer simulations of structure formation in different cosmological scenarios (e.g. [200]). Ideally, these simulations should be compared to large catalogues of galaxies and galaxy clusters in order to constrain the values of the cosmological parameters based on observations. There are a number of methods of conducting such large scale surveys. Traditionally, these have been limited by flux, and so can only be complete to a certain redshift. Because the SZ is a distortion of the CMB spectrum however, it is expected that the surface brightness of the SZ will remain constant for a given mass cluster, independent of its distance from Earth. In theory, therefore, it should be possible for a particular SZ telescope to observe all clusters with mass above a specific threshold back to the surface of last scattering itself. There are at least two major benefits of such a survey:

1. The redshift coverage is much larger than traditional techniques, allowing a much greater period of the Universe's history to be explored and allowing a greater divergence between different cosmological models to become apparent;

2. The evolution of LSS can be characterised in terms of a mass function, $dn(M,z)/dM$, which describes the functional form of the comoving number density, n, of clusters with mass, M, at redshift, z. Since SZ surveys are limited by mass, therefore, they represent a much more natural means of constraining the mass function.

Large-scale surveys of clusters using the SZ effect therefore offer the potential to study the evolution of structure in greater detail than is currently possible.

The SZ effect from galaxy clusters in fact has two components: the thermal and kinematic SZ. The thermal component is the 'classical' SZ due to inverse Comp-

ton scattering of CMB photons off free electrons in the hot intracluster medium; whereas the kinematic component is due to the bulk motion of the clusters. These effects have to be separated in order to make the kinds of precision measurements required for the cosmological studies discussed above. In principal, this is possible since the thermal and kinematic effects have different spectra [4] . If a cluster is observed at a number of wavelengths, therefore, it should be possible to achieve this separation.

SZ observations suffer, however, from a number of systematic uncertainties. Early observations of the SZ were generally in the so-called 'decrement' region of the SZ spectrum, at frequencies below $\sim$ 220GHz. In this region of the electromagnetic spectrum, the number of photons being boosted to higher frequencies is greater than the number of photons being boosted from lower frequencies. Overall, therefore, the CMB intensity is reduced. In the decrement, systematic uncertainties - in particular confusion with other astrophysical sources - are generally lower. Observations of the SZ effect above 220 GHz suffer from a greater number of systematic issues, for example variations in a cluster's temperature profile due to internal structure of the type seen by *Chandra* (described above), and have only been attempted relatively recently. Observing the complete SZ spectrum is crucial to providing accurate estimates of the kinematic contribution, so that the potential for SZ surveys to limit cosmological parameters can be fully realised.

Observations of the kinematic effect are also of intrinsic interest, since they provide information on the velocity fields of clusters. These velocity fields are believed to be affected by the amount and nature of the dark energy in our Universe, and observations of the kinematic SZ are, therefore, expected to be an independent

[4] Although the kinematic effect has the same spectral form as the CMB, making *their* separation more difficult in single observations.

means of investigating this aspect of our Universe in detail.

This thesis describes the mapping of four clusters: Abell 1835; Abell 2218; Abell 851, and MS0451.6-0305 in the SZ, at a frequency of 273GHz, using the Bolometric Camera (Bolocam), mounted on the Caltech Submillimetre Observatory (CSO), and the subsequent detailed analysis of one of these clusters: Abell 1835. We derive an estimate of the thermal SZ from this cluster and combine this with observations of Abell 1835 made at other wavelengths to determine a form for the SZ spectrum for the cluster, from which we estimate its peculiar velocity. We also present results that characterize the point sources in the field, which are an important source of confusion in SZ observations.

The structure of this thesis is as follows: in Chapter 2 we outline the theoretical background to the SZ, discuss the scientific potential of studies of the SZ and review the methods and current status of SZ observations; in Chapter 3 we outline the observations used to obtain the data presented in this research; in Chapters 4 and 5 we discuss the development of a pipeline for reducing and mapping this data; in Chapter 6 we outline the analysis code written to extract characteristic fluxes from the sources in the science maps; in Chapter 7 we present the results of this analysis for Abell 1835 and discuss sources of error; in Chapter 8 we describe the combining of our results with those from other experiments to obtain an overall SZ spectrum for Abell 1835 and estimate the central Compton parameter and peculiar velocity of the cluster, and in Chapter 9 we discuss further work that could be carried out based upon our results and present our final conclusions.

Chapter 2

The Sunyaev Zel'dovich effect - theory and observation

The SZ effect was first proposed by Sunyaev and Zel'dovich in the early 1970's [204, 205]. Since then, the theory has become well-developed, and there are numerous reviews available in the literature [23, 36, 178]. The paper by Birkinshaw in particular is generally considered as one of the seminal reviews of the SZ effect and a significant amount of the theory in this chapter is derived from it. This chapter begins with an outline of the physics and mathematics that describe the interaction between a field of radiation and a population of free electrons, and the distortion of the radiation that results; this is followed by a general discussion of the thermal and kinematic SZ effects and the cosmological implications of SZ observations, and ends with a review of the techniques used to make observations of the SZ and of observations to date.

2.1 Photon-electron interactions

Radiation fields: specific intensity

A radiation field at position x can be generally described in terms of its specific intensity, $I(k, x, t)$. This quantity gives the amount of energy, dE, from the radiation field crossing an area element, dA, in the time interval dt from within solid angle, $d\Omega$, about the direction of the radiation, k, in the frequency interval, $d\nu$, as:

$$dE(k, x, t) = I(k, x, t) dA d\Omega d\nu dt \tag{2.1}$$

For a blackbody, the specific intensity is given by:

$$I = \frac{2h\nu^3}{c^2} \frac{1}{e^{h\nu/k_B T_{rad}} - 1} \tag{2.2}$$

where h is the Planck constant, k_B is the Boltzmann constant, c is the speed of light, and T_{rad} is the 'temperature' of the radiation field. The form of the blackbody function is shown in Fig. 2.1 for sources with different temperatures.

As discussed previously, the CMB radiation field is a near-perfect blackbody, and if CMB photons interact with matter their specific intensity may be altered. Following the notation of [23], the change in I is determined by the transport equation:

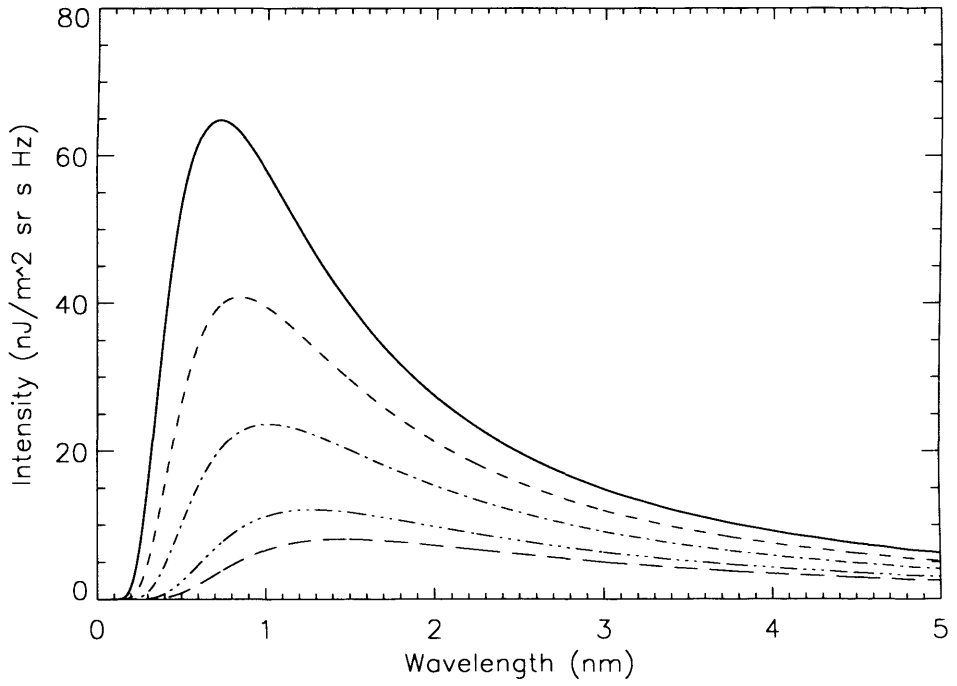

Figure 2.1: Spectra for blackbodies of different temperatures. At a given frequency, an object with a higher temperature will have a greater intensity. The temperature of the curves are: long-dashed line - 3500 K; long-dash long-dot - 4000 K; short-dash short-dot - 5000 K; short-dash - 6000 K, and solid line - 7000 K.

$$\frac{1}{c}\frac{\partial I}{\partial t}+\hat{\mathbf{k}}I = \int j(\nu)dl - \alpha_{abs}(\nu,\mathbf{k})I - \alpha_{sca}(\nu,\mathbf{k})I + \alpha_{sca}(\nu)\int \psi_\nu(\hat{\mathbf{k}},\hat{\mathbf{K}})I(\mathbf{K})d\Omega \quad (2.3)$$

where $j(\nu)$ represents the emissivity of the medium existing along the path the radiation traverses from emission to the observer (and the integral is performed over that path); $\alpha_{abs}(\nu)I_\nu$ represents the change in intensity due to absorption in that medium; $\alpha_{sca}(\nu)I_\nu$ represents the change in intensity due to scattering out of the line of sight, and $\alpha_{sca}(\nu)\int\psi(\hat{\mathbf{k}}),\hat{\mathbf{K}})I_\nu(\mathbf{K})d\Omega$ represents the radiation that is scattered *into* the line of sight from the rest of the field. $\psi_\nu(\hat{\mathbf{k}},\hat{\mathbf{K}})$ represents the 'scattering redistribution function' - i.e. the probability distribution that radiation will be scattered from the direction $\hat{\mathbf{k}}$ into the direction $\hat{\mathbf{K}}$.

It follows from (2.3) that there are a number of ways in which the specific intensity of a radiation field may change. Most relevant to SZ research are those due to scattering.

Compton scattering

Compton scattering is the quantum mechanical interaction of an electron with a photon. The change in wavelength, $\delta\lambda$, which results from Compton scattering differs from classical Thomson scattering, and is related to the change in direction of the photon by:

$$\delta\lambda = \frac{h}{m_e c}(1 - cos\theta) \quad (2.4)$$

where h, m_e and c represent the Plank constant; the mass of the electron, and the speed of light, respectively, and θ is the angle through which the photon scatters during the interaction.

Compton scattering arises in a wide range of different astrophysical situations. These include emission from Active Galactic Nuclei (AGN) and radio sources [16,98,102,189,196,197]; high energy photons from galaxy clusters [33,209]; pulsar and neutron star physics [10,129,167,168,228]; Gamma-ray bursters (GRBs) and supernovae [27,53,89,127,203,221,233], and solar physics [122,140]. [1] Compton scattering can also, however, be observed in lower-energy interactions, where the energy transfer is small. Inverse Compton scattering occurs when low energy photons interact with hot electrons. During this process, it is possible for the photon to gain energy rather than lose it, as happens in 'ordinary' Compton scattering. The physics of this process has been extensively examined (see e.g. [40], [226] and [207]), and is discussed below.

Individual photons-electrons interactions

The physical situation in which the SZ effect occurs involves CMB photons interacting with electrons with kinetic energy much larger than the photon energy. Although relativistic effects can become significant for detailed observations, it is generally reasonable to treat interactions between photons and electrons as virtually elastic, which leads to a number of simplifying assumptions in the mathematics.

Equation (2.4) for the Compton energy shift demonstrates that the change in the energy - or, equivalently, the frequency - of a photon is related to the change in

[1] Strictly, some of these physical situations involve inverse Compton scattering (see below). Research into the SZ effect is not included in this list.

direction of the photon during the scattering. The frequency shift during scattering can be represented by the dimensionless variable, s, defined as:

$$s = log\left(\frac{\nu'}{\nu}\right) \tag{2.5}$$

where ν and ν' represent the photon frequency before and after interaction in the reference frame of the electron. The probability of an electron moving with velocity, v, causing a shift in a photon's frequency, s is then defined as:

$$P(s|v)ds = \int p(\mu)d\mu\psi(\mu',\mu)\left(\frac{d\mu'}{ds}\right)ds \tag{2.6}$$

where μ and μ' are the cosines of the angles, θ and θ', which define the directions in which the initial and final photons move relative to some arbitrarily-defined axis; $p(\mu)d\mu$ is the probability of a photon scattering with angle μ, and $\psi(\mu',\mu)d\mu'$ is the probability that the photons scatters to angle μ'. Under the assumption of near-elastic collisions, it is found that these quantities can be expressed in terms of μ, μ' and the dimensionless velocity, $\beta = \frac{v}{c}$ using:

$$\begin{aligned} p(\mu)d\mu &= \frac{d\mu}{2\gamma^4(1-\beta\mu)^3} \\ \psi(\mu',\mu) &= \frac{3}{8}\left(1+\mu^2\mu'^2+\frac{1}{2}(1-\mu^2)(1-\mu'^2)\right) \end{aligned} \tag{2.7}$$

([23]), where $\gamma = (1-\beta^2)^{-1}$ is the Lorentz factor. μ and μ' can be related to

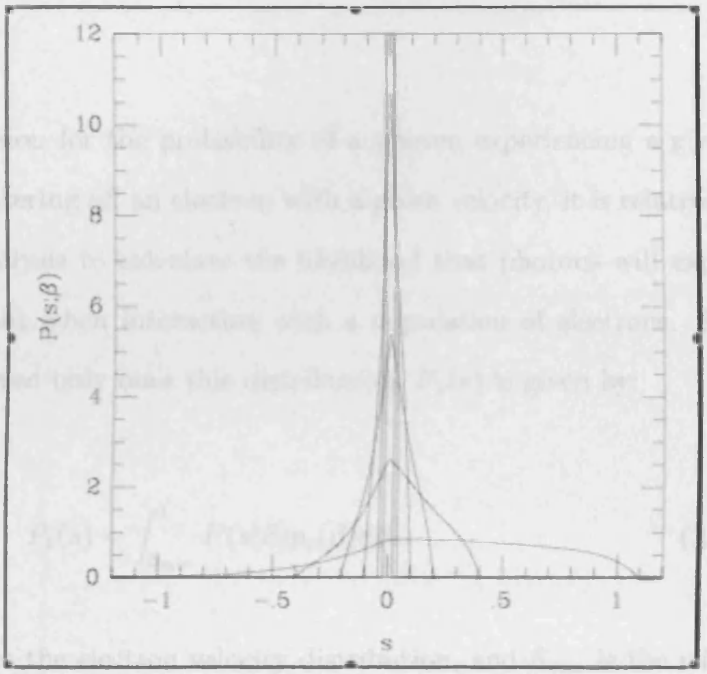

Figure 2.2: $P(s|\beta)$ calculated for a range of values of β: 0.01; 0.02; 0.05; 0.10; 0.20, and 0.50. The form becomes increasingly asymmetric as β increases. The asymmetry in $P(s|\beta)$ is what leads to the average energy shift during inverse Compton scattering being positive, which in turn leads to a redistribution of energy in the spectrum of the photons undergoing interactions. (Reproduced from [23])

one another by:

$$\mu' = \frac{e^s(1-\beta\mu)-1}{\beta} \tag{2.8}$$

[23,40,226]. Using these expressions (2.6) can then be evaluated. The resulting function for $P(s|\beta)$ is displayed in Fig. 2.2.

Interactions between populations of photons and electrons: full formalism

Once we have an expression for the probability of a photon experiencing a given shift in energy when scattering off an electron with a given velocity, it is relatively simple to extend the analysis to calculate the likelihood that photons will experience a given energy shift when interacting with a population of electrons. For photons that have scattered only once this distribution, $P_1(s)$ is given by:

$$P_1(s) = \int_{\beta_{min}}^{1} P(s|\beta) p_e(\beta) d\beta \tag{2.9}$$

where $p_e(\beta)$ describes the electron velocity distribution, and β_{min} is the minimum value of β required to generate a frequency shift, s. Although the upper limit of (2.9) is given as 1 ($v = c$), it is clear that one of the basic assumptions in the derivation of (2.9) is that the electrons involved in the interactions are, at most, only mildly-relativistic such that $p_e(\beta)$ would be expected to tail off towards relativistic values .

The form of (2.9) demonstrates the original motivation of the SZ effect. The form of $P_1(s)$ is strongly dependent upon the form of the electron thermal distribution, and could, in principal, be used to investigate which thermal distribution represents the best model for the gas in a cluster. A common feature of most realistic forms for $p_e(\beta)$, however, is that $P_1(s)$ is asymmetric about $s = 0$. This is demonstrated in Fig. 2.3. The degree of asymmetry increases with the electron temperature.

This result is fundamental to the SZ effect. If the form of $P_1(s)$ were symmetric

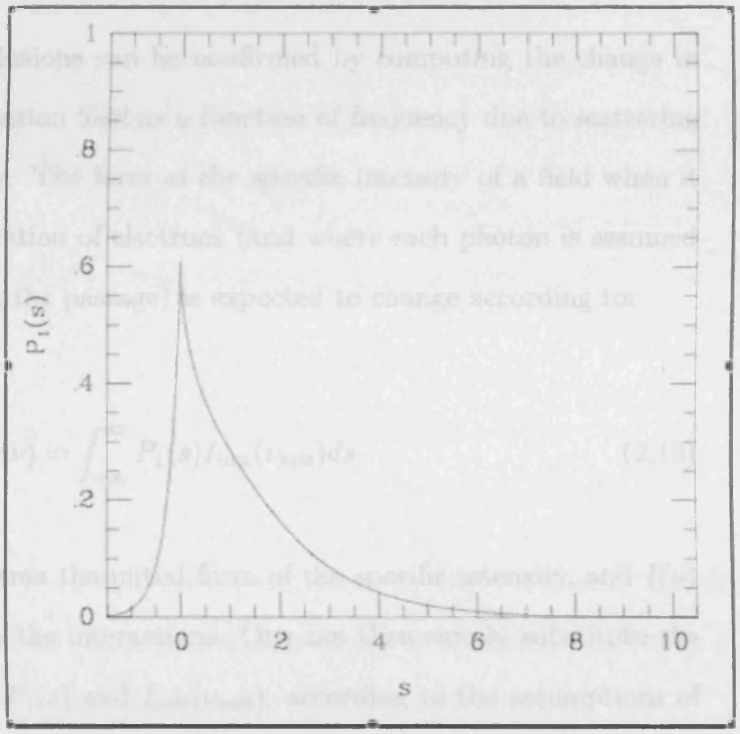

Figure 2.3: The form for $P_1(s)$, calculated for a power-law distribution of electron velocities. A strong upscattering tail is evident, and is more prominent than the equivalent form for a Maxwellian distribution. The key features of the forms for $P_1(s)$ derived for power-law and Maxwellian distributions are, however, similar.

then, on average, for every up-scattering (in which a photon gains energy), there should also be a down-scattering (where the photon loses energy), and there would be no overall change in the energy distribution of the interacting photons. The asymmetry, however, means that for a field of photons, it is expected there should be a redistribution of energy with the photons, on average, gaining energy. This leads to a distortion of the spectrum.

These qualitative conclusions can be confirmed by computing the change in intensity of an incident radiation field as a function of frequency due to scattering off a population of electrons. The form of the specific intensity of a field when it propagates through a population of electrons (and where each photon is assumed to interact only once during the passage) is expected to change according to:

$$I(\nu) = \int_{-\infty}^{\infty} P_1(s) I_{init}(\nu_{init}) ds \tag{2.10}$$

where $I_{init}(\nu_{init})$ represents the initial form of the specific intensity, and $I(\nu)$ is the specific intensity after the interactions. One can then simply substitute the appropriate expressions for $P_1(s)$ and $I_{init}(\nu_{init})$, according to the assumptions of the model, to obtain a form for $I(\nu)$.

In reality of course, photons could interact several times with electrons in a particular region, or may pass through without interacting at all. The probability that a single photon will interact with n electrons during its passage through a cloud of free electrons is given by the Poisson distribution:

$$p_n = \frac{\tau^n e^{-\tau}}{n!} \tag{2.11}$$

where τ is the optical depth of the electron cloud. The complete frequency redistribution function is then given by:

$$P(s) = e^{-\tau}\delta(s) + \sum_{i=1}^{N} \frac{\tau^i P_i(s)}{i!} \tag{2.12}$$

where the redistribution functions, $P_i(s)$ are obtained simply by:

$$\begin{aligned} P_2(s) &= \int P_1(s_1)P_1(s - s_1)ds_1 \\ P_3(s) &= \int P_1(s_1)P_1(s_2)P_1(s - s_1 - s_2)ds_1 ds_2 \end{aligned} \tag{2.13}$$

etc. [23].

It is also possible to express the full formalism in terms of Fourier transforms. In this case, the equation which governs the change in the specific intensity of the radiation field after interactions becomes:

$$I(\nu) = \int_{-\infty}^{\infty} P(s) I_{init}(\nu_{init}) ds \tag{2.14}$$

where $P(s)$ is now given as:

$$P(s) = \frac{1}{\sqrt{2\pi}} \int_{-\infty}^{\infty} \tilde{P}(k) e^{iks} ds \tag{2.15}$$

$\tilde{P}(k)$ is given by:

$$\tilde{P}(k) = e^{-\tau(\tilde{P}_1(k)-1)} \tag{2.16}$$

and:

$$\tilde{P}_1(k) = \frac{1}{\sqrt{2\pi}} \int_{-\infty}^{\infty} P_1(s) e^{-iks} ds \tag{2.17}$$

(see, e.g. [210]). The physical basis of this set of equations is the same as discussed previously, but the mathematics can, in certain circumstances, be simplified by using them.

In reality, the astrophysical environments in which the SZ effect arises have a very low optical depth, and it would rarely be required to extend $P(s)$ beyond the $P_1(s)$ term (or, equivalently, beyond terms that are linear in τ). Using this simplification, Rephaeli [178] demonstrates that the resulting change in specific intensity can be calculated according to:

$$\Delta I = I_{init}(x)\tau(\Psi(x,\zeta) - 1) \tag{2.18}$$

where the initial intensity spectrum, $I_{init}(x)$ is now defined in terms of the dimensionless frequency $x = h\nu/k_B T_{rad}$; $\zeta = mc^2/kT_e$, and the function Ψ is a complicated expression given by:

$$\Psi(x,\zeta) = A(\zeta)(\psi_1(x,\zeta) + \psi_2(x,\zeta)) \tag{2.19}$$

where the functions $\psi_1(x,\zeta)$, $\psi_2(x,\zeta)$ and $A(\zeta)$ are given by:

$$\psi_1(x,\zeta) = \int_0^1 \frac{t(e^x-1)dt}{e^{xt}-1} \int_{\beta_{min}}^1 \gamma e^{-\zeta(\gamma-1)} d\beta \int_{\mu_m}^1 \frac{\frac{1}{\beta^2}(3\mu^2-1)\left(\frac{1-\beta\mu}{t}-1\right)^2+3-\mu^2}{(1-\beta\mu)^2} d\mu \tag{2.20}$$

$$\psi_2(x,\zeta) = \int_0^1 \frac{(e^x-1)dt}{t^3(e^{xt}-1)} \int_{\beta_{min}}^1 \gamma e^{-\zeta(\gamma-1)} d\beta \int_{-1}^{\mu_M} \frac{\frac{1}{\beta^2}(3\mu^2-1)\left(\frac{1-\beta\mu}{t}-1\right)^2+3-\mu^2}{(1-\beta\mu)^2} d\mu \tag{2.21}$$

$$A(\zeta) = \frac{3}{32\int_0^1 \beta^2\gamma^5 e^{-\zeta(\gamma-1)} d\beta} \tag{2.22}$$

These expressions make use of the substitution $t = e^{-s}$. The limits in the expressions for $\psi_1(x,\zeta)$ and $\psi_2(x,\zeta)$ are found to be:

$$\beta_{min} = \frac{1-t}{1+t} \tag{2.23}$$

$$\mu_m = \frac{1-t(1+\beta)}{\beta} \tag{2.24}$$

and

$$\mu_M = \frac{t-1+\beta}{t\beta} \tag{2.25}$$

[178].

Interactions between populations of photons and electrons: the Kompaneets approximation

The theory described so far was originally outlined by Wright in [226] and further developed by Rephaeli [178]. The original work on the SZ effect made use of further simplifications to the mathematics, obtained by using the so-called Kompaneets equation [121]:

$$\frac{\partial n_\gamma}{\partial y} = \frac{1}{x_e^2}\frac{\partial}{\partial x_e} x_e^4 \left(\frac{\partial n_\gamma}{\partial x_e} + n_\gamma + n_\gamma^2 \right) \tag{2.26}$$

to calculate the change in specific intensity. In (2.26), $n_\gamma(\nu)$ is the occupation number of photons at a given frequency ν; $x_e = h\nu/k_B T_e$ is a dimensionless frequency, and y is the 'Compton range', more commonly referred to as the 'Compton parameter'. For a radiation field passing through a cloud of electrons, y takes the form:

$$y = \int n_e \sigma_T \frac{k_B T_e}{m_e c^2} dl \tag{2.27}$$

where n_e is the electron number density along the light's path; σ_T is the Stefan-Boltzmann constant, and the integration takes place along the line-of-sight through the cloud. Using the Kompaneets equation, the change in the specific intensity due to scattering is given by:

$$\Delta I(x) = I_0 y g(x) \tag{2.28}$$

where $I_0 = \frac{2h}{c^2}\left(\frac{k_B T_{rad}}{h}\right)^3$, x is a dimensionless variable defined by $x = h\nu/k_B T_{rad}$ (where T_{rad} is the effective temperature of the CMB radiation), and the spectral form of the intensity change, $g(x)$, is given by:

$$g(x) = \frac{x^4 e^x (x\coth(x/2) - 4)}{(e^x - 1)^2} \tag{2.29}$$

The Kompaneets equation is strictly an approximation, since it governs the behaviour of diffusion processes rather than scattering events. Furthermore, it does not take into account relativistic effects during the scattering, which the full formalism described above does. Nevertheless, the approximation is commonly used in SZ research. Its popularity is due primarily to the fact that it gives a simple analytic expression for the change in specific intensity, rather than the more complicated form described previously (see (2.18) - (2.25)). The amplitude of the intensity change in these sets of equations is a complicated function of τ and T_e, whereas in the Kompaneets form, it depends only on the Compton parameter y, which has a relatively simple relationship to τ and T_e (see (2.27)).

The characteristic features of the spectral form of the SZ effect are also independent of the electron temperature in the Kompaneets form, whereas they are dependent upon the electron temperature in the full treatment. For example, the position of the null - the point where the SZ spectrum crosses the frequency axis - which is important to the measurement of the kinematic SZ effect (see below), is found to be at $x = 3.83$ ($\nu = 217$GHz) using the Kompaneets form whereas, for the full treatment, its position depends on T_e according to:

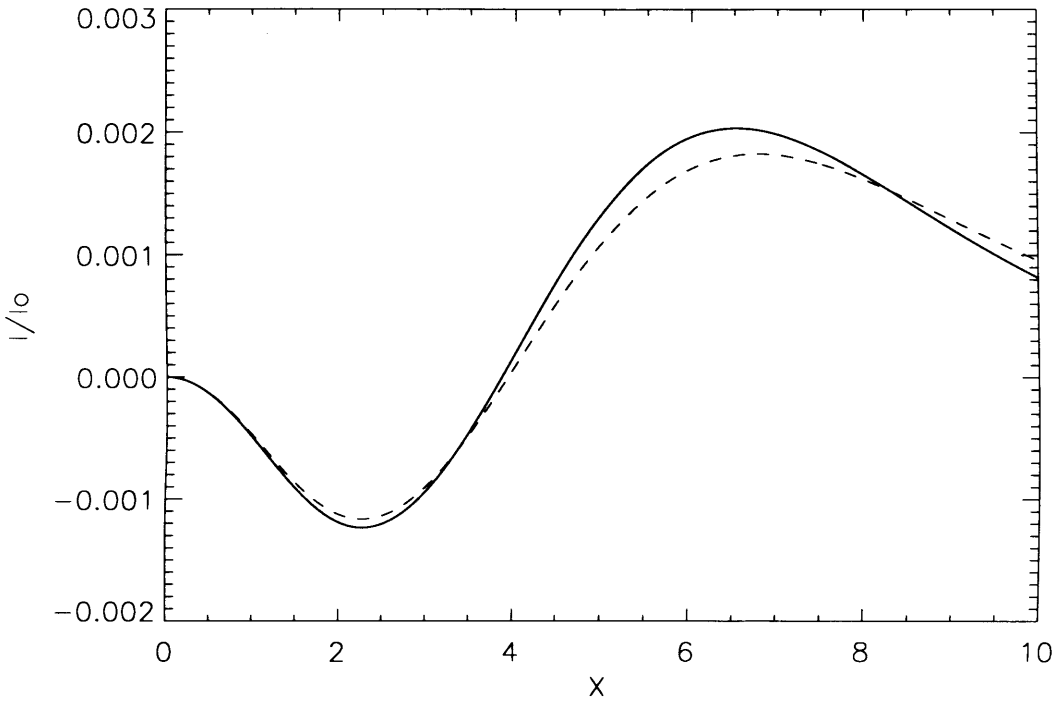

Figure 2.4: SZ spectrum *without* relativistic corrections (solid line), and *with* corrections. The models were generated using an electron temperature $\sim$ 8keV, and central Compton parameter $y_0 \sim 4 \times 10^{-4}$.

$$x \approx 3.83 \left(1 + \frac{k_B T_e}{mc^2}\right) \tag{2.30}$$

[178].

A significant amount of work has been carried out to find analytical approximations to express relativistic corrections to the SZ effect, as calculated using the Kompaneets equation (e.g. [39], [105] and [202]). These corrections are generally expressed in terms of a power series of the variable $\theta_e = k_b T_e / mc^2$. Using the corrections in [105] the intensity change, including terms up to fourth order in θ_e, can be expressed as:

$$\Delta I = \frac{I_0 y x^4 e^x}{(e^x - 1)^2}(Y_0 + \theta_e Y_1 + \theta_e^2 Y_2 + \theta_e^3 Y_3 + \theta_e^4 Y_4) \tag{2.31}$$

(where we note that, according to (2.27) and our definition of θ_e above, $y = \theta_e \int \sigma_T n_e dl$). An example of the effect of these corrections is demonstrated in Fig. 2.4. The co-efficients of the power series are complex functions of x. The Y_0 term is given by:

$$Y_0 = -4 + x\coth(x/2) \tag{2.32}$$

(which recovers the non-relativistic form for the SZ effect). Expressions for the higher order coefficients are given in full in Appendix A.

For a cluster temperature of $\sim$ 8 keV [147] find these corrections to be accurate at the percent level.

2.2 Applications of the SZ

2.2.1 Astrophysical Environments: Galaxy Clusters

The processes described so far are generally applicable for any field of radiation passing through a population of free electrons. The SZ effect refers specifically to the distortion of the CMB spectrum by free electrons. There are a number of different environments in which this distortion can take place. Of most importance cosmologically, however - and the environments in which the SZ effect is usually studied - are galaxy clusters.

Galaxy clusters are believed to represent the largest virialized structures in the Universe and represent mass structures of order 10^{14} $M_{\odot}$ or more. In the simplest cases, these clusters are assumed to be in hydrostatic equilibrium, where the internal pressure of the gas in the cluster balances its gravitational contraction:

$$\frac{dP}{dr} = -\frac{GM(r)\rho(r)}{r^2} \tag{2.33}$$

where $M(r)$, $P(r)$ and $\rho(r)$ are the mass of gas contained within a radius r from the cluster centre; the pressure at r, and the density at r, respectively, and G is the gravitational constant.

Based on this, the gas in clusters is believed to reach a temperature of 10^7 - 10^8K , which is hot enough to ionize hydrogen. The inter-cluster (IC) gas is, therefore, expected to have a large number of free electrons available to scatter CMB photons. The density of these electrons is, however, low enough that the mean free path of photons through clusters is large, and the optical depth correspondingly low.

It is clear, therefore, that the electron gas in clusters should be capable of producing a significant SZ effect of the type described above. The physical processes that have been described so far are referred to as the 'thermal' SZ (tSZ) effect. There is, however, another type of SZ effect which results from the bulk movement of the electrons in the cluster as a whole in relation to the CMB. This is referred to as the 'kinematic' or 'kinetic' SZ (kSZ) effect.

The form of the kinematic effect can be obtained from (2.3). The occupation number of CMB photons is given simply by:

$$n_\gamma(\nu) = \frac{1}{e^{h\nu/k_B T_{rad}} - 1} \tag{2.34}$$

In the reference frame of the moving cluster, however, this becomes:

$$n'_\gamma(\nu) = \frac{1}{e^{x_{cl}\gamma_{cl}(1-\beta_{cl}\mu_{cl})} - 1} \tag{2.35}$$

where β_{cl} and γ_{cl} refer to the dimensionless velocity and Lorentz factor of the cluster; μ_{cl} gives the direction of the incoming photon in the frame of the cluster, and $x_{cl} = h\nu_{cl}/k_B T_{cl}$, with ν_{cl} and T_{cl} the frequency and temperature of the photon in the reference frame of the cluster [2] .

Using these results, the change in specific intensity due to the kSZ is found to be:

$$\Delta I = x^3 I_0 \tau \int_{-1}^{1} \frac{3}{8}(1+\mu_{cl}^2)\left(\frac{e^x - 1}{e^{\tilde{x}} - 1} - 1\right) d\mu_{cl} \tag{2.36}$$

where $\tilde{x} = x\gamma_{cl}^2(1+\beta_{cl})(1-\beta_{cl}\mu_{cl})$, and $x = h\nu/kBT_{rad}$, as before [23].

Simulations of cluster peculiar velocities in a high-density Universe predict an r.m.s. peculiar velocity of 300 kms^{-1} [84], i.e. β_{cl} of order 10^{-3}. In this case, (2.36) can be expanded and simplified, then integrated to obtain:

$$\Delta I = -\frac{v_p}{c}\tau I_0 h(x) \tag{2.37}$$

[2] T_{cl} is related to T_{rad} simply by: $T_{cl} = T_{rad}(1+z)$, where z is the redshift of the cluster, while the transformed frequency is given by: $\nu_{cl} = \gamma_{cl}(1+\beta_{cl})\nu$, where ν is the frequency of the photon in the reference frame of the CMB.

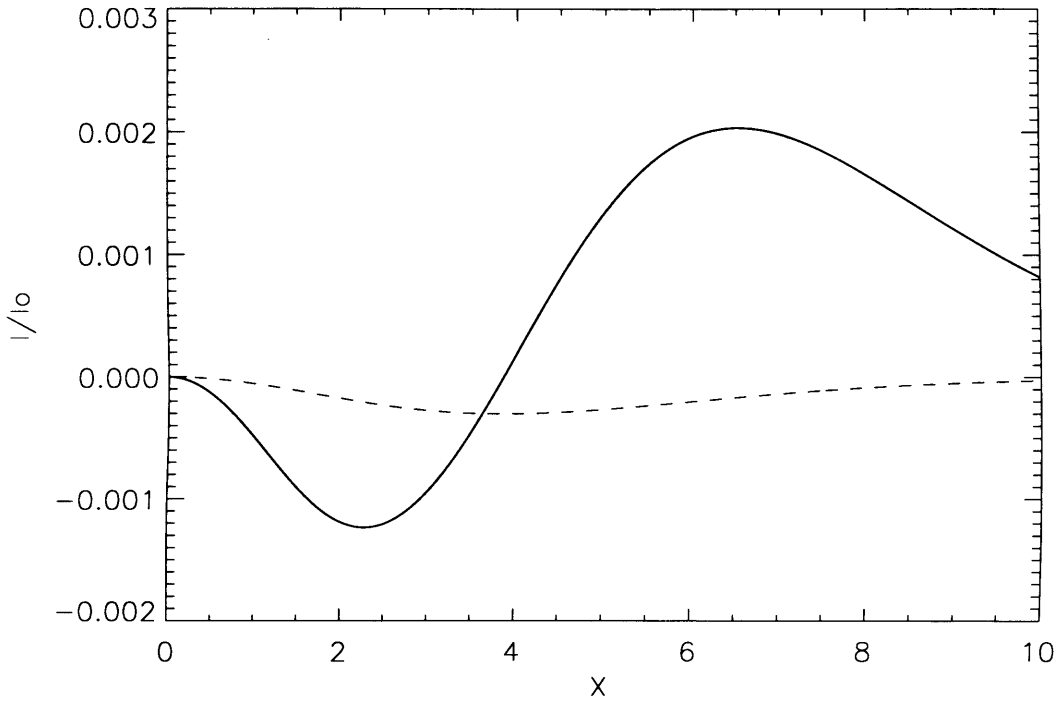

Figure 2.5: The thermal and kinematic SZ effects, calculated for a cluster with $y_0 = 3 \times 10^{-4}$ and $v_p = 1000\text{kms}^{-1}$. The thermal contribution is clearly dominant over the kinematic effect, except for frequencies around 220 GHz ($x \sim 3.8$), where $g(x) \rightarrow 0$.

with v_p the peculiar velocity of the cluster; and $h(x)$ given by:

$$h(x) = \frac{x^4 e^x}{(e^x - 1)^2} \tag{2.38}$$

and the optical depth can be related to the Compton parameter according to:

$$\tau = \frac{y}{\theta_e} \tag{2.39}$$

Examples of the forms for the thermal and kinetic SZ are given in Fig. 2.5. The kSZ effect is generally relatively small compared to the tSZ, but can come to

dominate around the null of the thermal effect (where $g(x) \rightarrow 0$).

The kSZ and tSZ effects have significantly different spectral forms. It should, therefore, be possible to separate the two with suitable multi-frequency data, and this has the potential to constrain the peculiar velocity of the cluster using (2.37). This data, as well as being of intrinsic interest, can provide important limits on cosmological parameters (see below).

Even though the SZ was first proposed as a means of investigating the thermal state of IC gas [88], its application to studying galaxy clusters was originally neglected, since X-ray astronomy is capable of studying cluster atmospheres with much greater sensitivity and resolution. Recently, however, the SZ has been used once more to provide estimates of cluster parameters. One such application is the measurement of the gas mass enclosed by a telescope beam in an SZ observation. This works since, for an isothermal cluster, the surface mass density of gas in a cluster along a given line of sight is defined by:

$$\Sigma_{gas} = \int n_e \mu_e dl \tag{2.40}$$

where μ_e is the mean mass of gas per electron along that line of sight.

It is obvious from (2.27), therefore, that a relationship can be derived between Σ_{gas} and y:

$$\Sigma_{gas} = \mu_e \left(\frac{m_e c^2}{k_B T_e} \right) \frac{y}{\sigma_T} \tag{2.41}$$

[23, 144]. This can be compared to the virial mass of the cluster, calculated

using the electron temperature of the cluster and assuming hydrostatic equilibrium (or, alternatively, using the integrated SZ signal, which is thought to be sensitively related to the cluster mass [see below]) to provide an estimate of the cluster gas mass fraction, f_g.

Where clusters exhibit lensing, an independent form of this measurement can be made by comparing the gas mass to the estimated gravitational mass, determined from the lensing. The gas mass fraction provides, therefore, a direct comparison between the gravitational and baryonic mass in the cluster. X-ray observations can be used for a similar purpose, but, due to their sensitivity to cluster physics, are limited far more by, for example, uncertainties in the clumping of the cluster gas.

There is a substantial amount of literature which discusses the future observational power of the SZ as a tool for studying cluster physics (for a review, see [24]). Much of this relates to the theory of how clusters form. [176] outline how SZ observations can be used to estimate the gas potential, thermal energy and mass of clusters. Combining SZ observations with observations at other wavelengths also has the potential to over-constrain gas density and cluster temperature profiles.

The integrated SZ signal, defined by:

$$Y = \int y(\tilde{n}) d\Omega \tag{2.42}$$

(where $y(\tilde{n})$ is the Compton parameter along the line of sight defined by the vector $\tilde{n}$, and the integration is over the entire cluster), is found to be proportional to the thermal energy of the inter-cluster medium (ICM) (e.g. [12, 176]).

This distinguishes SZ from X-ray observations, since the SZ is capable of probing the thermal history of a cluster, whereas X-ray observations are more suited to investigating the density of ICM gas. Galaxies in the early phase of their development are likely to have a large thermal energy and may be, therefore, be detectable with the next generation of SZ telescopes.

Following this line of research, it is also thought (see e.g. [78, 79]) that the development of massive spheroidal galaxies, bulges and active galactic nuclei involve significant feedback between quasars and their surrounding galaxies. This feedback involves an injection of thermal energy into the inter-galactic gas, which should be visible as an SZ signal [13, 41, 42, 57, 124, 164, 184]. Indeed, it is possible that these sources may be capable of accounting for an excess of arcminute scale fluctuations observed at 30 GHz by different groups (see [134] and [54]).

As emphasized by [23], the SZ effect in combination with X-ray observations has the potential to provide information on the 3-dimensional shape of clusters, clumping and the thermal structure of a cluster (see also [46]). Furthermore [144] point out that the SZ effect can be used as a measure of the projected mass of gas in the cluster along the line of sight (although this assumes a simple temperature structure of the cluster). The SZ is also expected to be capable of investigating non-thermal populations of electrons in clusters [47]; hot gas in the outer regions of galaxy groups [139]; radio lobes and plasma bubbles [45, 161]; cluster cavities [43], and cool cores [162].

As a precursor to these kinds of high resolution SZ observations, [116] have conducted a multifrequency analysis of the cluster RX J1347-1145 with the highest resolution SZ and X-ray images available at the time. Among their results, the authors report the detection of a high temperature (> 20 keV) subclump, which

is interpreted as an indication of a recent merger, demonstrating the potential of future SZ research.

Finally, there has been a significant amount of research into scaling relationships between cluster properties and the SZ signal from clusters (e.g. [52,176,230]). The form of these scaling relationships have the potential to constrain the evolution of galaxy clusters, as well as provide mass estimates for cluster SZ surveys (see below).

2.2.2 Cosmological Applications of SZ

Hubble Constant

By far the most common context in which the SZ effect is currently discussed, however, is that of cosmology (for reviews, see e.g. [36, 179]). Originally, interest in the usefulness of the SZ effect was reinvigorated by the prospect that it could be used to make independent measurements of the Hubble constant, H_0 (see, e.g. [26, 37, 82, 94, 195]). The principle behind this is that X-ray and SZ intensity measurements can both be expressed in terms of integral along the line of sight through a cluster. Whereas the SZ intensity can be expressed as:

$$I_{SZ}(x) = \int n_e \Psi(x, T_e) dl \tag{2.43}$$

where $\Psi(x, T_e)$ represents the spectral form of the SZ, the X-ray surface brightness, b_X, is given by:

$$b_X = \frac{1}{4\pi(1+z)^3} \int n_e^2 \Lambda_e dl \tag{2.44}$$

where Λ_e is the X-ray spectral emissivity of the cluster gas, and z is the cluster redshift [23]. It follows that the combination I_{SZ}^2/b_X is a density-weighted measure of the photon's path length through the cluster. This can be combined with measurements of the angular size of the cluster on the sky, as well as assumptions or measurements of the cluster gas profile (orientation, symmetry, etc), to obtain an estimate of the angular diameter distance, D_A, of the cluster. This quantity is related to the Hubble constant via:

$$D_A = \frac{c}{H_0 q_0^2} \frac{q_0 z + (q_0 - 1)(\sqrt{1+2q_0 z} - 1)}{(1+z)^2} \tag{2.45}$$

where q_0 is the so-called deceleration parameter, defined by:

$$q_0 = \frac{1}{2}(1+3\omega)\left(1 + \frac{k}{a^2 H_0^2}\right) \tag{2.46}$$

where ω is the equation of state of the Universe; k is the curvature of the Universe, whose value is determined by whether the Universe is closed, flat or open, and a is the scale factor of the Universe. It is also worth noting that q can be written in terms of H_0 and its derivative with respect to time, $\dot{H}_0$:

$$q = -\left(1 + \frac{\dot{H}_0}{H_0^2}\right) \tag{2.47}$$

The form for D_A in 2.45 specifically assumes that the cosmological constant

is zero [23].

Estimates of H_0 from multi-wavelength SZ and X-ray observations, however, suffer from a number of systematic issues. One potential bias is that X-ray catalogues may suffer a selection bias if the gas in the cluster is not spherically symmetric. If the cluster gas is aspherical, clusters which are oriented with the major axis of their gas distribution in the direction of the observer will appear brighter and are more likely to be selected. These clusters are also expected to underestimate H_0 by a factor that relates to the degree of asymmetry of the core of the cluster [23]. Although there are ways to avoid this selection bias, it has been pointed out that the clusters that have been studied so far in an attempt to derive estimates of H_0 are, because of the relatively young nature of the SZ field, also those which have bright X-ray emission, and so are more likely to suffer from this effect.

Further errors can be incurred because of uncertainties in the temperature and density structure of the clusters being observed. The sources of these uncertainties include: discrepancy between the profile parameters appropriate for the SZ and X-ray observations (since SZ and X-ray emission depend upon the density distribution of gas in clusters in different ways); clumping in the gas, and the isothermal assumption. It is estimated (e.g. [104, 229]) that such effects could contribute an error of up to $\sim$ 20 - 30% in the estimates of H_0. [220] also consider the effect of asphericity in the cluster gas distribution upon the estimate of H_0 and conclude errors of up to 5% are possible for realistic models. For a further discussion of systematic uncertainties in the estimates of the Hubble Constant using the SZ effect, see [113].

Finally, contamination of the SZ and X-ray signal may also generate errors in the estimates of H_0. These may arise, for example, due to emission from the

CMB; emission from the kinetic SZ; point and radio sources in the field, and from emission due to non-thermal and relativistic electrons. It is estimated that they could, once again, affect estimates on the level of $\sim 10\%$ [23].

Despite these complications, values for D_A and H_0 have been obtained using this method by a number of experiments (see e.g. [14, 23, 26, 137, 171, 214, 215]). The results are, in general, reasonably consistent with recent satellite estimates (e.g. the 5-year data from the Wilkinson Microwave Anisotropy Probe, WMAP, obtains a value of $71.9^{+2.6}_{-2.7}\ kms^{-1}Mpc^{-1}$). Other groups have used adaptations of the basic technique to estimate H_0. [51] employ a joint analysis which examines the combined SZ/ X-ray data with baryon acoustic oscillations (BAO) to obtain a value of $74^{+4}_{-3.5}\ kms^{-1}Mpc^{-1}$ (the errors for which do *not* include systematic uncertainties), based on data from 25 clusters. [192] use X-ray observations to 'refine' the SZ signal from three clusters. Based on this, they obtain a measurement of $69 \pm 8\ kms^{-1}Mpc^{-1}$.

CMB contamination

More recently, with the advent of projects capable of observing large numbers of clusters at millimetre wavelengths, attention has turned to examining the potential of large-scale SZ surveys to constrain other cosmological parameters. Signal from the SZ on large angular scales has two major implications for this kind of research.

First, the SZ acts as a source of contamination of the CMB, and can, therefore, potentially affect the estimates of cosmological parameters derived from CMB experiments such as WMAP and BOOMERanG. In principle, the spectrum of the SZ effect is unique and can, with sufficient frequency coverage, be extracted

cleanly during data processing. Indeed, studies of the SZ effect can be based on this extraction (see, e.g. [103, 219], who estimate σ_8 from WMAP data). WMAP, for example, has five observing channels, at frequencies between 23 and 94 GHz (e.g. [17]). Nevertheless, it is possible for contamination from the SZ to remain in CMB maps [48].

Early estimates of this contamination were based on model-dependent predictions (e.g. [119, 174, 175]) and suggested that the effects were likely to be small. More recently, however, several groups have worked on cross-correlating CMB data with cluster surveys such as 2MASS (Two Micron All-Sky Survey); APM and ACO surveys, and report evidence that contamination does indeed occur. [143] find evidence for contamination on scales of $\sim 1°$. Evidence for SZ, or SZ-like, contamination in WMAP data has also been reported by, for example, [90] and [22].

On the other hand, [103, 110] find no evidence for SZ fluctuations on degree scales, but some suggestion of SZ-like signal at angular scales of $\sim 10°$. This emission is tentatively associated with relatively cool ($\sim$ 1 kev) electrons in the outskirts of the Milky Way's halo. [73] have also modelled the contribution of the kinetic SZ from the warm-hot intergalactic medium to WMAP data and find that most of the cosmological parameter estimates are unaffected.

Galaxy Cluster Surveys

SZ surveys are, however, expected to be particularly useful for studying the large scale distribution of clusters throughout the history of the Universe. The importance of cluster studies lies in the fact that, in the concordance model of cosmology, they trace the evolution of the density perturbations we observe in the CMB at the

time of recombination. The large-scale structure of the Universe can be modelled using these density perturbations and assuming values for the characteristic parameters of the Universe. Observations of the abundance and evolution of clusters with redshift are, therefore, a sensitive measure of cosmology (see e.g. [8, 62, 74, 169]).

Cluster surveys based upon SZ observations have been considered in detail in this context, and have a number of distinct advantages over other survey methods. These include:

1. A distinct spectral signature, as discussed already, which in principal allows a clean removal from other sources in the sky (although clearly other sources of contamination remain). Furthermore, the spectrum and brightness of the SZ effect is linked to basic physics rather than more complicated processes, and does not suffer from dust obscuration.

2. As demonstrated by (2.27), the change in specific intensity due to the SZ effect is independent of redshift. Currently, there are relatively few clusters known with redshifts greater than ~ 1, yet knowledge of the cluster distribution to high redshift is essential for precise determination of cosmological parameters from cluster surveys. The strongest constraints on dark energy parameters, for example, are expected to come from observations of the cluster evolution about this epoch, when the Universe is thought to have moved from dark matter to dark energy dominated [12].

3. A sample that is defined by a mass limit. It has already been mentioned that the integrated Compton parameter, Y, defined in (2.42), is dependent upon the thermal energy of the cluster. Based on the assumption that the cluster is in hydrostatic equilibrium, this means that Y can be related in a straightforward way

to the total virial mass of the cluster:

$$Y \propto \frac{M_{virial}\langle T_e \rangle}{D_{\rm A}} \tag{2.48}$$

where $\langle T_e \rangle$ represents the mean electron temperature. At higher redshifts, the angular diameter distance $D_{\rm A}$ is expected to become relatively constant. Furthermore, clusters earlier in the Universe's history are expected to be denser and hotter. It is concluded, therefore, that the mass limit observable by SZ studies, and the corresponding selection function for SZ surveys, should end up being almost constant with redshift [36].

Mass-scaling relationships have been deduced for other SZ parameters (e.g. the maximum value of the Compton parameter), but Y is consistently found to be a more robust estimator for the cluster mass in cosmological simulations [141,225]. This general conclusion recently received observational support from Rines, Geller and Diaferio [182] who measure the virial masses of 15 clusters from the Hectospec Cluster Survey (HeCS) and compare them to the SZ signal from these clusters. They find the virial mass and SZ signal to be strongly correlated (at greater than 98% confidence) and characterise the scaling between them as a power law with a slightly shallower index than that expected from numerical simulations. [3]

The significance of the relationship between SZ surveys and mass limits becomes obvious when we consider the cosmological significance of cluster counts [15, 36, 213]. The fundamental principal in such studies is that the distribution of cluster mass at a given redshift, otherwise known as the cluster mass function,

[3] Although see [133], who compare cluster masses estimated from gravitational lensing in 14 clusters to the values predicted from their integrated Compton parameters, and find a significantly weaker correlation.

depends sensitively upon cosmological parameters. Precise models for the mass function vary depending upon the details of the physics involved and the method of determining the mass function. The first analytic attempt at its derivation was by Press and Schechter [166], who obtained:

$$\frac{dn(M,z)}{dM} = -\sqrt{\frac{2}{\pi}}\frac{\bar{\rho}}{M^2}\frac{d\ln\sigma(M,z)}{d\ln M}\frac{\delta_c}{\sigma(M,z)}exp\left(\frac{-\delta_c^2}{2\sigma(M,z)^2}\right) \tag{2.49}$$

where $n(M,z)$ is the comoving number density of clusters with mass $\in (M, M+dM)$; $\bar{\rho}$ is the mean background density of the Universe at the current epoch; δ_c is the critical overdensity required for a region to collapse, and $\sigma^2(M,z)$ is the variation of the density field at redshift z when smoothed by a mass M. The Press-Schechter relation is still frequently used in analytical estimates of cluster number counts although some authors prefer to use the so-called Jenkins mass function [108]. The important feature of both forms of the mass function, however, is that $dn(M,z)/dz$ depends exponentially on cosmological variables making them sensitive to different models for the Universe's evolution. In (2.49), $\bar{\rho}$ and $\sigma(M,z)$ both depend on cosmology. $\sigma(M,z)$ in particular can be separated: $\sigma(M,z) = \sigma(M)D(z)$, where $\sigma(M)$ represents the variance of the original density field at the epoch of recombination, and $D(z)$ is the so-called growth function, which governs how those density fluctuations subsequently evolve with time [36]. These functions can be simulated or calculated analytically for a given cosmology to determine the form of the mass function.

It is then possible to relate the mass function to, for example, the expected number of clusters observed by a survey, N, by:

$$\frac{dN}{dz} = \Delta\Omega \frac{dV}{dz d\Omega}(z) \int_{M_{lim}}^{\infty} \frac{dn}{dM} dM \tag{2.50}$$

[222] (where $\Delta\Omega$ is the solid angle of sky observed during the survey; $dV/dzd\Omega$ is the volume elements at redshift z - itself dependent on cosmology - and M_{lim} is the mass limit of the survey), and compared with observations.

The same principle can be applied to other differential functions [61], which have different systematic uncertainties and may, therefore, be more appropriate for a specific experiment. One such example is the temperature function: $d^2N/dTdz$, related to the mass function by:

$$\frac{d^2N}{dTdz} = \frac{d^2N}{dMdz}\frac{dM}{dT} \tag{2.51}$$

In this context, the scaling relationships discussed previously can also be used for cosmology studies (e.g. [194]).

It is clear, however, that in order to evaluate either dN/dz or $d^2N/dTdz$, information is required about the redshift of the clusters. For this reason, a multifrequency approach may be required to take full advantage of the potential SZ surveys, with optical follow-up to SZ detections [60, 61]. Alternatively, the cluster survey can be characterised by the number density of sources with integrated SZ flux, S, defined by:

$$S = \int_{cluster} \Delta I_{SZ} d\Omega \tag{2.52}$$

where ΔI_{SZ} is the change in specific intensity due to the SZ effect described previously and the integration is performed over the entire solid angle of the cluster [61].

The addition of redshift information would also increase the range of studies that could be performed. As discussed earlier in this chapter, the SZ effect can be used to measure the Hubble constant for individual clusters. A more accurate method for determining H_0 is simply to include information from a larger sample. A plot of values for D_A measured for a large number of clusters against their redshifts can be fit for H_0 for a given cosmological model [36]. A plot of SZ-derived values of H_0 can be plotted against redshift to provide an independent test of the results of the supernova studies which provided the first indications that the Universe's expansion is accelerating (e.g. [159]). It is even possible that generic predictions about inflation may be extracted from SZ surveys. In general, inflation predicts that the distribution of primordial density fluctuations in the CMB should be gaussian. Since SZ surveys should be most sensitive to the highest peaks in the density field (i.e. the highest mass clusters), whose number density should lie in the wings of the Gaussian distribution, an observed excess of these peaks should be a clear indication of non-Gaussianity in the original field. Such observations are particularly significant at high redshift [18,36]. A detection of non-Gaussianity might also, however, be used as a test of *alternative* models of inflation [183].

Another possible function of cluster surveys frequently referred to in the literature is as a measure of the University mass density, Ω_M (accounting for baryonic and dark matter). This is based upon the measurements of cluster gas mass fractions discussed in the previous sections of this review. In general, during the evolution of clusters, no significant segregation between different forms of mass is expected to take place (whereas at smaller scales there is clearly a large segrega-

tion: the Solar system does not appear to contain an appreciable amount of dark matter but is obviously dominated by ordinary baryonic matter). This means that cluster gas mass fraction can be used as an estimate of the proportionality between baryonic and total mass in the Universe in general:

$$f_g \equiv \frac{\Omega_B}{\Omega_M} \tag{2.53}$$

where Ω_B is the baryonic mass density in the Universe. Given independent estimates of Ω_B from, for example, Big Bang nucleosynthesis predictions or CMB experiments, it is clear therefore that measurements of f_g can be used to estimate Ω_M [36].

This method has been used to make initial estimates of Ω_M using relatively small samples of clusters [80, 93, 144]. The estimate is complicated slightly since, without a complete understanding of cluster physics, it is not known precisely the extent to which (2.53) represents an exact equivalence. It seems likely, for example, that some baryons may be lost during cluster formation. [68] estimate that the gas mass fraction defined at a radius, r_{500} (within which the mean density of the cluster is 500 times the critical density) can be related to the 'true' gas mass fraction of the Universe, f_g^{true} by:

$$f_g = 0.9 f_g^{true} \tag{2.54}$$

based upon simulations. [4] As emphasized in [36], however, the presence of

[4]The exact form also has a mild dependence upon cosmology, which would become important for a sample of clusters over a larger range of redshifts, implying that estimates of Ω_M based on this method would have to be deduced statistically rather than analytically.

additional reservoirs of baryons in clusters that have not yet been detected cannot be dismissed.

While there is a high level of optimism over the cosmological results that can be obtained by SZ surveys, some authors have outlined concerns about systematic effects in the measurements. Some of these issues are related to the effects of unusual cluster conditions that, in the context of cluster physics studies, are to be welcomed. Despite the fact that the SZ is less sensitive to the detailed physics in cluster gas than X-ray studies, with higher precision measurements and data from clusters in the early Universe - where the kinds of formation processes expected to be capable of producing detectable SZ signals (see above) are more likely to take place - simple assumptions about the physical state of cluster atmospheres are likely to become increasingly inappropriate [44]. [145] explore the effect of galaxy formation on SZ signal, and find that the normalisation of the SZ effect can be supressed by as much as 30 - 40% due to gas cooling and star formation. Meanwhile [185] study non-equilibrium electrons in the outskirts of simulated galaxy clusters and find that they have the potential to also suppress the SZ signal, leading to a bias in the assumed SZ gas mass amounting to as much as 5%, which would have important consequences for cosmology experiments.

[135] and [1] also discuss contamination of the SZ signal from, for example, point sources and infra-red (IR) galaxies. [1] in particular find that astrophysical contamination is likely to be a greater source of error than statistical errors. They conclude as a result that SZ surveys will not be able to meet their scientific expectations without additional information or follow-up observations. It seems likely, therefore, that the studies of cosmology and cluster physics, as well as that of foregrounds such as point sources and IR galaxies, cannot be separated and treated independently. For a further discussion of selection and systematic effects in SZ

cluster surveys, see [111].

Beyond these principal applications of SZ cluster surveys in studying cosmology, there are a range of other studies that have been discussed in the literature. The effect of the decay of dark matter particles on the SZ power spectrum, for example, is explored in detail by [208]. They find that the power spectrum is decreased at large angular scales, but increased at small scales. They further predict that upcoming SZ surveys could be able to estimate the decay lifetime of decaying dark matter to within a factor of two. Similarly [38] describe how studies of gas mass fractions extended to high redshift could provide information on the decay of dark matter.

The SZ power spectrum has also been discussed in the context of determining the normalisation of the matter power spectrum, σ_8, which is an extremely important parameter in the study of large-scale structure formation. [120] find that the coefficients of the SZ power spectrum (without accounting for the dark matter decay mentioned above), C_l^{SZ} scale according to:

$$C_l^{SZ} \propto \sigma_8^7 (\Omega_B h)^2 \tag{2.55}$$

where h is the Hubble Constant expressed in units of 100 $kms^{-1}Mpc^{-1}$. Based upon measurements of excess power from two independent experiments, and assuming that all this power can be attributed to the SZ, they estimate $\sigma_8 = 1.04 \pm 0.12$. This is, however, higher than other estimates of σ_8. Measurements of the CMB power spectrum by SPT (South Pole Telescope), for example, find $\sigma_8 = 0.773 \pm 0.025$ [128], while ACT (Atacama Cosmology Telescope) and BOOMERanG obtain upper limits for σ_8 of 0.86 and 0.96, respectively [69, 219].

In an earlier paper [11] also discuss how the mean value of the Compton parameter in an SZ survey, $\langle y_0 \rangle$, as well as number counts, can be used to estimate the present-day cosmological density, Ω_0 defined by: $\Omega_0 = 8\pi G\bar{\rho}_0/3H_0^2$ (where $\bar{\rho}_0$ is the present-day average density of the Universe). They compare two cosmological models and find that the values of $\langle y_0 \rangle$ vary by an order of magnitude for the different models.

The kinematic effect has also been extensively studied, in particular in relation to helping constrain the parameters that define dark energy (see, e.g. [222]). The underlying principal is that in linear perturbation theory - which describes the evolution of primordial anisotropies in the CMB - the magnitude of velocity perturbations is given by:

$$\tilde{v}(\tilde{k}) = i\frac{d\mathrm{ln}D}{d\mathrm{ln}a}\frac{aH\delta(\tilde{k})\tilde{k}}{k^2} \tag{2.56}$$

[58] where D and H are the growth factor at late times and Hubble constant, respectively; a is the scale factor, and $\delta(\tilde{k})$ represents density variations with wavenumber, $\tilde{k}$, in the early Universe. The velocity distribution of galaxy clusters, which is measured by the kinetic SZ, can also, therefore, be used as a probe of cosmology.

There have been a number of methods proposed which take advantage of this idea. Examples include [58], who consider cross-correlations with galaxy counts to constrain the dark energy equation of state, w as well as its evolution, dw/da. They also consider how such a study may be able to investigate the distribution and evolution of baryons in the Universe. Alternately, [21] investigate how three different velocity statistics - the distribution of radial velocities; the so-called 'mean

pairwise streaming velocity', and the velocity correlation function - can be related to dark energy properties. [21] also find that the constraints on the dark energy properties are comparable to or even better than those obtained by supernova measurements and other probes of dark energy identified by the Dark Energy Task Force [4].

2.3 SZ observations

The quantity and quality of SZ observations has increased rapidly over recent decades. By the end of the millennium, there were approximately 50 clusters with SZ detections [23], although many of these measurements were severely hampered by systematic uncertainties. In the last decade, it has become possible for equivalent numbers of clusters to be observed by a single project (e.g. [125]). The current status of observations using the SZ is an exciting one, with several 'next-generation' projects starting to produce results, or soon to begin operation.

Traditionally, SZ research has been conducted either using single-dish telescopes or interferometry. Of the two observational methods, single-dish observations were initially the more practical alternative and most of the SZ measurements made before 1990 used this approach (e.g. [7,81,123,186,216,217]. Interferometers are well-known for their high resolution, but this can become a problem for SZ observations. Nevertheless, interferometers have a number of important advantages for imaging the SZ, which led to a series of experiments being proposed designed specifically for that purpose. Both techniques suffer from important systematic effects, however, which are discussed further below.

Single-dish observations

There are a large number of single-dish telescopes that have been used for SZ detection. These include, for example: the One Centimetre Radiometer Array (OCRA) [5] ; Bolocam [6] ; the Aztronomical Thermal Emission Camera (AzTEC) [7] ; the Sunyaev-Zel'dovich Infrared Experiment (SuZIE) [8] , and APEX-SZ [9] .

The dominant source of emission at millimetre wavelengths comes from the Earth's atmosphere. Even in optimum weather conditions, sky emission can be three orders of magnitude greater than the SZ signal [23]. It is clear, therefore, that the removal of this noise is one of the most important objectives of these measurements. It is also clear that the removal has to be very efficient in order to reduce the contribution from the sky to a level which is significantly less than the target source for the observation.

The way in which single-dish observations achieve this is by using a variety of differencing techniques. These techniques share a common principal: by comparing emission from a 'reference position' (a region of sky that does not contain the source of the observations, and is assumed not to contain any other equivalent astronomical signal) to emission from the 'target position' (where the target of the observations is situated), and subtracting the signal from the two fields, the sky emission is reduced.

This assumes that the emission at the reference position is an accurate representation of the atmospheric emission at the target position, which clearly may not

[5]Mounted on the Torun 32m dish - http://www.jb.man.ac.uk/research/ocra/
[6]http://www.cso.caltech.edu/bolocam
[7]http://www.astro.umass.edu/AzTEC/
[8]http://www.stanford.edu/≈schurch/suzie_science.html
[9]http://bolo.berkeley.edu/apexsz/instrument.html

be true. There are, therefore, a number of differencing methods that can be used to increase the efficiency of the sky removal. The most basic differencing is carried out by position-switching, where the telescope beam is physically switched between the reference and target positions by moving the telescope dish; or drift-scanning, where the sky is allowed to pass through the beam of the telescope normally, but the time-sequence of sky brightnesses is then converted into a scan in position and fitted with a model that combines atmospheric noise with the SZ emission [23].

More sophisticated methods include using multiple feed-horns, so that the dish can observe two regions of the sky simultaneously; beam switching, where the beam is shifted between reference and target by chopping the telescope's secondary mirror, [10] and digital differencing in bolometer arrays, which produce continuous measurements of the underlying astronomical brightness in the field as the signal scans across the individual detectors in the array (as used, for example, in the Sunyaev Zel'dovich Infrared Experiment [SuZIE] [95]).

Differencing techniques can, however, introduce new uncertainties in the signal received due to differences in the system noise for the telescope when it is observing the reference and target positions. These uncertainties relate to, for example, variations in ground pickup in each beam or, in the case of twin-horn systems, losses through each channel [23]. Time-variation in these signals introduce additional complications. These kinds of issues can, however, be reduced significantly by an appropriate choice of scan strategy, particularly if the differencing takes place rapidly.

Furthermore, differencing limits the range of redshift over which observations of sources can take place. In the case of clusters which are at lower redshift, the

[10]Even more efficient sky removal can be achieved by combining beam-switching with position-switching. This was the technique employed to obtain the data analyzed in this thesis.

angular diameter of the cluster may become comparable to the angle between the reference and target positions, in which case the differencing may remove signal from the cluster itself, in the same way as it is supposed to remove sky noise. Increasing the angle between the reference and target positions, however, may not be viable for mechanical reasons, and may undermine some of the basic assumptions about the signal in the two beams that are necessary in order for differencing to be work.

High redshift clusters, however, will have a smaller angular diameter. If this falls below the full-width half maximum (FWHM) of the telescope beam, the intrinsic signal from the cluster will itself become diluted. The play-off between these effects is demonstrated in Fig. 2.6, which shows the minimum mass cluster detectable at a given redshift for two different kinds of survey. Furthermore, while the effect can be modelled, the modelling necessarily depends on assumptions over the underlying cosmology, which may subsequently effect the reliability of the science that can be extracted.

Other major issues for single-dish observations include obtaining an accurate calibration - to convert the electronic signal from the detectors on the telescope into measurements of brightness temperature or flux - and contamination from other astrophysical sources, such as radio sources in the cluster itself or in the rest of the field.

The calibration of data is reliant on observations of calibration sources. In most cases, these sources are planets, whose flux is determined by scaling relationships using previous measurements at other frequencies or using models.

The accuracy of the calibration clearly depends on the reliability of previous

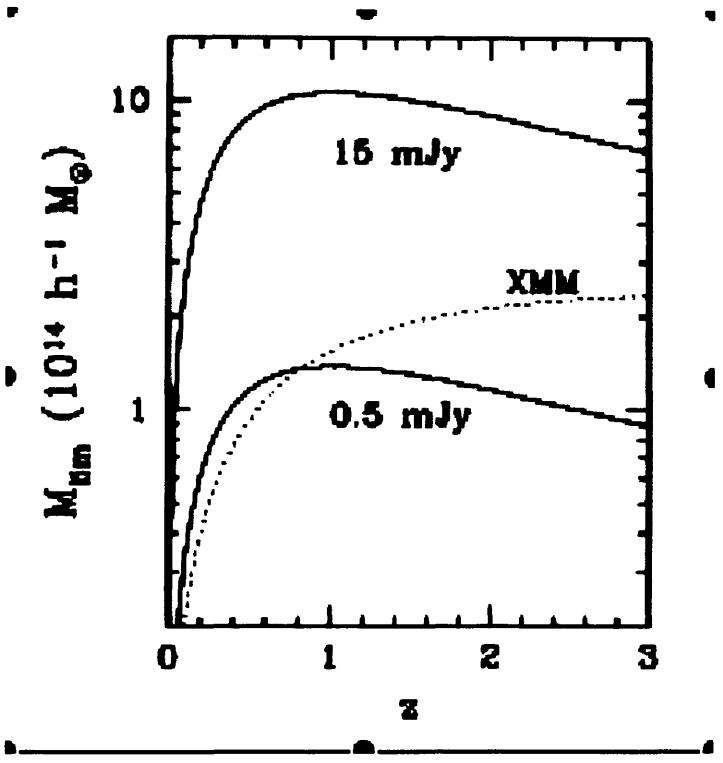

Figure 2.6: Mass limits for SZ detections calculated for a wide-field survey at 30 GHz (15 mJy), and a deep-field survey (5 mJy). The limits for the XMM serendipitous survey are also shown as the short dotted line. Both the 30 GHz limits are capable of detecting similar mass clusters even at high redshift, although there is some tailing off. (Reproduced from [36])

observations and the accuracy of scaling assumptions and models. In some cases the change in flux across the planetary disc also becomes important. Finally, uncertainties in the variation of the telescope beam when observing different sections of the sky can also contribute to error in the calibration. The combination of these effects means that the errors due to calibration can often be substantial, of order 5 - 10% [23].

Contamination from point sources in the same field as SZ targets is also an important source of error, particularly for observations of the SZ at frequencies higher than the null, where the emission of point sources are expected to rise rapidly. Below the null, emission from radio sources also increases substantially. These sources need to be removed from the data if a clean measurement of the SZ signal is to be made. A precise knowledge of the detailed spectrum of millimetre/ sub-mm point sources is, however, lacking. It is known that they can be variable, typically on timescales of months, but this clearly only increases the difficulty of removal, since limited archival data is insufficient to characterise a source [23]. Instead, simultaneous observations of sources is the only means of removing them with more confidence. Except in the case of observations carried out with interferometers (see below), however, this generally means a more complicated analysis (such as the modelling used in this work).

Interferometry

The technique of interferometry works by correlating the signal between two telescopes or receivers. The resolution of an interferometer is equivalent to the resolution of a single dish whose diameter is equivalent to the separation of the two telescopes. The interferometer will, however, only be sensitive to angular scales

close to this resolution. An interferometric array can be thought of as a collection of telescope pairs and, as a result, only samples a finite number of angular scales. Since the telescopes in the interferometer can be separated by large distances, however, the resolution can be made very small [36].

Interferometry has only been used comparatively recently for SZ studies. The first successful measurements of a cluster were made by [25] of Abell 2218. Interferometry is well-known as a technique for obtaining high-resolution astrophysical images and, in the mid-1990s, most interferometers were designed to exploit this feature, but in the case of SZ observations, high resolution can be a problem. This is because the signal associated with SZ measurements generally has a relatively large angular size and so would be 'resolved out' by interferometers [23].

More recently, however, there have been a large number of interferometery projects designed specially with SZ research in mind. These include the Owens Valley Millimeter (OVRO) and Berkeley-Illinois-Maryland Association (BIMA) arrays [11] ; the Square Kilometer Array (SKA) [12] ; the Arcminute Microkelvin Imager (AMI) [13] ; the Array for Microwave Background Anisotropy (AMiBA) [14] , and the Sunyaev Zel'dovitch Array (SZA) [15] .

There are a number of features of interferometric observations that make them useful for SZ observations. The sensitivity to specific angular scales, for example, means that most large-scale background noise (from the atmosphere, for example) is removed. Contamination can also be efficiently removed by imaging the cluster at different angular scales (using different baselines of the interferometer) [23, 36].

[11] Which now operate in conjunction as the OVRO-BIMA SZE Imaging Experiment, see http://astro.uchicago.edu/sze/

[12] http://www.skatelescope.org/pages/page_sciencegen.htm

[13] http://www.mrao.cam.ac.uk/telescopes/ami/

[14] http://amiba.asiaa.sinica.edu.tw/

[15] http://astro.uchicago.edu/sza/index.html

The higher resolution baselines are capable of monitoring point sources in the field while over-resolving SZ emission; whereas lower resolution baselines will image the contaminated SZ. Comparing the two baselines should, therefore, be an effective means of removing radio source contamination.

There are, of course, also problems introduced by interferometry techniques. One of the most important limitations is that the finite range of angular scales probed by an interferometer means that the observations risk simply detecting the component of the SZ emission with the minimum angular scale, although this effect can be ameliorated by appropriate instrument design. Strong sources close to the edge of the telescope beam or in the instrument's sidelobes can also affect the accuracy of the removal of radio sources [23].

Next-generation projects

While interferometry is a useful technique for obtaining high resolution images of SZ sources and controlling contamination, most of the upcoming or current SZ projects are based on single-dish designs. With improvements in technology producing detectors with increased sensitivity, large-scale surveying has become a realistic goal. Among the largest of the current SZ projects are the Atacama Cosmology Telescope (ACT); the South Polar Telescope (SPT), and the Planck satellite.

ACT is a 6 m off-axis Gregorian telescope, situated in the Atacama desert in Northern Chile. It uses three arrays of transition-edge sensor (TES) bolometers capable of observing at 148, 218 and 277 GHz (for full descriptions see [70,92,206]). First results from ACT were reported in [92], in which eight clusters previously de-

tected with X-ray or SZ observations were mapped, and their integrated Compton parameters measured.

SPT is situated at the NSF South Pole research station in Antarctica. The telescope uses a 10 m off-axis Gregorian design, with six TES arrays capable of observing at 95, 150 and 225 GHz [35, 152, 187]. The first detections by SPT were reported by [201] of five clusters, three of which had not previously been detected by other methods, and represented the first clusters detected by a blind SZ survey. X-ray follow-up of two of these clusters is reported in [218]. Since the first detections with SPT, further studies have reported data from increasing numbers of clusters, including the first detections of SZ profiles for individual clusters [91, 163].

Planck is an ESA-funded satellite mission launched in May 2009. The principle aim of the mission is to make the first all-sky survey of the CMB from the second Lagrangian point (approximately 1.5 million km from Earth) with a resolution better than 10', which will be a rich source of information about the early Universe

.

As has previously been noted, however, the SZ is a contaminant of the CMB, so it is essential that, for precise measurements to be made, SZ signal has to be removed accurately from the data. Planck uses two instruments to provide coverage over nine frequency channels between 30 and 857 GHz, so should be capable of identifying and removing SZ extremely efficiently.

The SZ data collected in this way clearly has huge scientific potential. Early simulations of the scale of potential cluster surveys using Planck predict that it should be capable of detecting of order 10^3 - 10^4 clusters [72, 87], eclipsing the surveys that have been carried out to date. The potential for independent cosmo-

logical studies based upon this data is correspondingly large, although the potential for studying individual cluster physics using Planck is low.

For detailed descriptions of the Planck instrument and mission, as well as reviews of the project's potential for cosmological research, see [9, 32, 71, 212, 224, 227]. Detailed discussions of the methods of extracting SZ signal from Planck data, as well as the prospective scientific applications of this data can be found in [132, 190, 191].

In this chapter, we have reviewed the theoretical background to the SZ effect; discussed the scientific potential of future SZ projects, and assessed the methods and status of SZ observations, including a brief outline of large current and next-generation projects. In the next chapter, we will discuss the details of the observations that provided the data used in this thesis and outline the general principals used in the data analysis to obtain scientific maps from it.

Chapter 3

Jiggle Map Observations

The raw data used for making the cluster maps was obtained using Bolocam, a large-format bolometer camera mounted on the Caltech Submillimeter Observatory (CSO) on Mauna Kea in Hawaii. The CSO consists of a 10.4 meter diameter radio dish, also known as The Leighton Telescope, with the capability to mount instruments either at the Classical Cassegrain or Naysmith focus. The integrity of the dish's surface is maintained using actuators mounted on the back of the dish, which correct for distortions of its shape due to, for example, temperature differentials across its surface.

Bolocam consists of 144 Si_3N_4 spider-web bolometers with neutron-transmutation-doped germanium (NTD-Ge) thermistors, cooled by a three-stage, close-cycle Helium fridge to 250 mK [76]. Bolocam is mounted at the Cassegrain focus of the CSO and can be operated at either 1.1 mm (273 GHz) or 2.1 mm (143 GHz). The data for the maps in this project were taken with Bolocam operating at 1.1 mm. Each pixel has an approximately circular field of view of 8 arcmin and the

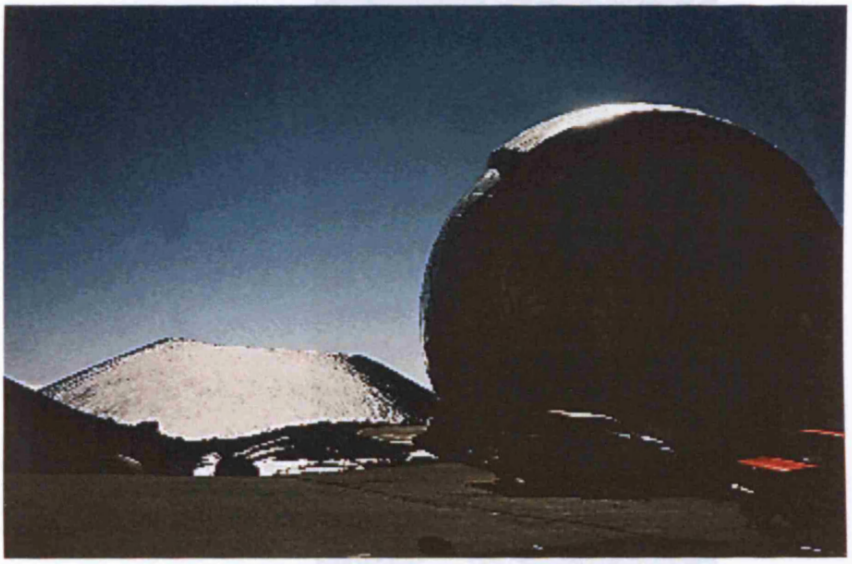

Figure 3.1: The CSO taken near the summit of Mauna Kea.

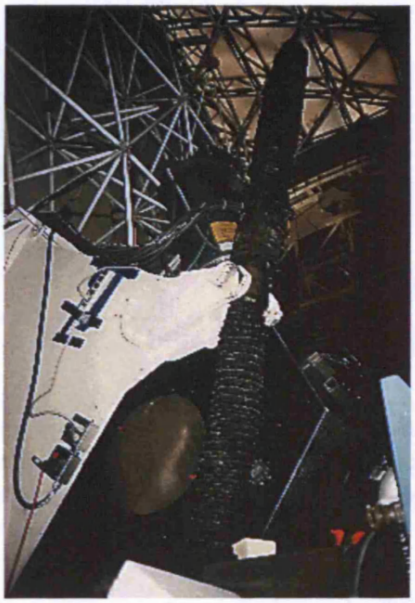

Figure 3.2: Bolocam mounted at the cassegrain focus of the CSO.

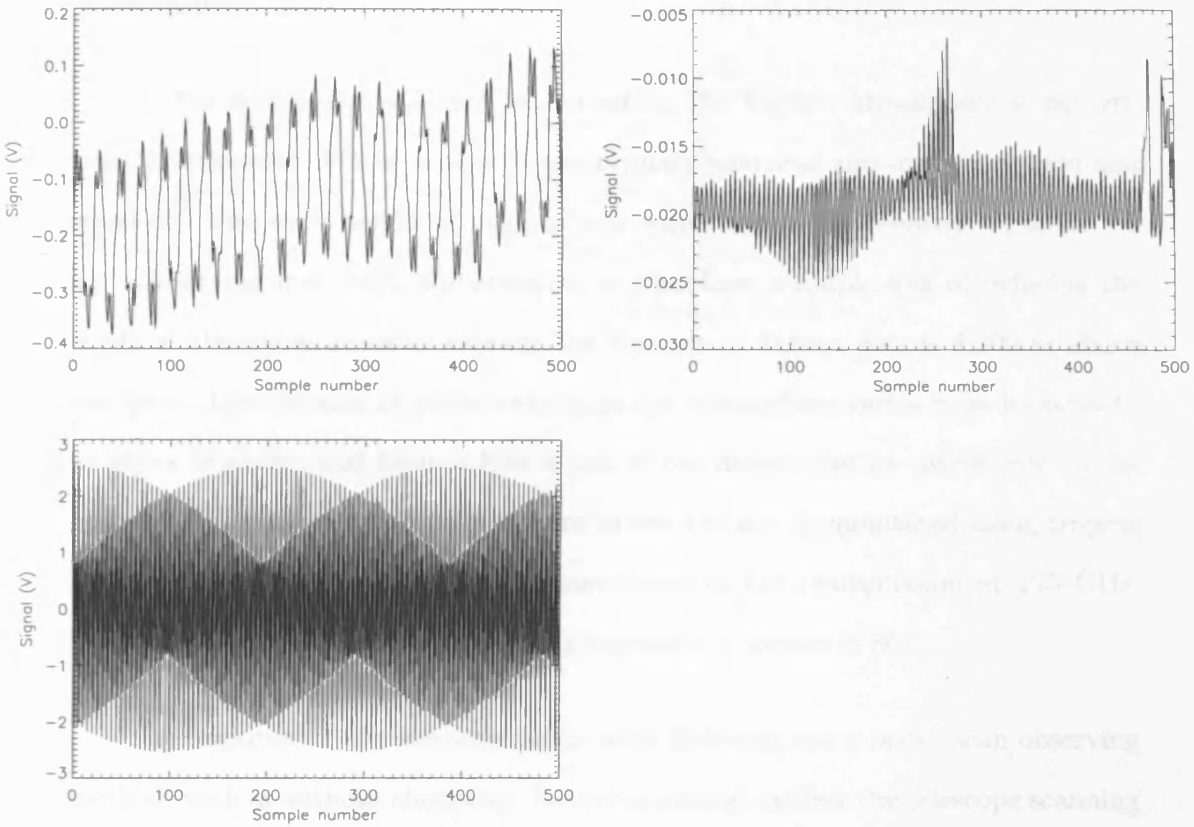

Figure 3.3: Examples of data from good and bad bolometers. The signal from good bolometers show a clear noisy-sinusoidal variation, whereas the signal from bad bolometers is either extremely low and without a consistent pattern, or displays a signal that appears to be have a harmonic structure.

instrument has a full-width half-maximum of approximately 30" at 1.1 mm [1] .

Over time, the performance of individual detectors in Bolocam are expected to degrade naturally, and not all of the 144 bolometers could be used in the processing. So-called 'bad' bolometers were identified by eye from the data itself. Fig. 3.3 demonstrates examples of signal from both good and bad bolometers. Data from the good bolometers showed a clear chopping pattern, whereas bad bolometers showed no consistent evidence of chopping. Based upon individual examination of the data from each of the bolometers, 105 were identified as operational and used

[1]For more information, see http://www.cso.caltech.edu/bolocam/ProposerInfo.html

in the analysis.

At millimetre and sub-mm wavelengths, the Earth's atmosphere is not entirely transparent. Water vapour is the primary source of sub-mm absorption and emission. The scale height of atmospheric water vapour is, however, of order 1-2 km. Observing from high altitude sites is, therefore, a simple way of reducing the levels of atmospheric water vapour; the summit of Mauna Kea is 4,200 m above sea level. The amount of water vapour in the atmosphere varies from location to location, however, and Mauna Kea is one of the driest sites for astronomy on the planet. The opacity of the atmosphere above the site is monitored using tipping radiometers to provide periodic measurements of the transmission at 225 GHz. Transmission at 273 GHz at the site is typically in excess of 80%.

The majority of observations taken with Bolocam use a raster scan observing method, with or without chopping. Raster scanning involves the telescope scanning across the region that the observer wants to image and is a method of obtaining a time-varying signal in order to try to remove sky background and 1/f noise. The data used in this report, however, was obtained by using a more complicated scan strategy. First, the secondary mirror was 'chopped' continuously from side-to-side during the observations, so the field of view moved back and forth across a region of sky defined by the 'chop throw' (the maximum angle of deflection of the secondary mirror). The beams located at the extremal positions of this throw are referred to as the 'on' and 'off' beams. Next, the entire telescope was moved so that whichever region of sky was being imaged at a given period of observation switched between beams. i.e. if the region of sky containing the target for the observations began in the on beam, the telescope was moved to a position where it occupied the off beam. This movement of the telescope is referred to as 'nodding'.

Nodding, as opposed to chopping, happens in steps, so that the region of sky under investigation alternately remains in the on and off beams for extended periods of time. The observation of one area of sky requires it to be imaged in the on beam for a period of time, t'; then in the off beam for a period of approximately $2t'$, and finally in the on beam again for a period of approximately t'. We refer here to one complete set of on-off-off-on observations as a 'subsection'.

The scan strategy was designed to be a more efficient means of removing telescope noise and sky background. The basic concept, as outlined in Chapter 2: 'The Sunyaev Zel'dovich Effect - theory and observation', is to subtract signal from target and reference fields. If the signal in the reference field contains only sky noise, $B^{ref}_{sky}(t)$, whereas the signal in the target field contains both sky noise and astrophysical signal, $B^{tar}(t) = B^{tar}_{sky}(t) + B^{tar}_{sig}$, then subtracting the fields should leave only astrophysical signal, provided that $B^{ref}_{sky}(t) = B^{tar}_{sky}(t)$. If the target and reference fields are chosen to be close to one another, the accuracy of this assumption is likely to improve.

As noted previously, however, the flux from astrophysical signals can be only of order 0.1% or less of the sky noise. If there are, therefore, gradients in the noise, such that the noise in the target and reference beams are not equal:

$$B^{tar}_{sky}(t) = B^{ref}_{sky}(t) + \delta B_{sky}(t) \tag{3.1}$$

even though $\delta B_{sky}(t)$ may be small in comparison with $B^{ref}_{sky}(t)$ and $B^{tar}_{sky}(t)$, it could still be equivalent to or larger than the astrophysical signal. More complicated schemes are, therefore, required in order to remove the sky noise efficiently. Including a nod is one such method.

In the ideal case, the beam would be able to shift between the target and reference instantaneously, resulting in a top-hat data timestream. Clearly, however, this is not a mechanically feasible proposition. In practice, therefore, the signal is modulated by a sine-like function:

$$B(t) = B_s \sin[\nu_c t + \phi_c] + B^{sky}(t) \tag{3.2}$$

where B_s is now the signal from the target source; ν_c and ϕ_c are the chop frequency and phase respectively, and $B(t)$ is the signal detected by the instrument at time, t.

If values for ν_c and ϕ_c can be estimated, therefore, the time-variation in the signal can in principle be extracted. This can be achieved by monitoring the chopper position and fitting to the variations to obtain an estimate of ν_c. ϕ_c can be estimated using this fit and comparing the chopper position to the fluctuation in the data timestream. The estimated values of ν_c and ϕ_c will be referred to as ν_f and ϕ_f, respectively.

The signal from the astrophysical source can then be extracted analytically. If we ignore the term representing the sky noise in 3.2 (since it will be subtracted out by the nod), we can multiply the signal by the fit time-variation in the signal and integrate according to:

$$B_{est} = \frac{\int B(t) \sin[\nu_f t + \phi_f] dt}{\int \sin^2[\nu_f t + \phi_f] dt} \tag{3.3}$$

It is clear from (3.2) that, for an accurate fit ($\nu_f \rightarrow \nu_c$, $\phi_f \rightarrow \phi_c$), $B_{est} \rightarrow B_s$.

Naturally, there are a number of general constraints and limitations to this mode of observation. First, the data acquisition time has to be significantly smaller than the chop period in order to resolve the variation in signal. Second, the chop period clearly has to be smaller than the period of the nodding in order that there are a reasonable number of chop periods at each nod position. The chopping also has to be rapid enough that the sky noise will not alter significantly in the reference and target beams during individual chop periods.

Furthermore, if a source is extended, the chop throw must be large enough to ensure that whichever beam does not contain the area of interest at a particular point of the observations contains *only* background emission. If this is not the case, emission from the extended structure may lead to inaccuracy in the flux calculated for the target region. Although in principal one could model the effect, it would increase the errors in the flux measurements. Conversely, however, the chop throw must be small enough that the assumption of a constant sky background between the on and off beams remains reasonable.

In order to form a fully-sampled image of the region around the source being observed, the telescope was also 'jiggled', so that the position of the beam centre for a given on-off-off-on sequence varied around the source. In this way, an image of the cluster $\sim$ 10 arcmin$\times$10 arcmin was formed.

The observations used for this work were taken during an observing run at the CSO starting in late January and ending at the beginning of February 2006. The principal investigator for this run was Eiichi Egami. Data was sampled every 0.02 s. The chop frequency was 2.25 Hz, making a single chop $\sim$ 0.44 s in length, while the chop throw was 90". The telescope was nodded in azimuth, and the period of time during which the telescope was oriented so that the source was

located in either the on or off beam was $\sim$ 9 s. The total time taken to complete a single subsection (accounting for a certain period where the telescope was slewing between positions on the sky and therefore not acquiring data) was, therefore $\sim$ 45 s.

The data taken during the observations was stored in network Common Data Form (also known as 'netCDF', or 'ncdf') files. Network Common Data Form is a set of libraries and data formats designed specifically for handling array-oriented data [2] . Each ncdf file contained 60 variables, providing information on, for example, the weather conditions at the time of observing; details of the chopping and acquisition, as well as the raw data itself.

The observing run targeted four clusters: Abell 1835; Abell 851; Abell 2218, and MS0451.6-0305, all of which are well-known and well-studied objects at other wavelengths. The fields surrounding all these clusters were known to contain a number of point sources. As discussed previously, uncertainty in the characterisation of point sources in SZ fields, and hence the amount of contamination from these sources, is one of the most important limitations in SZ studies at higher frequencies. The original motivation for the observations were, therefore, to characterise these point source fluxes accurately.

The observations of the main science targets were broken down into individual files of $\sim$ 50 minutes (3000 s) duration, composed of 63 individual subsections. These observations were separated by shorter observations of pointing/ calibration sources lasting $\sim$ 10 minutes (600 s). The full Jan 2006 observing run is given in Appendix B.

In this chapter, the telescope and detector used to obtain the data analyzed

[2] see e.g. http://www.unidata.ucar.edu/software/netcdf/

in this thesis have been described. The scan strategy used has also been outlined. At the beginning of the project the standard Bolocam pipeline was not suitable for mapping data obtained using the combined chop and nod scan strategy. It was necessary, therefore, to write a new pipeline. In order to have complete control over the process, it was also decided that this pipeline would be written largely independent of the existing Bolocam pipeline. The following chapters describe the pipeline code and its development.

Chapter 4

Pipeline Development I: Demodulation and mapping

The mapping pipeline for the Bolocam data was written in idl and structured as a set of modules handling different functions in the process. The basic aim of the pipeline was to extract signal according to (3.3). In order to achieve this, it was necessary to obtain a reliable model for the chopper signal in order to construct the fit; to understand when the telescope was nodding, then to apply an accurate calibration to transform the signal into units of flux. After this had been done, maps of individual observations could be made. These maps, however, generally had a low signal-to-noise (S/N). Higher S/N images of science sources could be produced by combining the calibrated data and corrected pointing information into a single set of vectors which could then be mapped.

The raw data from observations was stored in a set of 144 voltage timestreams (corresponding to the signal at each time step from each of the instrument bolometers) in each ncdf file. The files also contained a large number of other timestreams

containing positional and other data relevant to the observations. Among the most important of the timestreams used in the mapping were:

ac_bolos: Contained the raw data from the bolometers, filtered then amplified to remove dc offsets that dominate the raw bolometer output;

dc_bolos: Contained the unfiltered, unamplified signal from the bolometers, which was dominated by bit noise but retained the dc offsets (which are essential for calibration - see Chapter 5: 'Pipeline Development II: Pointing and Calibration');

chop_enc: Contained information on the chop based on the signal being used to control the position of the telescope's secondary mirror;

acq_das, acq_tel: Contain information on when the telescope was acquiring data during an observation;

rotangle: Contained information on the rotation angle of the detector plate inside the Bolocam cryostat. This was required to determine the orientation of the map;

source_ra, source_dec, source_epoch: Contained positional information for the source based upon catalogued values, as well as the epoch in which these positions were defined;

az, el: Contained information on the azimuth (az) and elevation (el) of the area of sky the telescope was imaging;

eaz, eel: Contained errors on the values stored in the variables az and el;

ut: Contained the values for Universal Time when the observations were made,

necessary for calculating the precise Julian date at which the observations took place, as well as right ascension (R.A.) and declination (decl.) values based upon the az and el data;

pa: Contained information on the parallactic angle of the observations;

on_beam_tel: Contained information on the times at which the telescope was imaging the source in its on beam (on_beam_tel = 1) and in its off beam (on_beam_tel = 0).

The implementation of different stages of the signal demodulation is described below.

4.1 Nodding Pattern

The jiggle map observing strategy, as described in Chapter 3: 'Jiggle Map Observations', consisted of a sequence of jiggle positions around the target in order to form a fully sampled nyquist image of the region. Each measurement at a jiggle position consisted of a single set of on-off-off-on nodding pattern (as described previously), which formed a symmetric double difference effective beam pattern on the sky. In order to locate the periods when the telescope was observing the target in the on and off beams, the on_beam_tel and acq_tel timestreams were combined according to:

$$n(t) = 2a(t)\,(b(t) - 0.5) \tag{4.1}$$

where $n(t)$ represents the nodding timestream, and $a(t)$ and $b(t)$ represent the

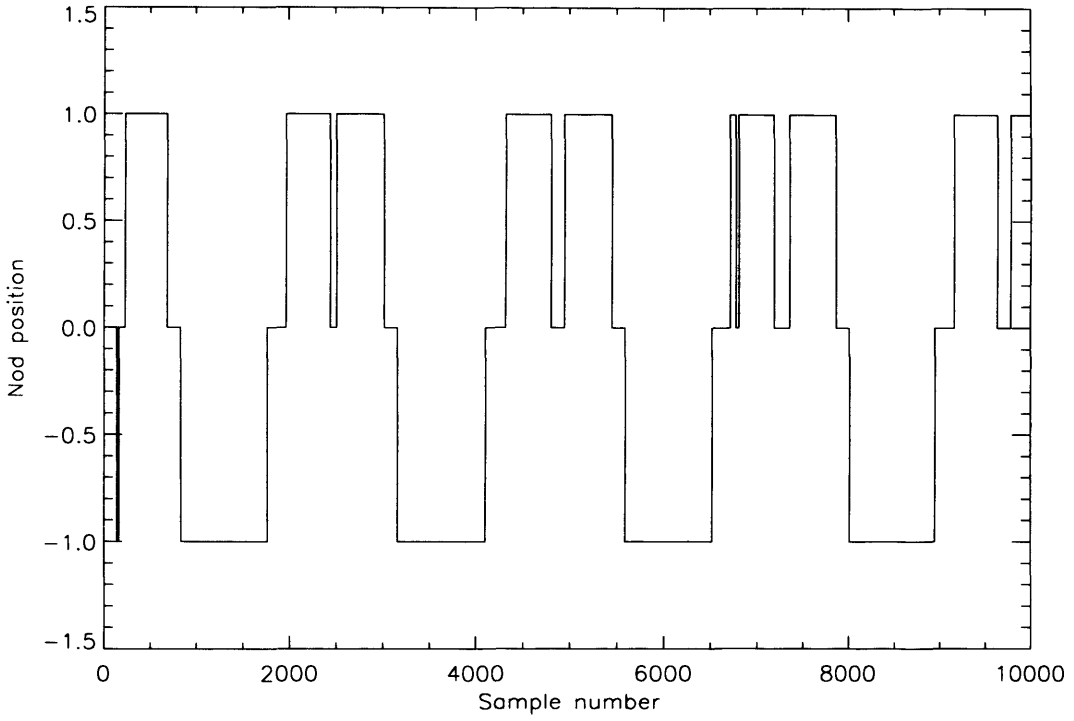

Figure 4.1: Nodding and acquisition pattern. A nod position of +1 implies the telescope is on-source, whereas nod position -1 is when the telescope is off-source. The pattern is a combination of acquisition and positional data, so that where the pattern falls to zero this reflects where the telescope is not acquiring data (usually while the dish is moving to a different location on the sky).

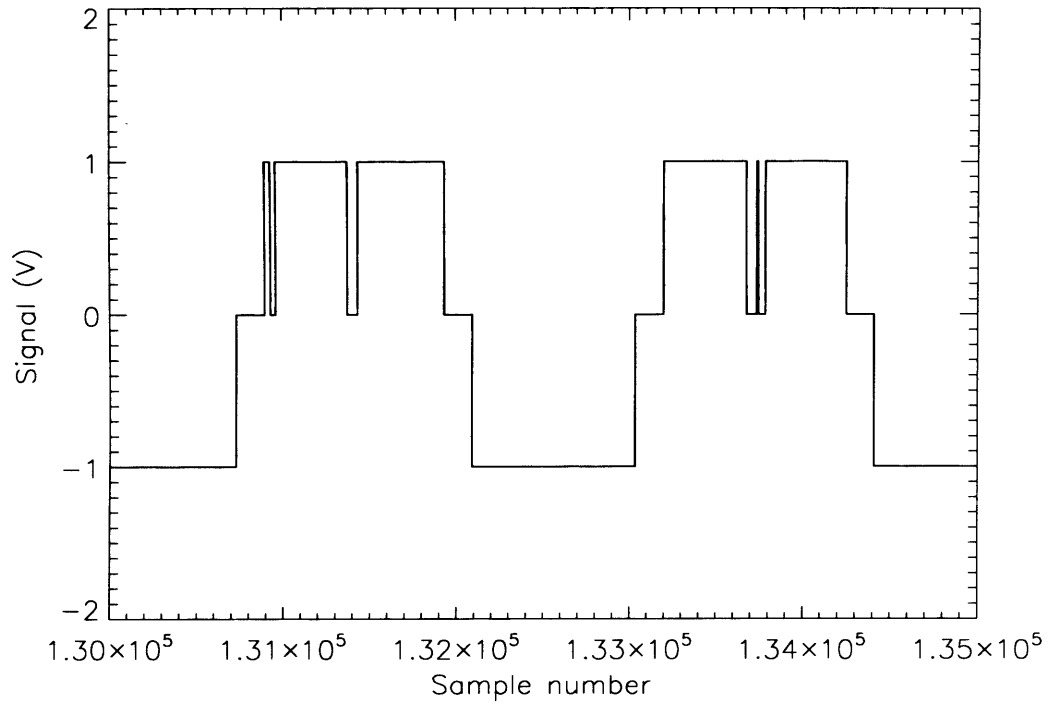

Figure 4.2: Detailed section of nodding pattern, demonstrating spikes in the typical pattern. The spikes were capable of confusing the characterization of the nodding sequence, in particular when they were located between the last 'on' section of once complete nod and the first 'on' section of the next (as in the second nod in this figure).

acq_tel and on_beam_tel timestreams, respectively. This combination produced a data vector which had a value of +1 when the telescope was observing in the on beam; -1 when the telescope was observing in the off beam, and 0 when the telescope was not acquiring data (for example, when moving between on and off positions). An example of this pattern is given in Fig. 4.1.

The beginning and end of the on and off sections could then be identified simply by examining the first derivatives of the timestream:

$$d(t) = n(t+1) - n(t) \tag{4.2}$$

where the beginning of the on sections were identified by $d(t) = 1$ and ended at the next occurrence of $d(t) = -1$ (and vice-versa for the off sections). The acquisition timestream did not, however, have an entirely regular pattern, and exhibited short sections where the telescope was acquiring data (or not) in regions which were clearly not part of the overall nodding scheme. This led to short, intermittent breaks or spikes in the nodding timestream which confused the analysis of the first derivative (see Fig. 4.2).

These irregular features were dealt with by smoothing the nodding timestream to remove short-period features in the nodding. The characteristic period below which features were smoothed had to be chosen carefully, since in some cases breaks in acquisition were of similar length to real features in the nodding. This characteristic period was determined by forming a histogram of the distances between subsequent features in the first-derivatives of the on timestream (formed simply by extracting those regions of the nod where the values are 1) and calculating the modal value. While there remained the possibility that, given a sufficient number of irregular regions, the modal value may have reflected the size of the irregularities rather than the size of the subsections, this could be avoided by an appropriate choice of binsize when forming the histogram and by checking whether or not the distribution of the differences was bimodal; or by studying how the modal value changed with binsize.

A further complication was that the nodding timestream occasionally began while the telescope was acquiring, which confused the series of first derivative values. Individual on or off subsections at the start or end of the observations could also be unusually large or small. All these scenarios had to be accounted for in the module.

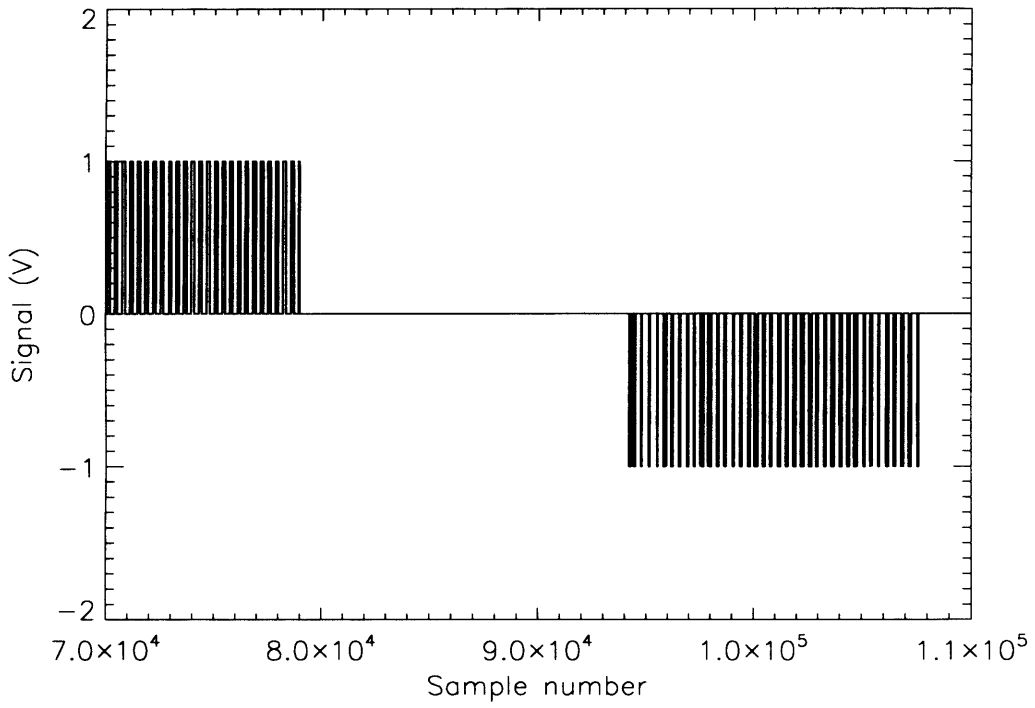

Figure 4.3: Nodding structure for the Mars file 060205_ob7. The nodding sequence is clearly different to the typical structure.

Bad data files could also be identified in this process, since their nodding structure did not show the regular nodding structure (Fig. 4.3).

The acq_tel and on_beam_tel timestreams were both recorded according to the telescope clock whereas the observational and chopping data were recorded by a separate computer. Differences between the timing of timestreams recorded by each computer could arise from filtering of the acbolos and from intrinsic timing differences between the elesctronic components and had to be corrected for. This could be achieved simply by comparing the acq_tel and acq_das timestreams. The first derivative of each were calculated according to (4.2). The derivatives of the acq_tel timestream was used as a template for acq_das and used as a filter to determine the value of time difference which led to optimal matching between the two differential timestreams. This was achieved by repeatedly shifting the acq_das differential timestream then multiplying with the acq_tel differential vector, and summing the resulting datastream. The sum was largest where the match between acq_das and acq_tel was greatest, and the shift required to achieve this was subsequently recorded.

4.2 Chopping Timestream

Next, it was necessary to accurately model the chop signal in each subsection of the data. The simplest method of achieving this would be to calculate the frequency and phase of the chop from the variations in the data timestream and use this to reconstruct the chopping from a specific time and throughout the subsequent subsection. It was not known, however, if there were phase differences between the chop and the data timestreams (due, for example, to clock differences), or if

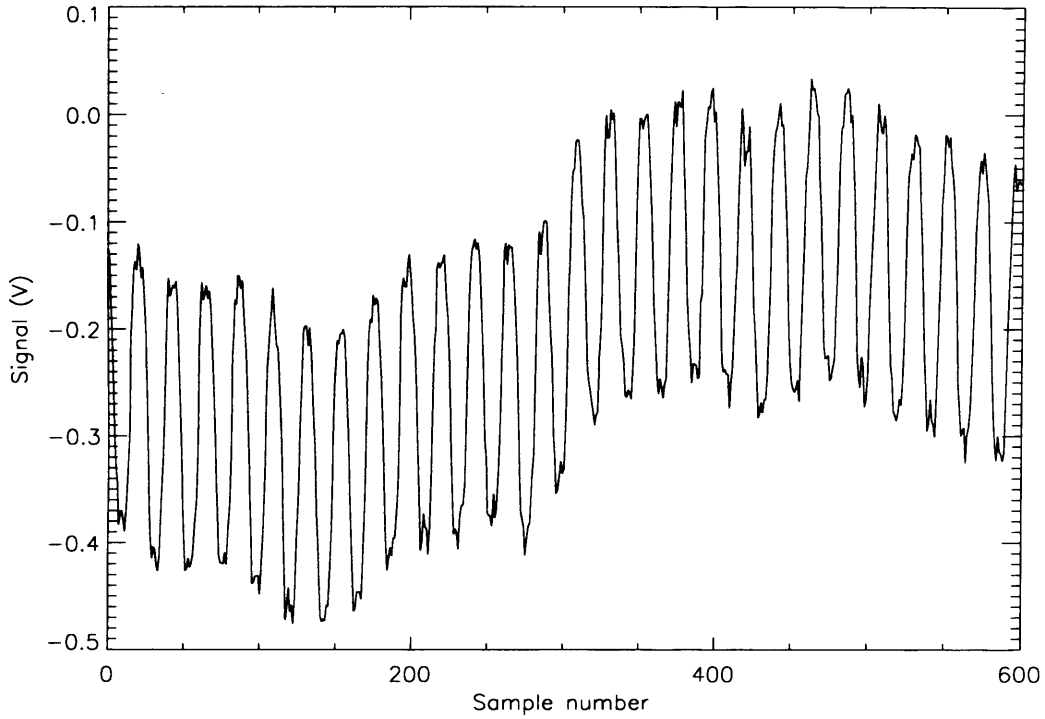

Figure 4.4: A sample of the chop data. The variation in the signal due to the chopping is evident.

sources located along the line of the chop could skew the fit. The fitting had, therefore, to be taken from the chop signal - stored in chop_enc - itself.

An example of a chop timestream is given in Fig. 4.4. Although it was possible to fit the entire chop timestream to obtain single values for the chop frequency and chop phase and reconstruct the chop signal in each subsection, the coding was simpler in the later stages of analysis to isolate the regions of the chopping timestream that corresponded to the nodding subsections and calculate individual chop frequencies and phase differences for each subsection.

This was achieved simply by using the nod boundaries calculated in the previous module to extract the chop regions in each subsection, then fitting these regions with a simple sine function, defined by:

$$F(x) = A(0) + A(1)\sin\left(A(2)x + A(3)\right) \tag{4.3}$$

where A(0), A(1), etc are the fitting parameters. The curvefit routine used in the code required initial estimates for these parameters. It appears from Fig. 4.4 that the offset term is negligible and A(0) was, therefore, set to be small but non-zero. The initial value for the amplitude term A(1) was estimated by calculating the rms value of the chop timestream:

$$A(1) \approx \sqrt{chop(x)^2/n_{samples}} \tag{4.4}$$

where $n_{samples}$ is the total number of samples in the chop timestream, $chop(x)$. This is clearly not going to be an accurate estimate of the amplitude, but should be correct within an order of magnitude, which was sufficient for the fit. The initial value for the frequency term, A(2), was estimated by:

$$A(2) \approx 2\pi f \Delta s \tag{4.5}$$

where f is the angular frequency of the chop (stored in the ncdf files) and Δs is the sample interval of the observations. Clearly, this value was not expected to change much as a result of the fit. The initial value for the phase offset term, A(3), was calculated simply using:

$$A(3) \approx \sin^{-1}\left(chop(0)/chop_{max}\right) \tag{4.6}$$

where $chop(0)$ is the value of the first element of the chop timestream in the subsection being considered, and $chop_{max}$ is the maximum value of the timestream.

Once the fit was finished, the values of frequency and phase were stored in separate variables and passed back into the upper level of the the program.

4.3 Cleaning and baseline removal

Before demodulating the chopper signal, it was necessary to perform a basic spike removal and subtract correlated low frequency atmospheric noise from the signal. Removing the low frequency atmospheric noise could be achieved in a number of ways. The initial approach chosen was to examine the Fourier transform of a given data timestream, identify the signal that corresponded with the chopping, filter out the low frequency baseline, and reconstruct the signal according to the adjusted Fourier transform.

In order to do this, it was necessary to construct a template in frequency space based upon $chop_{\mathrm{enc}}$. The Fourier transform of a sample chop timestream is given in Fig. 4.5.

While the chop signal contained a relatively clean Fourier transform, the fourier transform of the data contained significant low and high frequency contributions. These were filtered at the beginning of the routine using a low-frequency filter, $f_l(\mathbf{x})$ with a gaussian profile, defined by:

$$f_1(\mathbf{x}) = 1 - exp\left(\frac{-\mathbf{x}^2}{2\sigma^2}\right) \tag{4.7}$$

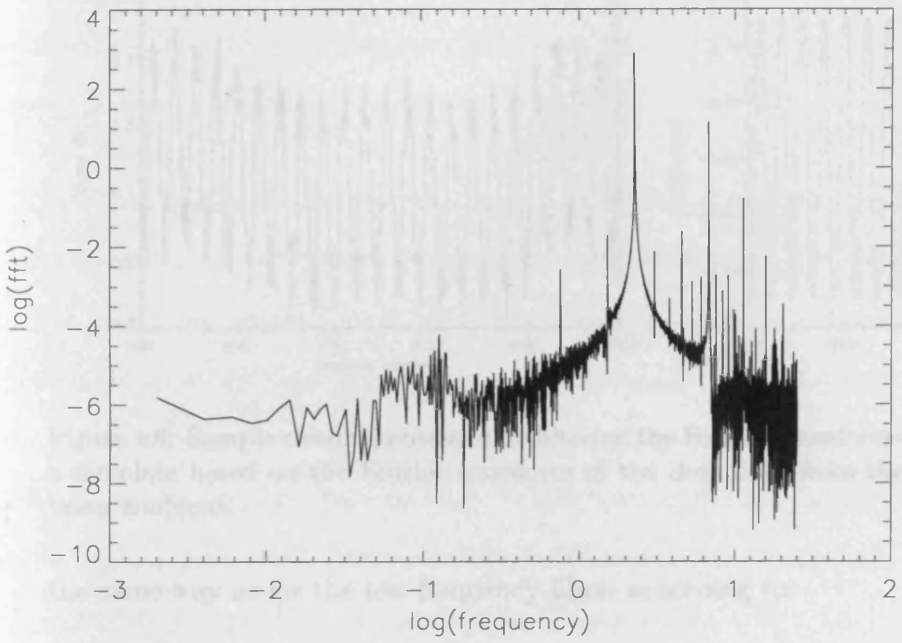

Figure 4.5: The Fourier transform of the chop signal from an observation file, plotted on logartihmic scales. The main contribution from the 2.25 Hz chop is clear.

where the width of the filter was characterised by the σ. The value of σ was chosen by trial and error: the filter had to be wide enough to eliminate the majority of the long wavelength signal, but not so wide that it also eliminated higher frequency signal that needed to be kept.

The remaining Fourier transform of the data was then multiplied by $f(x)$ to remove the low frequency contribution. The rest of the data filter was obtained by studying the derivatives of the chop Fourier transform. These derivatives were calculated simply by differencing consecutive data points, as before. Locating the maxima in the transform's derivative data was found to be a more reliable means of locating the peaks, since the derivative data contained less noise, but the peaks coincided with those in the transform itself. The position of the first peak of the derivative data was, therefore, found and a filter, $f_2(\mathbf{x})$, generated in almost exactly

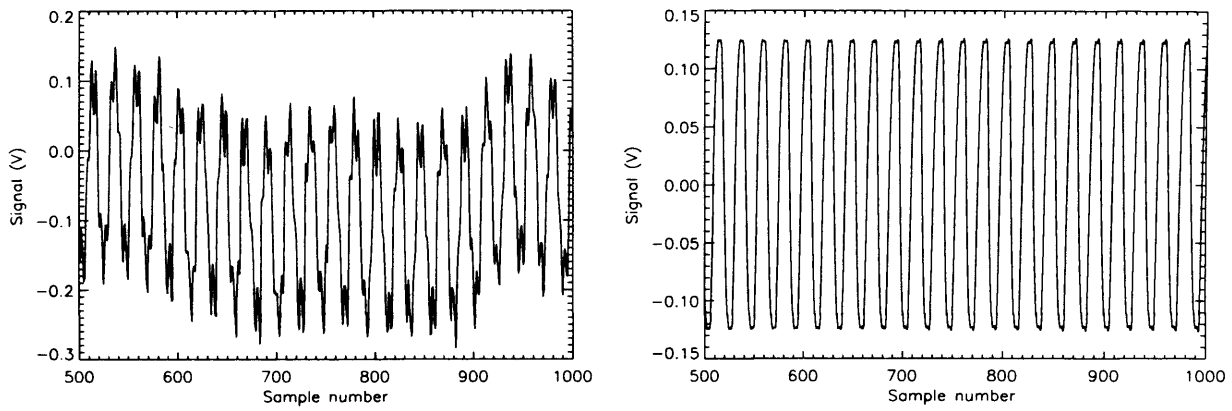

Figure 4.6: Sample cleaning obtained by filtering the Fourier transform of the data using a template based on the Fourier transform of the chop data from the observation file being analyzed.

the same way as for the low-frequency filter, according to:

$$f_2(\mathbf{x}) = 1 - exp\left(\frac{-(\mathbf{x}-p)^2}{2\sigma^2}\right) \tag{4.8}$$

where the p represents the location of the peak. The value of σ was chosen to be the same as for the low-frequency filter. The location of the next peak was calculated by filtering chop_enc derivatives using $f_2(\mathbf{x})$ and locating the next maximum. In general, chop_enc rarely contained more than three peaks, and the code was therefore designed to calculate only the first three peaks in the derivative data. The total filter, $F(\mathbf{x})$ was given by:

$$F(\mathbf{x}) = f_1(\mathbf{x}) - \sum_i exp\left(\frac{-(\mathbf{x}-p_i)^2}{2\sigma^2}\right) \tag{4.9}$$

where the p_i values are the locations of the peaks.

This effect of this cleaning is demonstrated in Fig. 4.6. The figure on the

left shows a sample of data prior to filtering; the figure on the right shows the data after filtering. The low frequency components of the data have clearly been removed, as have some of the higher frequency noise.

One of the important drawbacks of any type of cleaning based upon filtering the Fourier transform of the data is that some signal from the source itself will be lost. The signal that might be lost was expected to be small, but if would clearly be preferable to avoid this. Furthermore, the cleaning was not always entirely efficient, in particular at the beginning and end of the timestream, where up to $\sim$ 10% of the chop signal could be lost. [1] Calculating Fourier transforms in idl is also a lengthy procedure. This resulted in the cleaning module in the pipeline being very slow, especially since the data timestreams were long.

A more time-efficient method of cleaning the data was to use 'average subtraction'. This method uses the fact that the atmospheric noise in a given subsection, i.e. at a given time during the observations, remains relatively constant across all the bolometers, since the region of sky being imaged is smaller than the typical size of atmospheric cells . By calculating a value for the signal at each point in the datastream averaged across all the good bolometers, therefore, it was possible to reconstruct a template which represents the 'average datastream' in the observations. This was a good model for the baseline in the signal, and could then be subtracted from the raw data to obtain the signal due to astrophysical sources. An example of a template obtained using this method is given in Fig. 4.7. It is clear from Fig. 4.7 that some chopped signal is evident in the template. This is assumed to be from variations in the background between chop positions, and is not distinguished by the Fourier filtering method, which cannot discriminate between

[1] Although the telescope was never acquiring scientific data at the beginning and end of the observations, so this excess removal of signal should have little impact upon the maps obtained for the observation file.

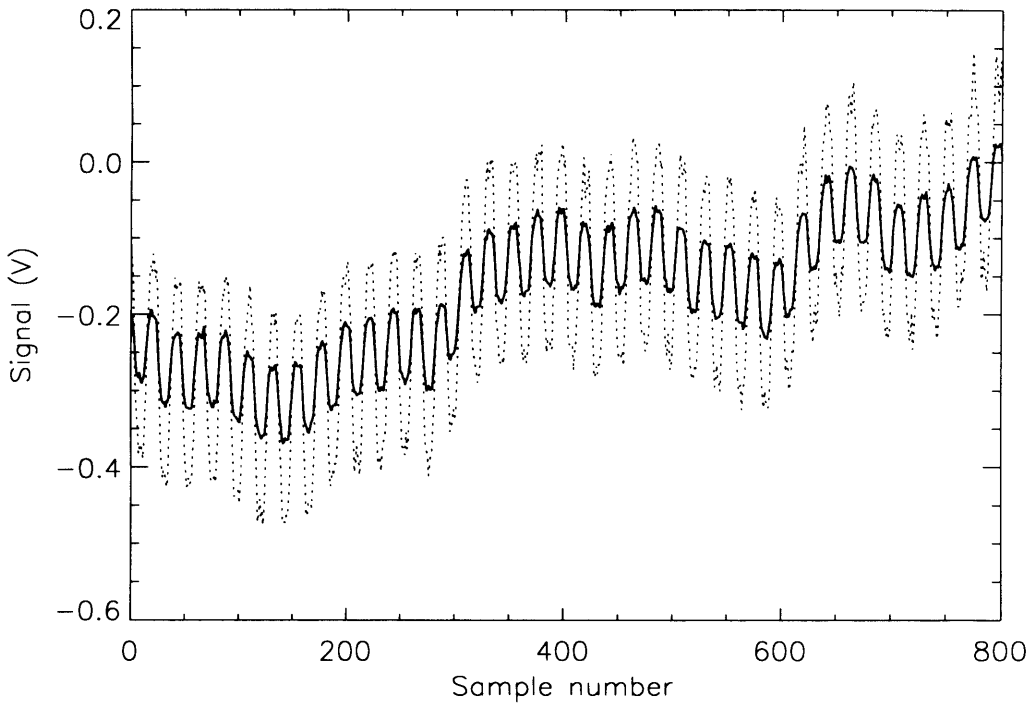

Figure 4.7: Template derived for one of the observation files in our dataset. The template is the solid line, while the dotted line is a set of data for one of the good bolometers. It is clear that the template also contains a chopped signal. This is, however, to be expected as it reflects the average difference in emission between the two positions as seen by all of the detectors in the array. This could be due to either atmospheric common mode emission, large scale astronomical emission or differential ground emission and spillover.

different signals at the same frequency.

The code for this was taken from the standard Bolocam pipeline. The clean timestreams are obtained by evaluating the matrix equation:

$$\mathbf{d}_{clean} = \mathbf{d} - \mathbf{CA} \tag{4.10}$$

where $\mathbf{d}_{clean}$ represents the cleaned data timestreams, $\mathbf{d}$ represents the raw, uncleaned, data, $\mathbf{A}$ is a 'template', defined by:

$$\mathbf{A}(j) = \frac{\sum_i \mathbf{d}(j,i)}{n} \tag{4.11}$$

where n is the number of good bolometers, j represents a specific bolometer, and the summation is carried out over the entire timestream for that bolometer. $\mathbf{C}$ is defined by:

$$\mathbf{C} = \frac{\mathbf{dA}}{\mathbf{A}^T\mathbf{A}} \tag{4.12}$$

Fig. 4.8 demonstrates the effect of average subtraction on the same sample of data displayed in Fig. 4.6. A straightforward comparison between Fig. 4.8 and Fig. 4.6 appears to show that the filtering method provides a much cleaner signal. This is, however, hardly surprising, since the Fourier filtering method is almost certain to produce a smooth signal due to the narrow width of the filters, which remove both high and low frequency components of the noise. Furthermore, as mentioned above, the Fourier filtering is unable to discriminate between chopped

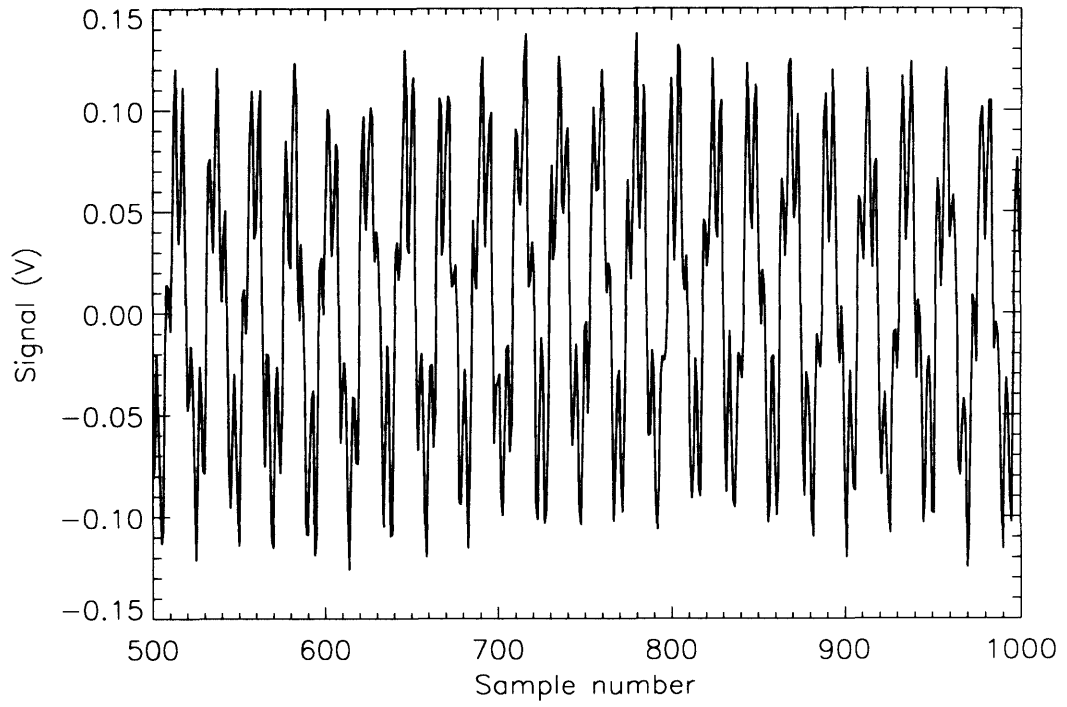

Figure 4.8: The effect of average subtraction upon the sample of data used to produce the plot in Fig. 4.6.

noise and chopped signal. This is evident from the different peak signals in Fig. 4.8 and Fig. 4.6, and makes average subtraction the preferable choice for removing baseline in the timestreams.

4.4 Phase differences

It was possible for phase differences between the chop data and the raw data to exist, due to, for example, differences in the clocks in the computers recording the chop and the computers recording the data. Clearly this needed to be accounted for accurately in order to carry out the demodulation.

The phase differences between the chop and the data were calculated by examining the individual on and off subsections from the cleaned data (i.e. data from which the baseline had been removed. The phase of the data, ϕ_{data}, was found by determining the value of ϕ_i that maximized:

$$L_i = \sum_i \mathbf{d}(\mathbf{s})\sin(\nu_{chop}\mathbf{s} + \phi_i) \tag{4.13}$$

where $\mathbf{d}(\mathbf{s})$ represents the data in the subsection being considered (and $\mathbf{s}$ represents the data positions included in that subsection); ν_{chop} is the chop frequency for the subsection being considered, as calculated previously and ϕ_i is the i'th value for the phase being tested in the fit.

The processing efficiency was increased by splitting this fitting procedure into two parts - the first which finds a rough estimate of ϕ_{data}, ϕ_{est}, by allowing ϕ_i to vary between 0 and 2π with a stepsize of 0.2 radians, and a second which then

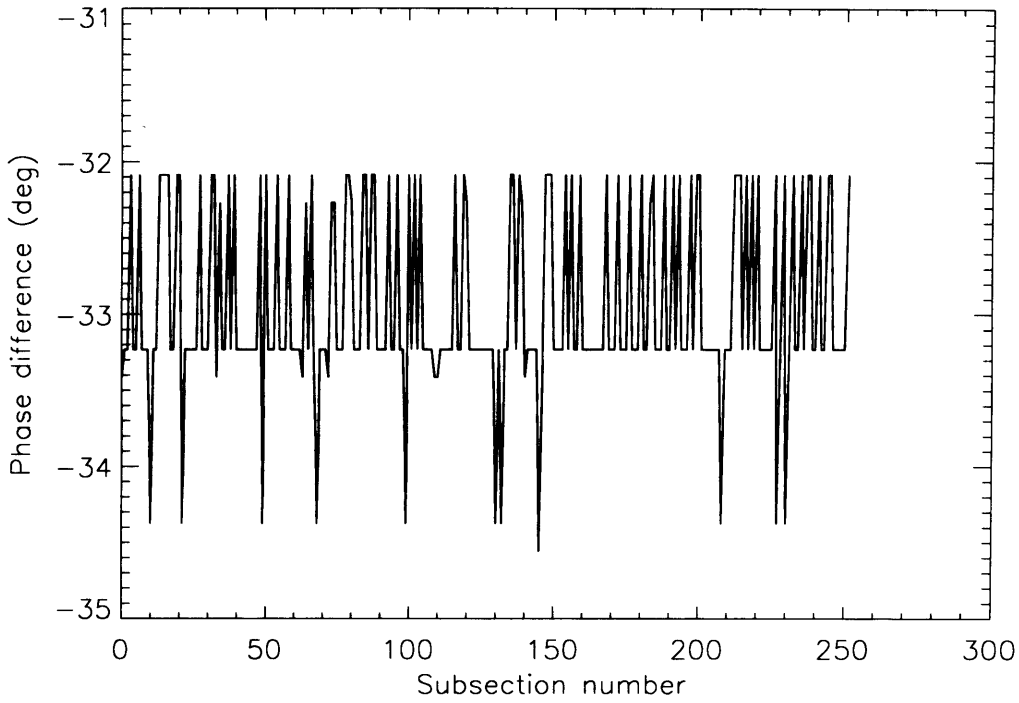

Figure 4.9: Phase differences between the chop timestream and the raw data for each subsection in the timestream from file 060131_o46_raw.nc (Abell 1835).

refined ϕ_{data} by restricting the range for ϕ_i to $\phi_{est} \pm 0.2$ and reducing the stepsize to 0.02 radians. This gave an estimate of ϕ_{data} to within approximately a degree, which was considered accurate enough for the demodulation, particularly since the values of ϕ_{data} were averaged in the later stages of demodulation (see below).

The phase of the chopper signal had already been calculated in a previous section of the pipeline, but were recalculated here using the method described above. The phases for the data and the chopper were then simply subtracted, and the subsequent phase differences for each subsection recorded and stored. Fig. 4.9 demonstrates a typical set of phase differences for a given bolometer.

The source of the phase differences is believed to be timing differences between the clocks in the different computers recording and storing data from the telescope.

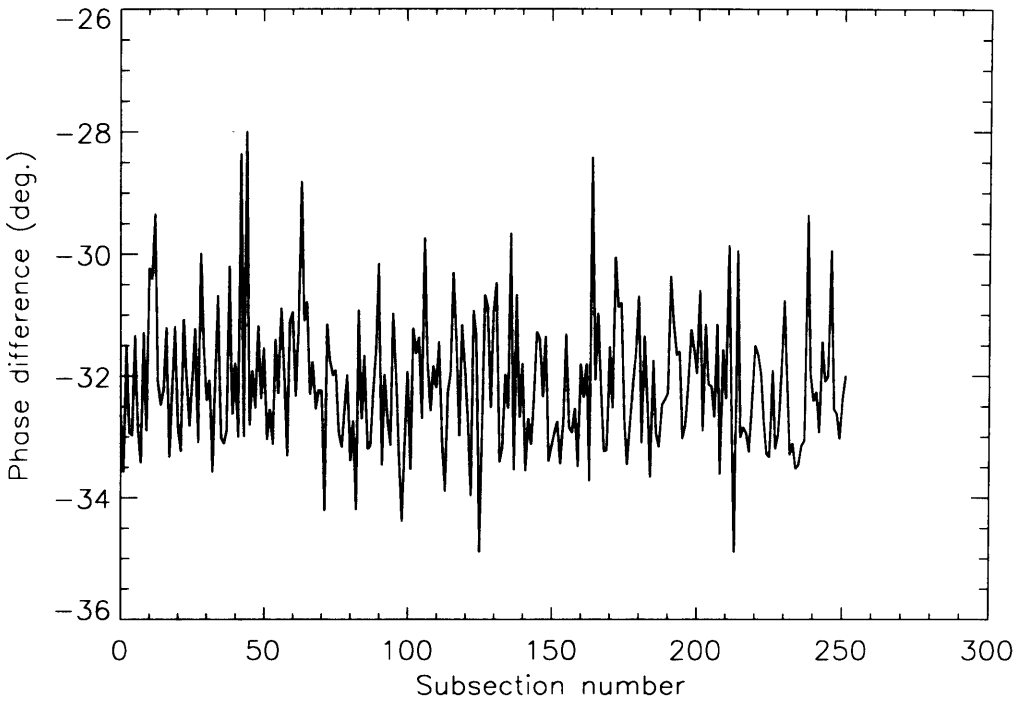

Figure 4.10: Representative set of mean phase differences per subsection, obtained by averaging across all the good bolometers in a datafile. There is clearly a consistent value for the phase throughout the file, although there is some variation about it.

The data in Fig. 4.9 appears to vary about a value of $-33.2°$ (equivalent to a couple/ few time samples in the timestreams), in discrete steps of $\sim 1°$, although some smaller variations are present. The values of phase difference also do not appear to correlate with what stage in the nodding cycle the observations are, which is consistent with the source of the phase differences being differences in computer clocks.

The phase differences were also expected to be independent of the specific bolometer being analysed and effectively constant with time (changes in the computer clocks may well occur with time, but significant differences would not be expected on the timescales of the observations). Fig. 4.10 demonstrates this effect, by calculating the mean phase difference in each subsection, averaged over

all the good bolometers. There is clearly a consistent value of phase difference between the chop and data, although individual measurements of this phase can vary by small amounts.

The phase differences obtained by observing different sources on different nights also demonstrate a reasonable consistency, although there were some files that exhibited systematic variation from the general value. The phase differences still, therefore, had to be calculated for each file (rather than an average value being chosen for all files, see Fig. 4.11).

The fit to the chop signal could then simply be transferred into the timeframe of the data simply according to:

$$\zeta(\mathbf{x}) = \sin(\nu_{chop}\mathbf{x} + \phi_{chop} + \Delta\phi_{mean}) \tag{4.14}$$

where $\zeta(\mathbf{x})$ represents the effect of the chopping in the timeframe of the raw data; ν_{chop} is the chop frequency for a given subsection; ϕ_{chop} is the phase difference of the chop data for a given subsection, derived from the raw chop timestream (chop_enc), and $\Delta\phi_{mean}$ is the mean phase difference for the observation file being processed, as discussed above.

4.5 Demodulation

With the phase information stored, all that was required to complete the demodulation therefore was to reconstruct the variation in the signal due to the scan strategy according to (4.14). The reconstructed signal $\zeta(\mathbf{x})$ for a specific subsec-

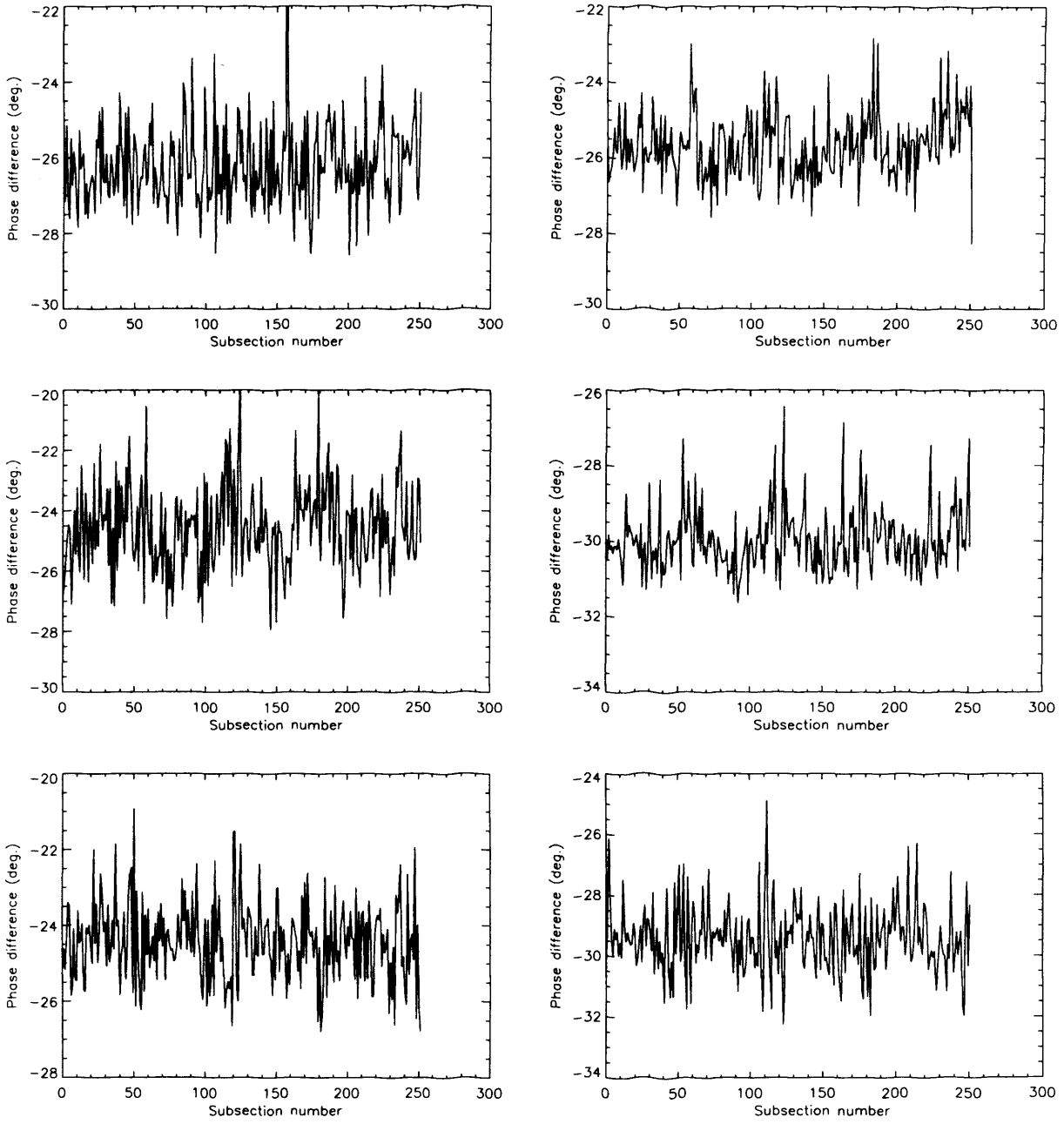

Figure 4.11: Mean phase differences for each subsection in a selection of Abell 1835 observations, made on different nights between 31st Jan 2006 and 4th Feb 2006. The data in these figures demonstrates that, while the general trend of the phase differences were similar for each file, there was variation, and a single value for the phase difference could not be relied upon in the analysis.

tion was then used to extract the signal in that subsection, A_{sub}, according to (3.3), which, in terms of vectors of data, is given by:

$$A_{sub} = \frac{\sum \zeta(\mathbf{x}) D(\mathbf{x})}{\sum \zeta(\mathbf{x})^2} \tag{4.15}$$

where $D(\mathbf{x})$ is the data in the subsection.

This simple process was only complicated by the fact that the length of the vectors in (4.15) had to represent an integer number of chop cycles. If an incomplete set of cycles were used in the summation, significant errors in the signal could result [3]. The integration lengths were calculated simply by working out the number of cycles in a subsection (based upon the chop frequency), then truncating this number to leave an integer number of cycles. In general, the integration length turned out to be 443 samples (8.9 s observing time).

The signal was calculated according to (4.15) for each on and off subsection. Given that one nod constituted a set of on, off, off, on sequence, the results had to be combined by differencing the average signal in the on subsections, $\bar{A}_{on}$, and the average signal in the off subsections, $\bar{A}_{off}$:

$$A_{nod} = \bar{A}_{on} - \bar{A}_{off} \tag{4.16}$$

The error in this value, $\sigma(A_{nod})$, was then calculated by weighting A_{nod} by the number of elements in the on and off subsections according to:

$$\sigma^2(A_{nod}) = \frac{\sum A_{nod}^2 w}{\sum w} \tag{4.17}$$

where the summation is over all nods in an observation file, and w is given by:

$$w = \frac{n_{on} n_{off}}{n_{on} + n_{off}} \tag{4.18}$$

Here, n_{on} and n_{off} are the total number of elements used in the on and off sections, respectively.

4.6 Mapping

The section of code that deals with mapping of the demodulated, calibrated data uses a standard routine taken directly from the Bolocam standard analysis pipeline. The pointing source files were the first to be mapped. Since these were to be used to determine the calibration for the observations, the signal in these files was initially stored in Volts. When mapping science sources, however, the data had to be converted to mJy using the calibration conversion (see Chapter 5: 'Pipeline Development II: Pointing, Calibration and stacking').

The signal arrays were converted into one-dimensional vectors. The locations on the sky being observed by individual bolometers throughout the observations were also passed as one-dimensional vectors into the standard mapping routines. This required the positions of each pixel relative to the centre of the telescope beam to be calculated, and the equivalent R.A. and decl. information to be adjusted accordingly for each sample from each bolometer. Extracting the R.A. and decl. values was carried out individually for each file. This process is discussed in more detail in the next Chapter.

In this chapter, we have outlined the basic operation of the main demodulation section of the pipeline code. Next, we will review how that demodulation was incorporated into a complete routine to generate maps of science sources.

Chapter 5

Pipeline Development II: Pointing and calibration

A number of well-known bright sources close to the science targets were also observed during the run. These sources were used to determine the calibration required to convert the raw data from units of volts to units of flux, as well as to deduce the positions on the sky that the signal from individual pixels represented (referred to as 'pointing').

Pointing and calibration sources can be classified as either primary or secondary. Primary sources are generally planets, whose flux and variability are well-known and can, therefore, be considered reliable for calculating the calibration. Secondary sources include, for example, protostellar sources, HII regions and evolved stars. These sources are still bright, relative to the science sources which are the targets of the observations, but their flux may not be as well-known, and their variability more uncertain.

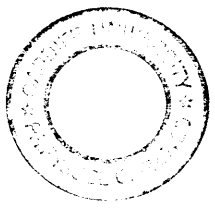

Source name	RA (B1950)	Dec (B1950)	RA (J2000)	Dec (J2000)	1.1 mm Flux (Jy)
0420m014	04h20m43.5s	-01°27'28.8"	04h23m15.8s	-01°20'33.1"	1.3
0458m020	04h58m41.3s	-02°03'33.4"	05h01m12.8s	-01°59'14.3"	1.2
0923p392_4cp39.25	09h23m55.3s	39°15'23.5"	09h27m03.0s	39°02'20.9"	2.2
1334-127	13h34m59.8s	-12°42'09.8"	13h37m39.8s	-12°57'24.7"	4.3
3c371	18h07m18.5s	69°48'57.1"	18h06m50.7s	69°49'28.1"	0.6

Table 5.1: Positions and 1.1 mm fluxes for the secondary pointing sources used in the observing run. Two sets of positions are included for each source, which are recorded for different epochs. The B1950 coordinates are those supplied with the 1.1 mm flux measurements. The J2000 coordinates are taken from measurements of the sources at 0.85 mm. All data from the Bolocam pointing source archive.

The majority of the pointing sources used for the Bolocam observations were secondary, although there were also a number of observations of Mars made during the run. Table 5.1 gives the fluxes and positions of the secondary sources used.

Maps of the pointing and calibration sources are given in Fig. 5.1 - Fig. 5.5. The quality of the pointing source maps varied considerably. The pointing source observation files were much shorter than the science source files and the coverage of the maps (i.e. the number of observations per pixel) could vary significantly. This was particularly significant in the central regions of the maps, where low coverage could lead to empty pixels in the region of the source itself.

5.1 Pointing

Whereas the pointing for the science maps was based upon the pointing and calibration sources, clearly a different approach had to employed to obtain the correct inital pointing for the pointing and calibration sources themselves. The process by which this was achieved is described below.

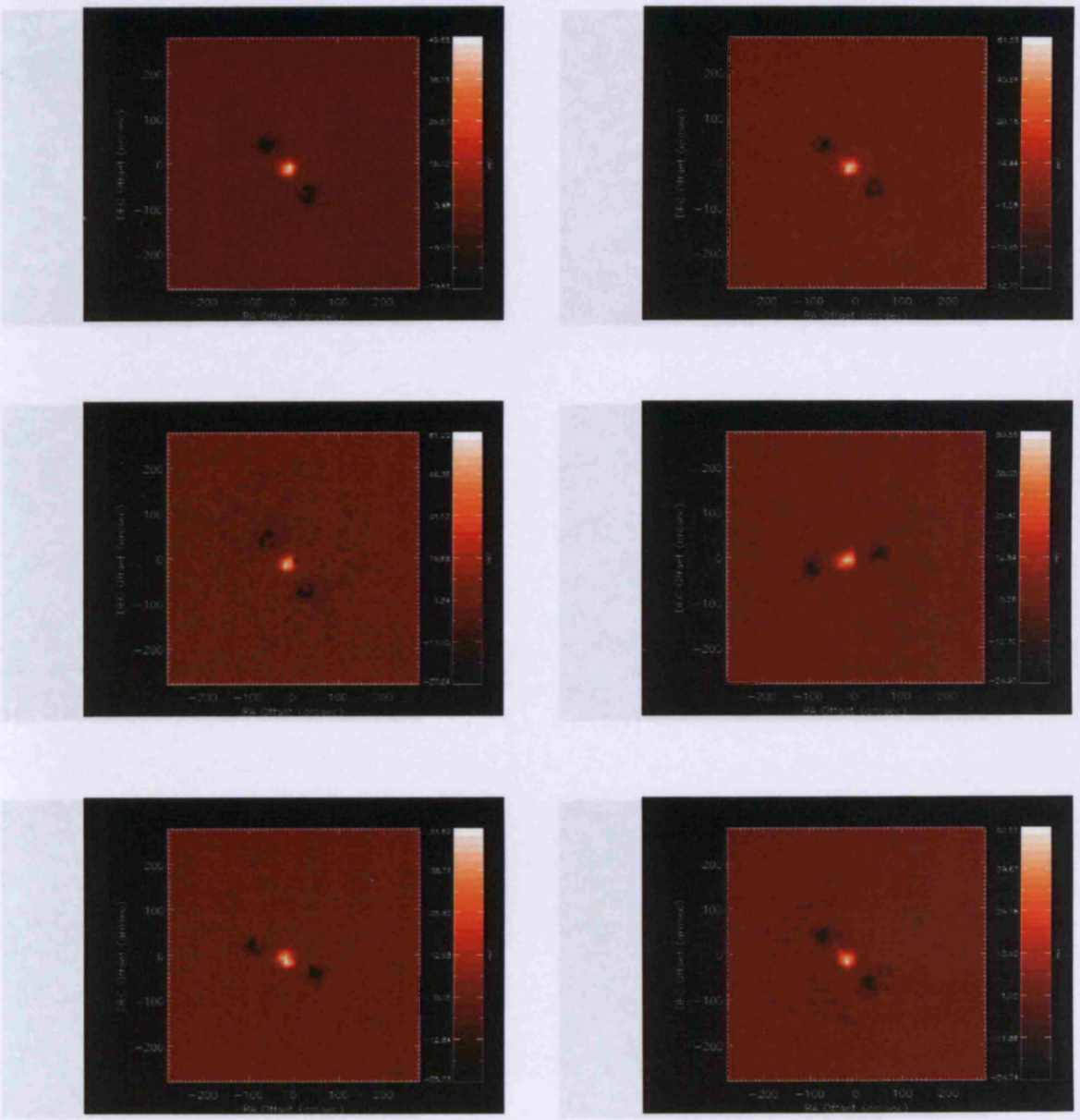

Figure 5.1: Pointing maps for a representative set of the 0420m014 observations.

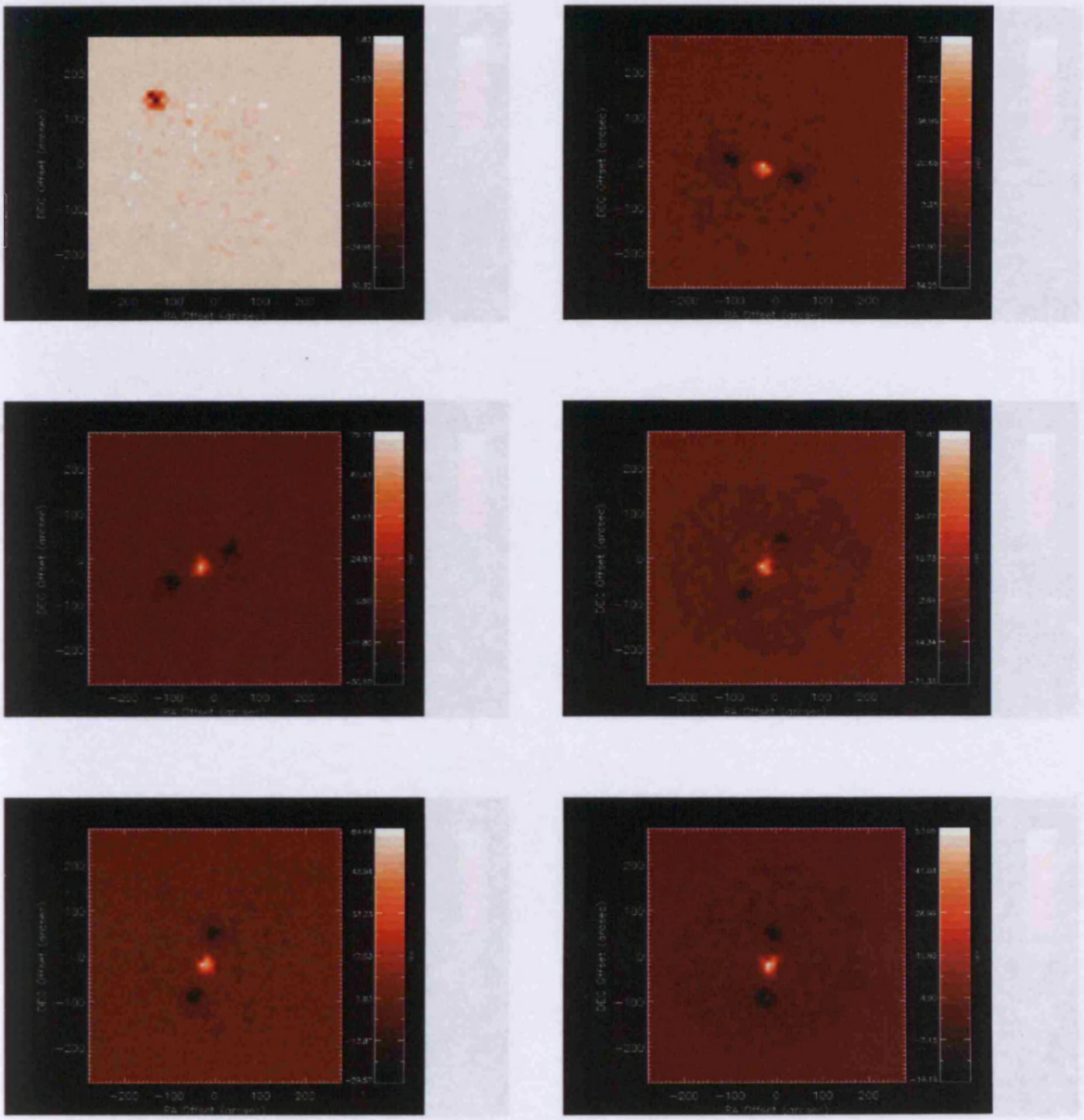

Figure 5.2: Pointing maps for a representative set of the 0923p392_4cp3925 observations.

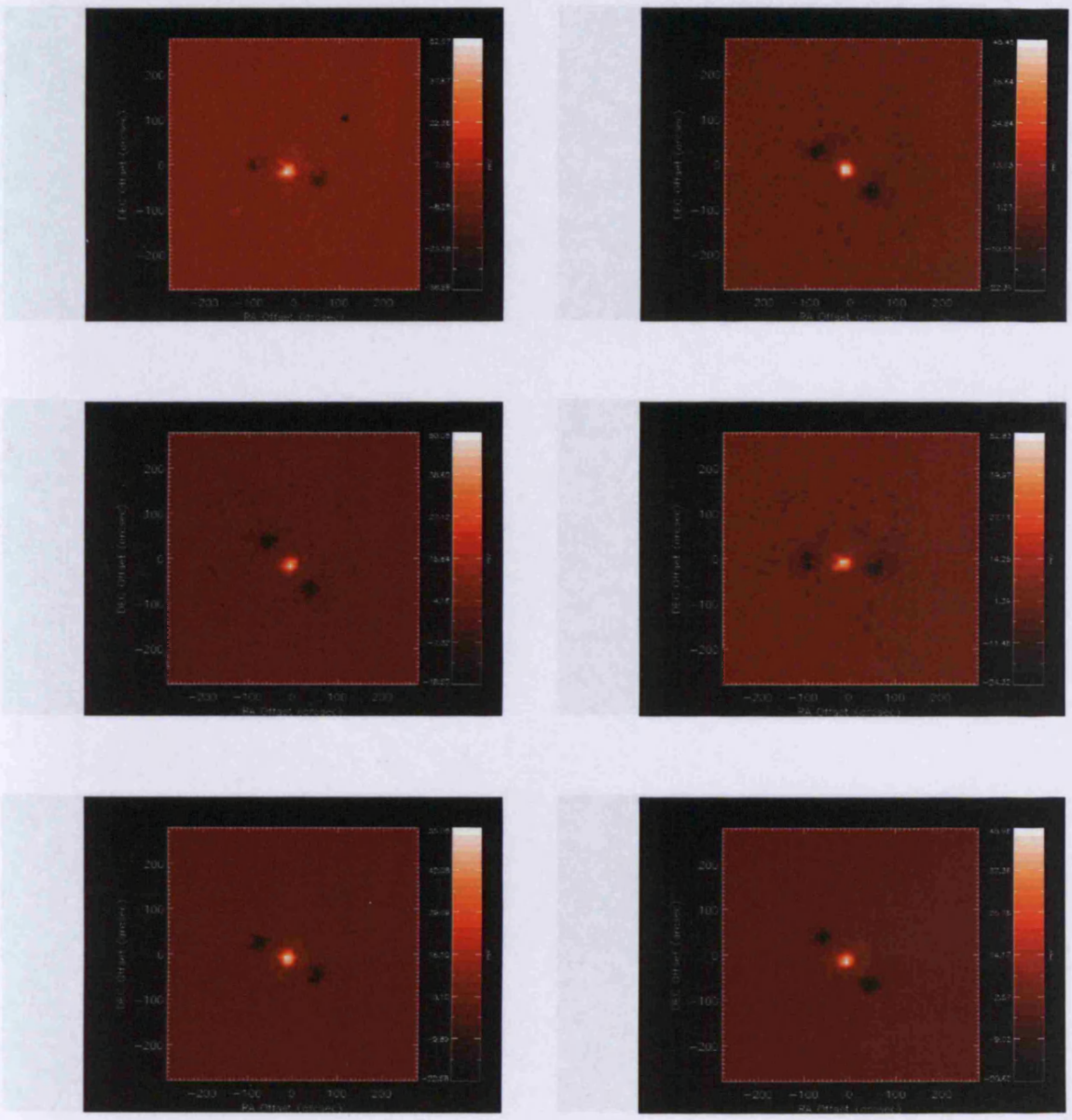

Figure 5.3: Pointing maps for a respresentative set of the 1334-127 observations.

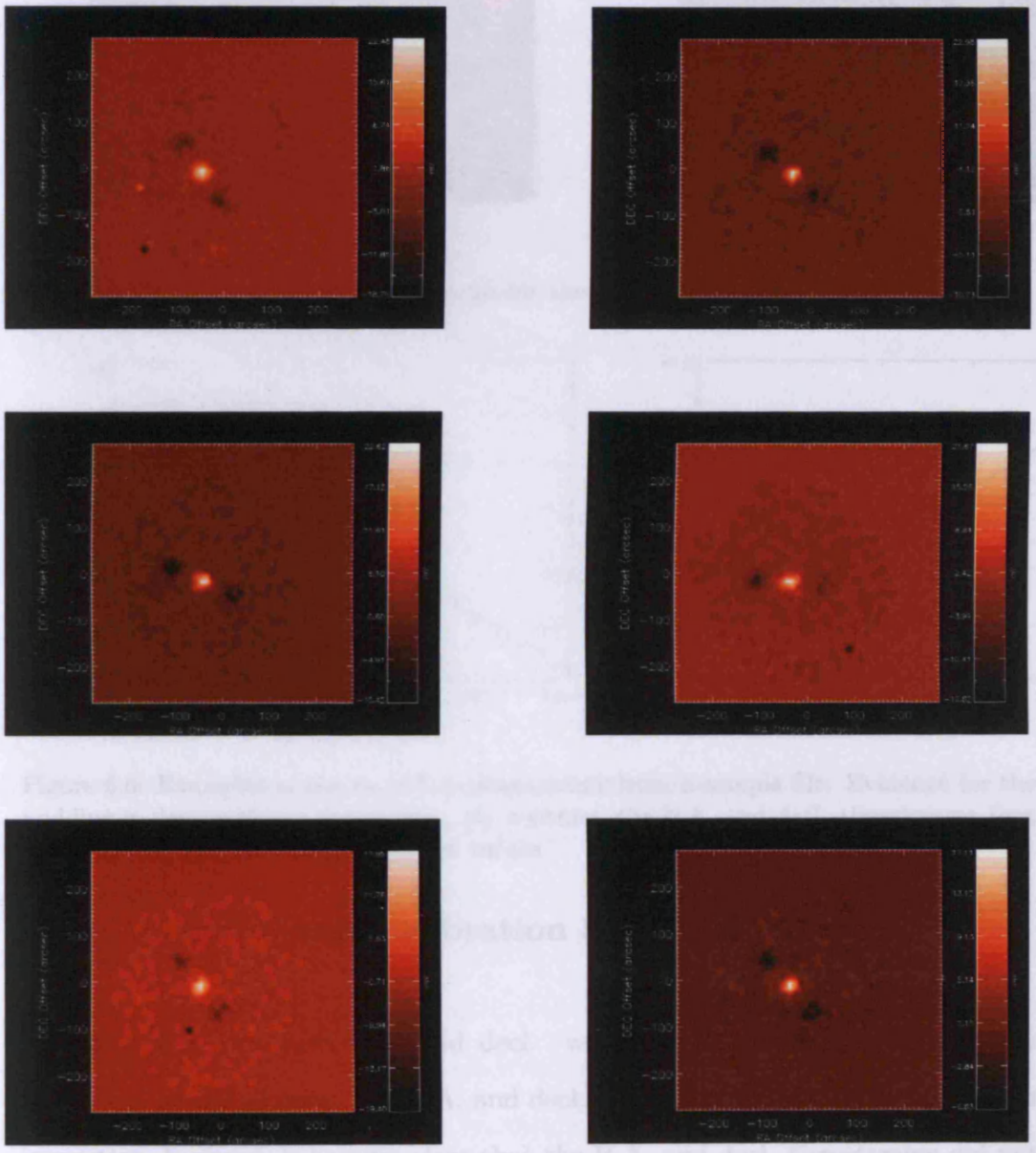

Figure 5.4: Pointing maps for a represetative set of the 3c371 observations.

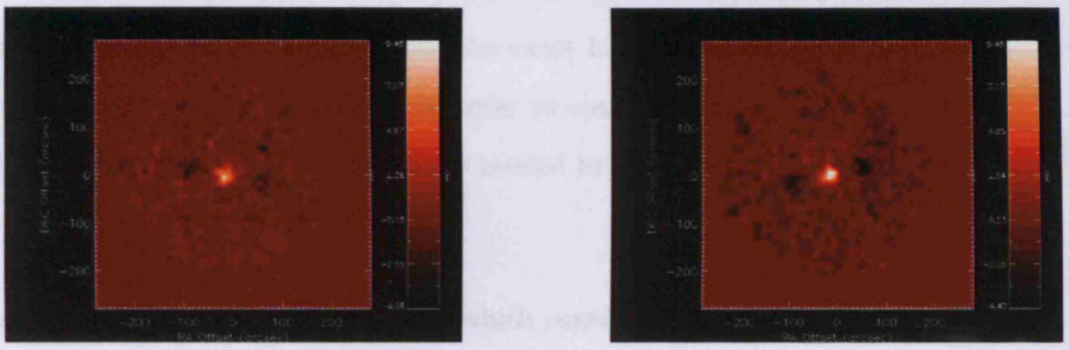

Figure 5.5: Pointing maps for the 0458m020 observations.

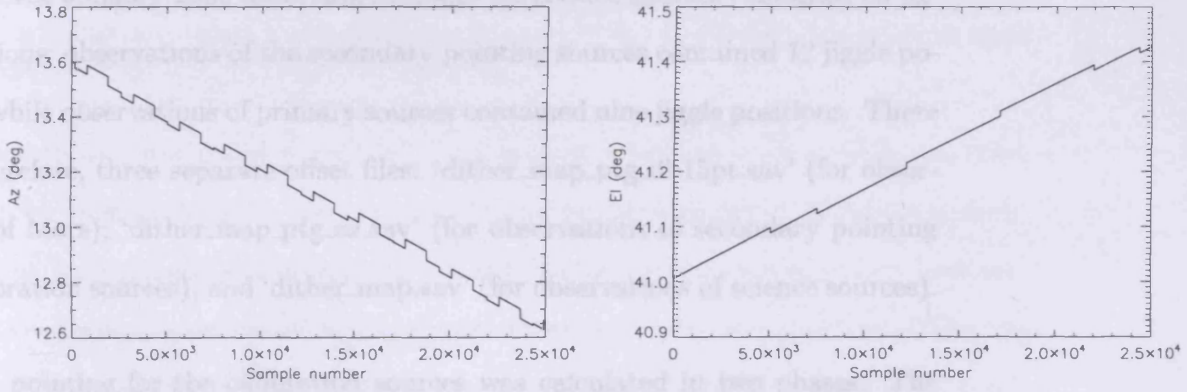

Figure 5.6: Examples of the az and el timestreams from a sample file. Evidence for the nodding is clear in the az timestream. By contrast, the R.A. and decl. timestreams (not shown above) contained only constant values.

5.1.1 Pointing and Calibration Sources.

The data files contained R.A. and decl. values for the telescope while it was observing; az and el data, and R.A. and decl. values for the science source. Upon inspection, however, it became clear that the R.A. and decl. timestreams did not appear to contain information on the nodding of the telescope, whereas the az and el timestreams did (see Fig. 5.6). It was clear, therefore, that the az and el data had to form the basis of the pointing reconstruction.

The situation was complicated, however, since the az and el values stored during the processing did not correspond with the exact location of the centre of the field of view of the telescope in the sky. In order to obtain the actual position on the sky that the telescope is observing, offsets needed to be added to the stored values.

The standard Bolocam pipeline stores files which contain approximate offsets for different targets. The offsets are expected to change, depending on the altitude and elevation of the telescope dish. Thus, offsets are recorded for each jiggle position. For the January 2006 observing run, files for science sources contained 63 jiggle locations; observations of the secondary pointing sources contained 12 jiggle positions, while observations of primary sources contained nine jiggle positions. There were, therefore, three separate offset files: 'dither_map_ptg_db15pt.sav' (for observations of Mars); 'dither_map_ptg_az.sav' (for observations of secondary pointing and calibration sources), and 'dither_map.sav' (for observations of science sources).

The pointing for the calibration sources was calculated in two phases. The initial phase involved finding a mean offset between the values of az and el stored in the ncdf files and the real sky values. The telescope was, in general, assumed to be pointing in the direction of the pointing and calibration source ('source_ra' and 'source_dec' in the ncdf file). The archive offsets were then added to the corresponding alt and az values and compared to the alt and az timestreams stored in the ncdf file for each subsection in an observation file. The offsets determined for individual subsections were found to be generally consistent, and an overall offset for the file was determined by taking the average value from these results.

The overall offsets calculated in this manner are displayed in Fig. 5.7. There is clearly a general trend in both sets sets of offsets. The average azimuth offset

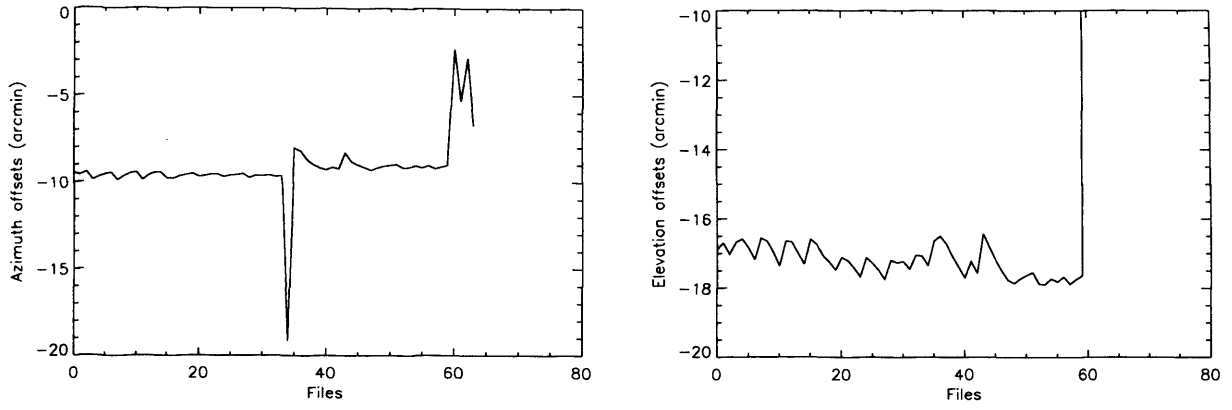

Figure 5.7: Initial offsets between archive source positions and the position timestreams saved in observation files for all the pointing and calibration sources. Consistent offsets are observed for both azimuth and elevation, although there is some scatter. The sources with the largest variation from the mean (corresponding to the final datapoints in these plots) were derived from Mars observations.

over all files was found to be -9.2 ± 1.8 arcmin, while the average elevation offset (not including the Mars observations - see figure caption), was -17.2 ± 0.4 arcmin. Since the precision of the pointing was anticipated to be 10 arcsec or less, however, the variation in the results was too great to use a general average (over all files) in the analysis, and the initial offsets continued to be calculated for individual files.

The next phase of the pointing was to derive small adjustments for a given file. The pointing was reconstructed from the mean offset calculated in the first phase and the az and el data in the ncdf file. The location of the point source in the resulting map was then found by using a fit, which was designed to locate the region of the map which matched closest the expected ideal profile for a point source. Using a fit avoids the potential for so-called 'flux boosting' to distort the results. Flux boosting occurs when low significance noise features are coincident with regions of real signal (even though these regions may not represent the true peak in intensity of the source being studied). The presence of the noise distorts the significance of individual pixels and could, therefore, lead to false readings of

peak intensity.

In the fit, the point source intensity profile was simulated as a gaussian with full-width-half-maximum (FWHM) of 30" (i.e. the result of convolving a delta function with the beam profile of the instrument). This model was not precise, but was adequate for detecting the location of the peak of the point source flux. The beam model was a 7×7 pixel template, which was fitted to 7×7 sections of the pointing source maps, M. The degree of matching between the beam profile and the map section was determined using:

$$\lambda = \sum_{i,j} n_{i,j}(M_{i,j} - \bar{F}B_{i,j})^2 \tag{5.1}$$

where λ represents the 'goodness-of-fit', and the summation was carried out over all the pixels, i and j, in each of the maps; $n_{i,j}$ represents the coverage in each pixel; $B_{i,j}$ is a 7×7 map of the telescope beam (centred on the central pixel of M), and $\bar{F}$ represents an averaged signal over all the pixels in M_s (which, once convolved with the beam, produces the template for a point source in the 7×7 segment), determined by:

$$\bar{F} = \frac{\sum_{i,j} M_{i,j}B_{i,j}n_{i..j}}{\sum_{i,j} B_{i,j}Bi,jn_{i,j}} \tag{5.2}$$

The process was complicated by the fact that the coverage was incomplete for many of the pointing source maps, even in regions close to the point sources. This could change the position of the minimum χ^2 in a given map and had to be accounted for within the routine. This involved, for example, checking that the signal in the pixel at the location of the minimum χ^2 was approximately equal

to the maximum signal in the map. Despite flux boosting affecting pixels in the centre of the map, it was expected that the flux at the true centre of the pointing source emission should be large, so the approximation was reasonable.

Once the approximate center of the emission had been located, the difference between its location (according to the adjusted alt and az timestreams) could be compared to the archived values in order to obtain the final pointing correction for these maps. These values were stored for later use in the processing of the science sources.

5.1.2 Science Sources

Once both sets of offsets had been obtained and stored for the pointing and calibration sources, the pointing for the science sources could be addressed.

The first stage of this process was identical to that for the pointing and calibration sources. The stored az and el values were compared to the source az and el (adjusted by the archived offsets), and a mean difference between the two obtained. Clearly, however, the individual maps of science sources were expected to be too low signal-to-noise (S/N) for the same method to be employed in deriving the smaller offsets.

Typically, the final adjustment to the pointing in observations of science sources is performed by generating a model for the size of the offsets which depends upon the az and el positions that the telescope is observing (since the offsets are expected to be a result of, for example, distortions in the telescope structure, which will be a function of its position and arrangement at a given time), derived from the offsets determined from the pointing and calibration sources (discussed above).

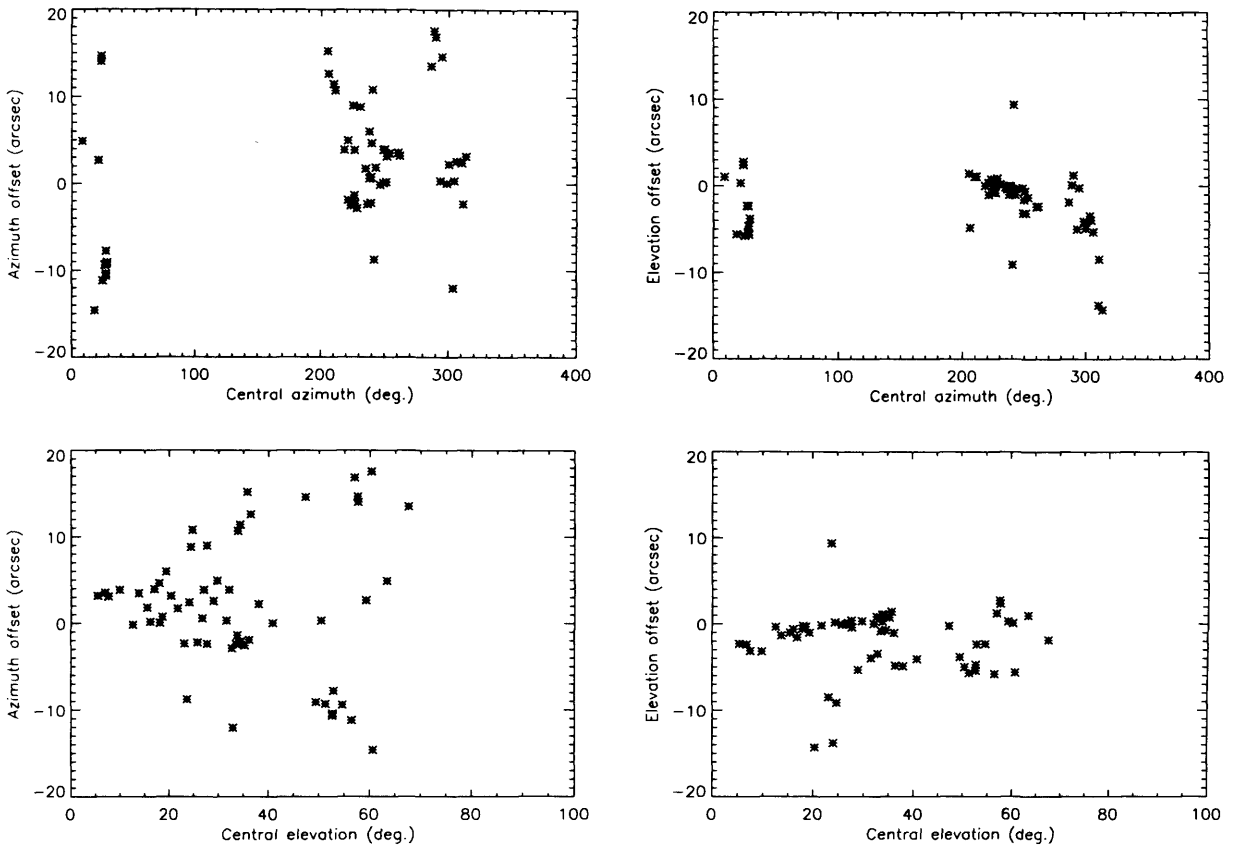

Figure 5.8: Plots of az and el offsets compared to the central az and el of the telescope for pointing and calibration sources observed during the run. There appears to be little evidence of a straightforward correlation between either of the offsets and the direction in which the telescope is pointing.

The model is then used to calculate the expected offset for a specific science source given the az and el timestreams stored for that source.

Initial plots of the offsets against central az and el, however, detected no obvious relationship between position and offset (see Fig. 5.8). More complex relationships between the positions and offsets also showed no definite pattern. Furthermore, despite there being over fifty individual observation files, for more complicated functions of central position coordinates the parameter space became increasingly poorly sampled, and a reliable functional relationship between the

offsets and the sky coordinates became correspondingly difficult to obtain.

The small offsets were, therefore, eventually determined simply by using the offsets for the pointing and calibration sources that were observed directly before or after the observations of the science source being processed. These offsets were expected to be extremely close to the offsets for the science sources, since the pointing sources were chosen to be close to the science targets they bracketed. An additional test was to ensure that the offsets from the pointing sources were similar, implying that the variation in the offset value when the telescope was pointing in that region of the sky was small, and that the assumption that the science source itself would have a similar offset was reasonable.

5.2 Calibration

5.2.1 Calibration based on secondary calibrators

Once the position of the pointing sources had been determined, the signal of that source (in mV), S_{mV}, could be read and compared to archive values for the source' fluxes (in mJy), S_{mJy} (5). The calibration factor, F_{calib}, for that source could then be calculated simply as:

$$F_{calib} = S_{mJy}/S_{mV} \tag{5.3}$$

Once calibration factors for all the pointing sources had been calculated and stored, it was possible to use them to calculate the calibration factors for the science sources.

The standard means for determining the calibration factors required to convert the data from voltage measurements to flux values for Bolocam is to plot the calibration factors for the pointing sources against the bolometer operating resistance, represented by measurements of the dc level of the lock-in amplifier output [126].

This method works because the flux calibration, in units of V/Jy (or equivalent), is proportional to the atmospheric transmission and the bolometer responsivity. The bolometer responsivity is expected to be a monotonic function of the bolometer resistance. Similarly, the bolometer resistance decreases monotonically as the atmospheric loading increases, and the atmospheric loading increases monotonically as the atmospheric transmission decreases. The atmospheric transmission is, therefore, also expected to be a monotonic function of bolometer resistance, and so too the combination of atmospheric transmission and bolometer responsivity (i.e. the flux calibration).

This resistance is measured by monitoring the median dc lock-in voltage, since this is proportional to the resistance (Ohm's law). By plotting dc levels against calibration factors for sources of known flux, therefore, it is possible to obtain an empirical relationship between flux calibration and median dc-signal. The resulting plot generally has a quadratic form and can be fit to determine the coefficients that define the functional relationship. By calculating the dc signal in maps of science sources the corresponding flux calibration could then be determined.

The previous version of the calibration curve for Bolocam was based upon measurements of primary pointing and calibration sources made in May 2004. The curve is defined by a quadratic relationship:

$$F_{calib} = \sum_{i=0}^{2} A_i D_s^i \tag{5.4}$$

where D_s represents the dc signal of the source, and A_i are the coefficients of the fit, which are given as:

$$\begin{aligned} A_0 &= -3.334 \times 10^{-3} \\ A_1 &= -2.926 \\ A_2 &= 6.973 \end{aligned} \tag{5.5}$$

The calibration curve is expected to evolve with time as the components of the detector change, so needs to be re-checked periodically and updated when necessary. It was decided, therefore, to review the data to see if this re-assessment was required.

The dc signal from the pointing and calibration sources were obtained using the same pipeline as for the ac data. A keyword was simply added to the appropriate procedures to allow the user to define if the analysis should be carried out on the ac or dc timestreams, both of which were stored in the ncdf files for the observations.

The resulting plot of dc signal against calibration factor is given in Fig. 5.9. Not all of the pointing source maps were used in the plot, since some were too incomplete to produce reliable results, or simply contained poor data. Of those that remain, however, it seems clear that, while there is a modest scatter about

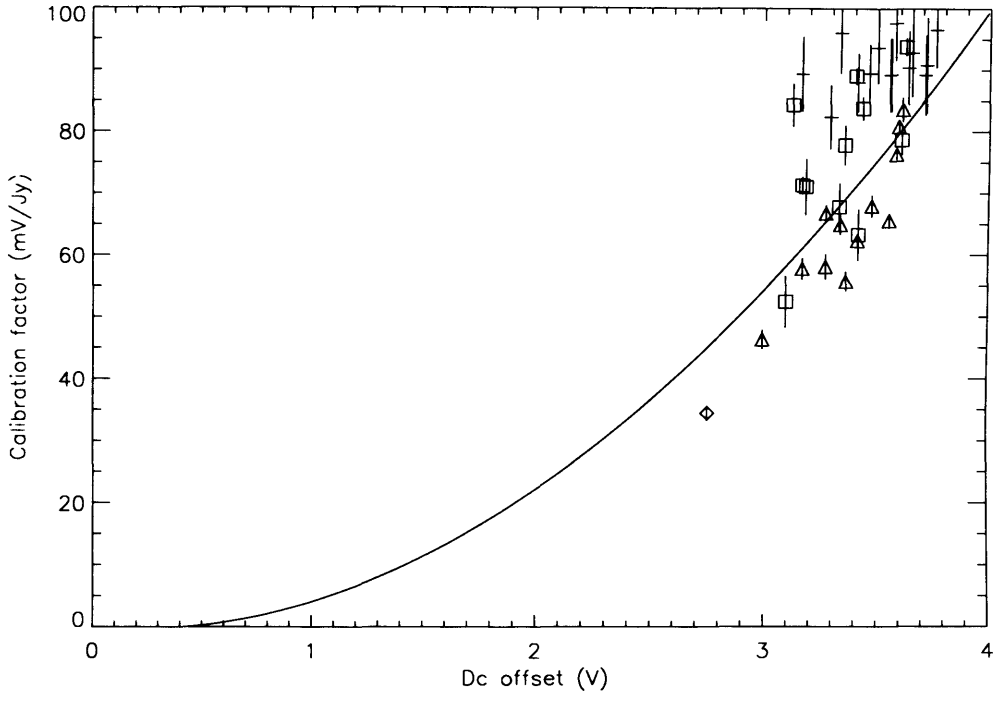

Figure 5.9: Calibration data. The May 2004 calibration curve is shown as the solid line. The error bars in this figure are statistical errors from the measured data. They do not, therefore, include intrinsic uncertainty in the source brightness. The data does not, on the whole, deviate substantially from the May 2004 curve. Legend: Vertical crosses: 0420m014; open triangles: 0923p392_4cp39.25; open diamonds: 1334-127, open squares: 3c371.

the May 2004 curve, the sources remain reasonably consistent with it.

While the scatter is significant, it is not necessarily surprising, since it is much harder to define a well-constrained calibration curve using secondary pointing sources. Although the sources are considered to have reasonably well-defined fluxes, differences exist between different surveys. Furthermore, the variability of secondary sources is often not well-known. It was not considered unreasonable that these uncertainties could introduce errors of order up to 10% in the data, which is of a similar order to the statistical scatter of the pointing sources in Fig. 5.9.

It has also been noted that the coverage per pixel in the pointing source maps could vary significantly, even in the portions of the maps that contained the sources themselves, and that this potentially represented a problem for the fitting procedure used to determine the position of the sources in the maps, described previously (see 5.1.1: 'Pointing and Calibration Sources'). While maps in which this was obviously a problem had been removed, it remained possible that some of the maps used in the calibration *had* been affected in this way.

Based upon this, therefore, no significant evidence was found to justify redefining the calibration curve for this analysis, and it was concluded that the May 2004 curve probably remained reasonably accurate.

5.2.2 Calibration based on primary calibrators

Ideally assessment of the calibration curve should be carried out using primary calibrators; most commonly planets. In the case of the Jan 2006 run, as has already been noted, there were a number of observations of Mars. During the initial stages of processing, however, two of these files had been discarded because

they contained bad nodding sequences.

The remaining Mars observation files were analysed in a similar manner to the secondary sources discussed above. The primary difference between the analysis of Mars and the other sources was that Mars was bright enough to saturate the bolometers when being operated with an ac-bias. For this reason, the dc_bolos timestreams were used to reconstruct maps. The dc_bolos timestreams essentially contained the same information as for the ac_bolos, but were less sensitive, and so were not saturated by the Mars observations.

In order to construct a calibration plot, however, the maps constructed using the dc_bolos data needed to be converted into equivalent ac signal. The multiplicative factor that separated the timestreams (referred to as the gain) could be calculated simply be comparing the dc maps for the secondary sources (discussed above) to the ac_bolos maps of the same sources. The gain was found to be 108.6.

Maps of the Mars observations are displayed in Fig. 5.10. It is immediately obvious that a number of the maps appear to be of poor quality, containing double-sources in the central portions.

In order to determine calibration factors based on planetary primary calibrators, the flux of the sources (in mJy) has to be estimated based on theoretical models. In this case, a simple blackbody model was used, where the flux, F, was given by:

$$F = \left(\frac{2ckT}{\lambda^4}\right) A\Omega \frac{10^{20}}{4\pi D^2} \tag{5.6}$$

where T and A are the temperature and surface area of Mars respectively

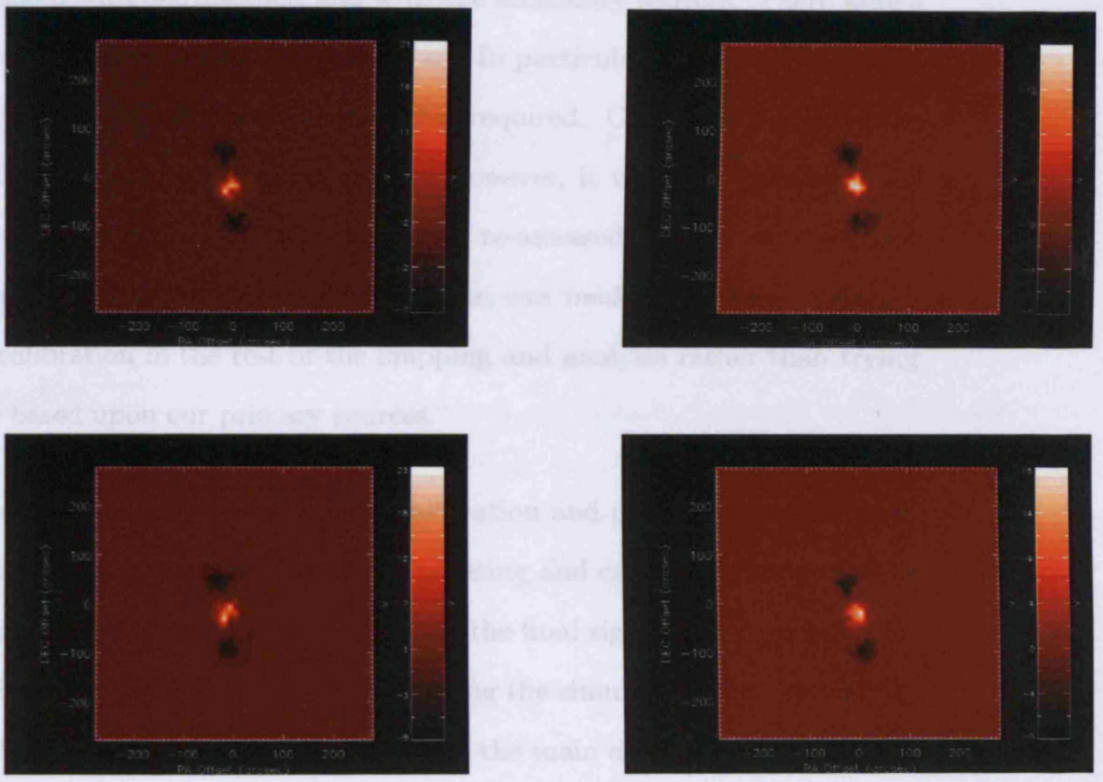

Figure 5.10: Mars maps, constructed using the dc_bolos timestreams, then converted into equivalent ac signal for including in the calibration curve analysis.

[1] ; Ω and D are the solid angle and distance of Mars from Earth at the time of the observations (taken from a separate set of data); λ is the wavelength of the observations, and c and k are the speed of light and Boltzmann constant, respectively.

When added to the calibration plots, however, the Mars points appeared to be poorly-correlated with one another, and with the secondary sources. There were a number of reasons why this may have been so. In particular, it is possible that a more refined model for the Mars emission was required. Given the results of the analysis of the secondary calibration sources, however, it was concluded that the May 2004 curve was probably not going to be re-assessed, even if improvement could be made in the Mars points. The decision was made, therefore, to simply use the old calibration in the rest of the mapping and analysis rather than trying to update it based upon our primary sources.

In this chapter we have discussed the calibration and pointing reconstruction for science maps based upon observation of pointing and calibration sources. The next chapter describes the process of producing the final signal and error maps for the cluster fields and interpreting the results using the simulation of emission from known sources. From this analysis, the fluxes of the main astrophysical sources in the field around Abell 1835 were extracted along with an estimate of the central Compton parameter for the cluster.

[1] Data taken from http://nssdc.gsfc.nasa.gov/planetary/factsheet/marsfact.html

Chapter 6

SZ Fitting: Analysis Code

Final maps for each cluster were generated by combining the chopped data from all the observations of a field and mapping as normal. Co-added S/N maps for Abell 1835, Abell 2218, Abell 851 and MS0451.6-0305 are given in Fig. 6.1. These maps have also all been convolved with the Bolocam beam to enhance the structure contained in them.

Abell 851 does not show any obvious cluster emission. Multi-frequency studies of the cluster have found a complex core and a significant level of substructure (e.g. [56, 150]), which cannot, therefore, be modelled simply. Recent research into Abell 851 has involved, for example, investigating the effect of starburst galaxies on galaxy cluster evolution [65, 150], but it is not an obvious target for SZ observations. It was decided, therefore, that Abell 851 was not suitable for an SZ study in this case. The bright sources in the field (and high S/N features), however, are associated with point sources, which have been studied previously (e.g. [49]), and were potential sources for further study.

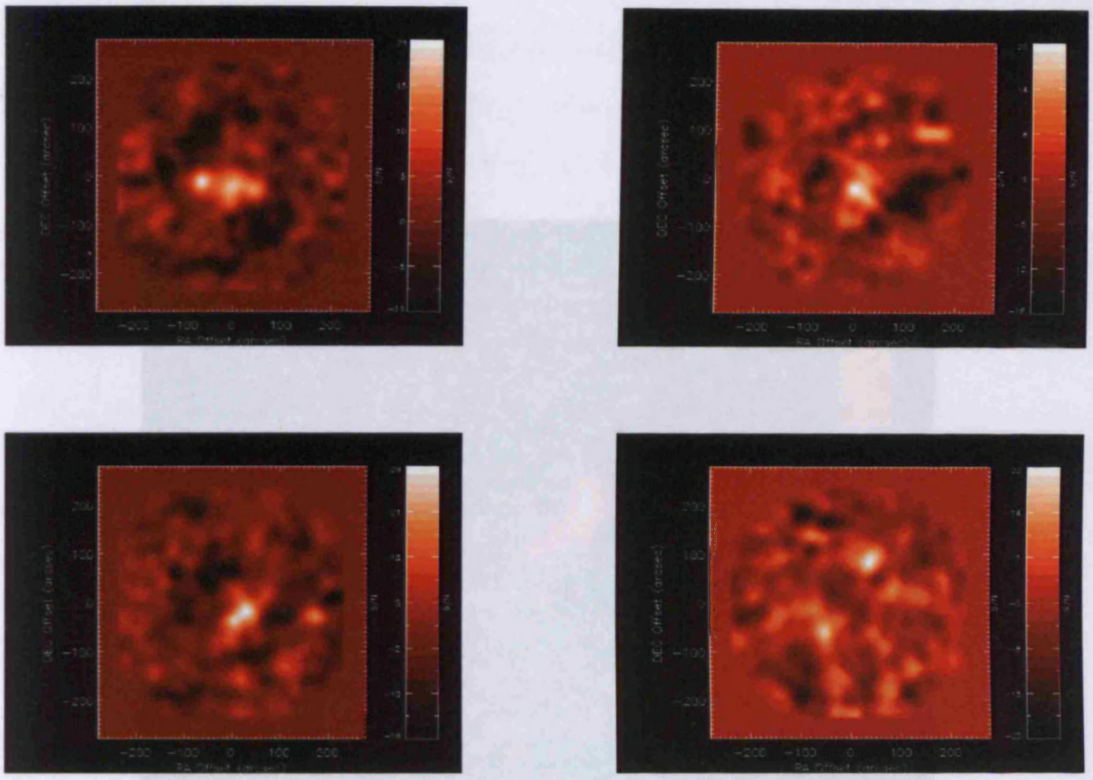

Figure 6.1: S/N maps of the clusters Abell 1835 (top left), Abell 2218 (top right), MS0451.6-0305 (bottom left) and Abell 851 (bottom right), convolved with the Bolocam beam to enhance the structure in the images. Emission from Abell 1835 is obvious (central source), as is that from the two point sources SMM J14009+0252 and SMM J140104+0252 on either side. Abell 2218 contains cluster emission as well as emission from two point sources close to the cluster. The field around MS0451.6-0305 is much more complicated, containing not only cluster emission, but emission from a number of point sources as well as a strong lensed arc. These individual components are hard to separate in the Bolocam maps, making MS0451.6-0305 a poor candidate for trying to extract the SZ signal. Finally, the field around Abell 851 shows no evidence for cluster emission, but instead contains a number of point sources.

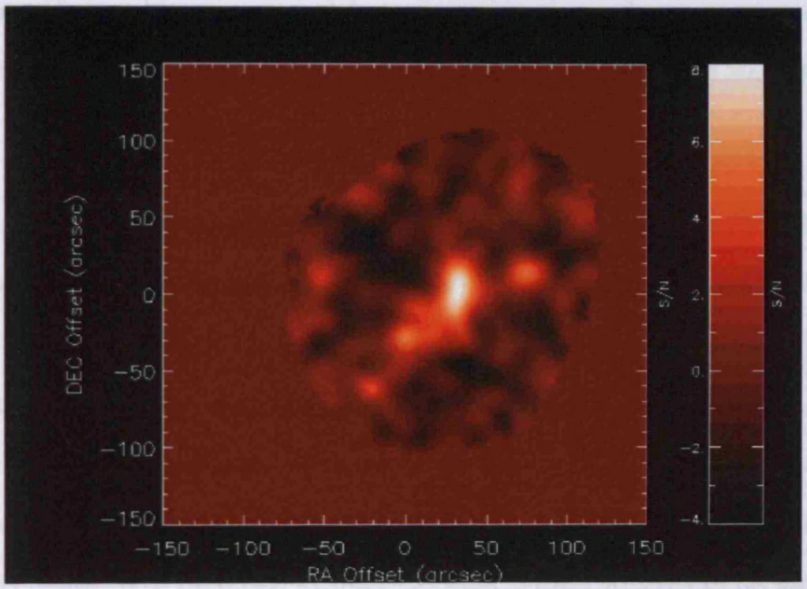

Figure 6.2: SCUBA image of the cluster MS0451.6-0305. A bright lensed arc, thought to be associated with a $z \sim 2.9$ Lyman Break galaxy, is just visible in the central region of the image. This feature is not, however, reliably resolved in the Bolocam map of the source. Data for map kindly provided by M. Zemcov.

MS0451.6-0305 is a well-studied cluster at a redshift of ~ 0.55. [173] detect a strong SZ decrement, which led to the expectation that a strong increment could be detected at higher frequencies. [31], however, report the presence of a large, bright lensed arc at sub-mm wavelengths, apparently associated with a high redshift Lyman Break galaxy. Whereas this arc can be detected in the central portion of SCUBA imagery of the cluster (Fig. 6.2), it is not unequivocally detected in the Bolocam map (see Fig. 6.1). This makes modelling of the cluster extremely difficult, and since the analysis presented here is highly dependent upon accurate modelling, this prevented MS0451.6-0305 being a suitable candidate for SZ analysis in this case.

Abell 2218 is an extensively studied cluster at moderate redshift ($z \sim 0.17$). The cluster is well-known for containing one of the highest redshift lensed sources recorded so far: SMM J16359+6612, believed to be located at $z \sim 7$ (see, e.g. [67]), and for the existence of a large discrepancy between estimates of the cluster mass made using X-ray and gravitational lensing (e.g. [34]). It is believed that the cluster may have experienced a merger sometime during its evolution [165]. Recent research into the cluster have included studies of other lensed sources in its vicinity (e.g. [117]) and studies of the cluster population [118, 170, 188]. The field contains a number of bright point sources, which are visible in the Bolocam maps. In principal, therefore, Abell 2218 was a potential candidate for SZ analysis.

The most promising source for SZ analysis was, however, Abell 1835. Abell 1835 is also a well-studied source over a large range of wavelengths. It was one of the brightest objects in the ROSAT source catalog and is located at $z \sim 0.25$. Early observations showed the cluster to contain a significant cooling core. The cluster field contains a number of lensed sources, and in 2004 an object was discovered that appeared to be a lensed source at a redshift of approximately 10 [155]. Follow-

up observations using data from the Keck and Spitzer telescopes did not, however, detect the source [198], and an independent analysis of the original data also did not lead to any detection. Recent research on Abell 1835 has tended to concentrate on the structure of the cluster. The field around Abell 1835 contains two bright point sources, SMM J14011+0252 and SMM J14009+0252, both of which are subjects of interest in their own right. SMM J14011+0252 is believed to be a lensed sub-mm galaxy at $z \sim 2.56$, whose properties are consistent with it being a massive spheroidal galaxy undergoing starburst [146], while SMM J14009+0252 is believed to be located at $z \sim 1.3$. Multi-frequency observations of both sources have been carried out to help characterise the spectral forms of sub-mm sources (see, e.g. [106]).

6.1 Abell 1835: SZ and Point Source Analysis

Once Abell 1835 had been chosen as the primary object for further analysis, a code was written to simulate the observations of the source and obtain estimates for the point source fluxes and SZ emission. The details of this code are described in the next section.

6.1.1 Modelling and Parameter Estimation

As with the map-making pipeline, the modelling and parameter estimation was organised into a set of individual routines which were called from an overall program ('top level'). The top level of the program produced a range of values for each of the parameters that defined the model. These parameters were stepped through individually and passed to a dedicated procedure (referred to here as

cluster_model_mod) to produce simulated observations. These simulations were then compared to the data map and the degree of matching between the two evaluated using a simple chi-squared statistic.

The parameter set that best fitted the data map was then passed to another module (referred to as Fisher_matrix_mod) to determine the errors on the values.

Although in essence a simple procedure, this process involved several iterations to refine the positional information and the values of the parameters. The basic structure of the cluster model generation code is outlined below.

6.1.2 Model Code

The module simulation code first generates an image that represents the area of sky over which the observations are taking place. Because the telescope chops by 90", the size of the simulated image had to be substantially larger than the final map. The array was also constructed on a finer angular resolution than that of the BOLOCAM beam ($\sim$ 30"), and later convolved with the telescope beam to reproduce this resolution. The resolution of the map was originally chosen to be 3", although this was later reduced further to 1" to include errors from the pointing in the results.

The next step was for the map to be filled with simulated signal from the cluster SZ emission. It is common to assume that the SZ signal follows the distribution of a King model [115], defined by:

$$D(\theta) = \left(1 + \frac{\theta^2}{\theta_c^2}\right)^{-\frac{3}{2}+\frac{\beta}{2}} \tag{6.1}$$

where θ is the angular displacement from the centre of the cluster, and the shape of the distribution is determined by two free parameters: θ_c and β (hereafter referred to as the 'profile parameters').

The change in the specific intensity of the CMB as a result of the SZ effect (equivalently: 'the SZ signal', $I_{SZ}(\theta)$) was then given by:

$$I_{SZ}(\theta) = y_0 I_0 g(x) D(\theta) \tag{6.2}$$

where I_0, and $g(x)$ were defined in Chapter 2: 'The Sunyaev Zel'dovich Effect - theory and observation', and y_0 is the value of the Compton parameter in the centre of the cluster.

The temperature of the electron gas in Abell 1835 is believed to be high enough that relativistic corrections to the thermal effect have to be accounted for. Although the general aim of the simulation code was only to extract the flux due to cluster emission, these corrections were, nevertheless, included in the simulation. These are generally expressed in terms of the variable θ_e:

$$\theta_e = \frac{k_B T_e}{m_e c^2} \tag{6.3}$$

Following [105], the form of g(x) in (6.2) is modified to become:

$$g(x) = g_0(x) + \frac{x^4 exp(x)}{(exp(x)-1)^2}\left(\theta_e Y_1 + {\theta_e}^2 Y_2 + {\theta_e}^3 Y_3 + {\theta_e}^4 Y_4\right) \tag{6.4}$$

where g_0 is the non-relativistic form of g(x) derived using the Kompaneets ap-

proximation and the values for Y_1, Y_2, Y_3 and Y_4 are corrections to this expression, defined previously (see 'Chapter 2: The Sunyaev Zel'dovich effect - theory and observation'). [1]

It is common to assume in SZ analysis that the electron gas in a cluster is isothermal. The value for T_e chosen for the analysis was based upon a range of literature sources. Measurements of the electron temperature are most commonly based on X-ray data. Since X-ray observations generally have a better resolution than sub-mm observations however, the models used to describe the temperature profile of a cluster can be more complicated.

In some cases this was not a problem. [109], for example, find that a two-component thermal plasma model comprising one component at 1.8 keV and another at 8 keV fits their temperature profile well. The 1.8 keV component would not produce a substantial relativistic correction to the SZ effect, and only the 8 keV model needed to be considered.

On the other hand, some independent groups use two-component models to fit the profiles which have very similar temperatures. In these cases, the temperatures of the components were averaged. Finally, if different results for the X-ray derived temperatures are reported for the centre of the cluster and for regions further out and depending on the characteristic size of the cluster core in these models, it was possible to consider only the results from the outer regions. Once again, this is due to the difference in resolution between the X-ray and sub-mm measurements: the 1.1 mm measurements would not be able to observe detailed variations in the centre of the cluster.

[1] The equation given here is different to that in [105] since their definition of the Compton parameter differs slightly from the one given here by a factor of θ_e. Once this has been accounted for, the expressions are equivalent.

Reference	T_e value (keV)	Notes
[112]	7.95 ± 0.61	Averaged value
[109]	$7.6^{+0.8}_{-0.6}$	Outer region of cluster
[109]	8.0	Two component model
[160]	8.2	
[177]	8.7 ± 0.6	
[131]	7.6 ± 0.4	
[6]	$9.8^{+2.3}_{-1.3}$	
[223]	$8.5^{+1.5}_{-0.5}$	Multiphase model
[223]	8.2 ± 0.5	Isothermal model
[142]	8.2 ± 0.5	

Table 6.1: Literature results for the electron gas temperature of Abell 1835.

A summary of the literature values for T_e used in this work is given in Table 6.1. The results that were reported with associated errors were then averaged to give a mean value of $T_e = 8.3^{+1.0}_{-0.6}$keV, which was subsequently adopted as the standard value of T_e for the subsequent analysis. [2]

In the next stage of the analysis code, Cluster_model_mod converts the intensity values to flux values and scales them to units of Jy by multiplying by a factor of $\Delta\Omega_{pixel}/10^{-26}$, where $\Delta\Omega_{pixel}$ represents the solid angle of the pixels in the map.

Once the signal from the SZ has been generated, the point sources were added. The central pixel in the map was defined to be at the same R.A. and decl. as the centre of the X-ray emission from Abell 1835, obtained from the literature. This was initally taken to be R.A.: 14 hrs 01 min 00.8 s; decl.: 2° 52′ 45.6" (from [160]). The R.A. and decl. values of the other pixels were calculated relative to this position and stored. The locations of the point sources had been stored and could then be compared to the R.A. and decl. maps. The pixels whose R.A. and decl. values matched those of the point sources the closest were then attributed single values of flux, F_0 and F_1, whose values were defined in the top level of the analysis

[2]Only those values with reported errors were included in the calculation.

routine.

Next, the map was convolved with a Gaussian kernel with FWHM 31.5" to reproduce the resolution of the data maps and passed through a proceedure which used the data from the observations to reproduce the telescope's chopping and nodding. For each position on the sky - as stored in the observation files - the equivalent location was found in the simulated map using the R.A. and decl. arrays. The signal in this pixel was compared to the signal from the regions of sky 90" in az from it. This section of the code was particularly cumbersome and was the longest part of cluster_model_mod to run.

The model map was then re-binned to the same pixel-size as the data maps and cropped to include only those regions of sky that were actually being studied. Once this was done, the model map was in an appropriate state for it to be compared to the data map.

The chi-squared statistic, χ^2, is defined as:

$$\chi^2 = \sum_i \frac{(S_{model,i} - S_{data,i})^2}{\sigma_{data,i}} \tag{6.5}$$

where $S_{model,i}$ and $S_{data,i}$ are the fluxes of the i'th pixel in the model and data maps, respectively, and $\sigma_{data,i}$ is the noise in the i'th pixel in the data map. $\sigma_{data,i}$ was calculated by taking the error from the data maps and weighting these values by a factor $1/\sqrt{cov_i}$, where cov_i is the coverage of the i'th pixel of the data map.

Values for the five parameters y_0, F_0, F_1, θ, β were then passed into cluster_model_mod from the top level of the program, and the corresponding χ^2 for each set of parameters stored.

Values of the profile parameters, θ_c and β, in SZ observations are generally chosen from X-ray measurements, since SZ measurements have traditionally not been of sufficient resolution to constrain them accurately. Literature values for the profile parameters can, however, vary by appreciable amounts. Furthermore, there is reason to suspect that the profile parameters used in X-ray observations may not be exactly representative of SZ profiles. The X-ray emissivity of cluster gas depends approximately upon the square root of the electron temperature and the square of the electron density [23]. A simple comparison of the equations describing the SZ and X-ray emission leads to the conclusion that, while the SZ emission depends upon the line of sight integral of $n_e T_e$; X-ray emission depends upon the equivalent integral of $n_e^2 T_e^{1/2}$. Unless there is a very specific correlation between the temperature and density profiles in a cluster, therefore, this implies that the SZ and X-ray distributions should be different.

Computer simulations of SZ and X-ray emission from galaxy clusters have also suggested that there may be significant discrepancy between X-ray and SZ cluster profiles. [86] find that using X-ray cluster profiles in SZ analysis could lead to errors in the measurement of y_0 on the level of 10%.

Unfortunately, however, SZ experiments generally do not have the resolution to confidently constrain cluster profiles, which is why X-ray profiles, in general, continue to be assumed. It was decided in this project to use a range of different sets of profile parameter values. One of the most recent observations of Abell 1835 reported in the literature were made by La Roque et al. [125], using the *Chandra* X-ray observatory and OVRO/BIMA interferometer. They report three sets of values for θ and β obtained using different combinations of their X-ray and SZ data:

i) Using a double-beta non-isothermal model, in which the the 3-D electron density profile, $n_e(\mathbf{r})$ is defined by:

$$n_e(\mathbf{r}) = n_{e_0}\left[f\left(1+\frac{\mathbf{r}^2}{r_{c1}^2}\right)^{-3\beta/2} + (1-f)\left(1+\frac{\mathbf{r}^2}{r_{c2}^2}\right)^{-3\beta/2}\right] \tag{6.6}$$

where the shape of the profile are fitted using the variables n_{e_0}, f, r_{c1} and r_{c2}. This form of distribution is designed to better fit cluster X-ray data, which often demonstrates strongly-peaked central emission.

ii) Using a single beta-model of the same form as (6.1), fit to a combination of a restricted set of the X-ray data, which excludes emission from the central 100 kpc of the cluster, and all of the SZ data. All of the SZ data was used for this fit since SZ emission is less sensitive to the electron density, so is not affected significantly by the presence of cool-cores in clusters (which cannot accurately be included in the simple beta model), whereas the X-ray data is more sensitive to high levels of cluster-core emission and so was restricted to exclude emission from the central $\sim$ 100 kpc region.

iii) Fitting only the SZ data, with the value of β fixed at 0.7. [125] find that their results for the measurements of y_0 and flux do not vary significantly between $\beta \sim 0.6$ and $\beta \sim 0.8$.

The double-beta isothermal model is, as mentioned above, specifically a distribution chosen to fit the X-ray data from cool-core galaxy clusters; SZ data is less sensitive to the detailed physical state of the gas in a galaxy cluster. The values for the double-beta isothermal model were, therefore, not used for this analysis. The values of θ_c and β based upon the other two models were, for the combined

fit to SZ and restricted X-ray data: $\theta_c = 33.6$", $\beta = 0.69$; and for the fit to the SZ-only data: $\theta_c = 50.1$", $\beta = 0.69$. It was decided to investigate the parameters that minimized χ^2 for various combinations of these values of θ and β, as well as to attempt a 'total fit' of all five parameters. This, therefore, constituted six distinct scenarios:

a) $\theta = 33.6$", $\beta = 0.69$; y_0, F_1 and F_2 allowed to vary; b) $\theta = 50.1$", $\beta = 0.69$; y_0, F_1 and F_2 allowed to vary; c) $\beta = 0.69$; y_0, F_1, F_2 and θ allowed to vary; d) $\theta = 33.6$"; y_0, F_1, F_2 and β allowed to vary; e) $\beta = 50.1$"; y_0, F_1, F_2 and β allowed to vary, and f) all parameters allowed to vary.

When the initial models were made, it was discovered that the pointing was still not entirely correct, and that small offsets still remained between the maps and the archive cluster position. These offsets were corrected for in two ways. First, a 'pixel-scale' shift was implemented into cluster_model_mod.pro. This shift was based upon forming a 'reasonable' model of the cluster, then matching it to the data by offsetting it by an integer number of pixels in both spatial dimensions and forming a χ^2 between the two maps. The value for this offset remained constant for different models (i.e. different values for the fluxes, Compton parameter and profile parameters) and so could be fixed within the routine.

A finer pointing correction was achieved by varying the position of the centre of the cluster in the model map on the arcsecond scale (i.e. in the over-resolved model map generated before the model was convolved and compared to the data map). The offsets obtained with these small corrections were mostly the same for different models, but there were exceptions, and the small offsets were, therefore, determined individually for each set of parameters once the best fit model had been obtained.

6.1.3 Identifying Minima in the χ^2 Distribution

The process for identifying and refining a minimum in the χ^2 value involved an iterative method similar in concept to the Newton-Raphson technique for identifying minima. The initial step involved choosing a 'mesh' of reasonably-spaced values for each parameter, then allowing the routine described above to calculate χ^2 values for every combination of parameters in this set.

The definition of 'reasonably-spaced' in this context was not precise. The aim was to find a global rather than local minimum in the χ^2 values. A mesh of values in which the parameters were close together risked missing a global minimum located outside the limits of this mesh, whereas if the values were too widely separated, there was the possibility that a minimum could be located below the 'resolution' of the search, and missed as a result.

Clearly, in order to improve the chances of getting an accurate minimum, as many values as possible had to be sampled for each parameter. The time to run the analysis program, T, was, however, slow and scaled according to:

$$T(\mathbf{p}_1, \mathbf{p}_2, ..., \mathbf{p}_N) = t_{run} n^N \tag{6.7}$$

where t_{run} is the time for an individual run of the analysis program, n is the number of values sampled for each parameter, N is the total number of parameters, and $\mathbf{p}_i$ represents the array of values for parameter p_i.

With up to five parameters being varied, n^N could become large. The analysis took approximately 135 s to compute the χ^2 value for a single model, meaning that it was difficult to sample a reasonable number of points as N increased. The run

N	n=3	n=4	n=5
N=3	1.01 hrs	3.04 hrs	9.11 hrs
N=4	4.69 hrs	23.44 hrs	4.88 days

Table 6.2: Running times for different models. n represents the number of parameters in the model, while N represents the number of values being sampled for each parameter.

times for 3, 4 and 5 parameter fits using N=3 and N=5 are shown in Table 6.2. The length of time it took to run the analysis was primarily because the code needed to chop the cluster model in the same way as the data was taken (as discussed above).

For the cases in which 3 or 4 values for each parameter were being sampled (N=3 or 4), smaller initial step sizes could be sampled. These steps were typically $\sim$ 0.4 - 0.5 mJy for F_1 and F_2, and $\sim$ 0.2 - 0.4$\times 10^{-4}$ for y_0. The step size for θ and β in the different runs were more variable, since the range of values being tested was also larger. The step size would often be modified between different runs of the analysis routine to reflect how quickly the χ^2 appeared to be converging (see below). The process was, therefore, a dynamic one.

Once the mesh of values for a given set of models had been searched, the χ^2 values were examined to identify a minimum. The process would then be repeated with a refined set of model parameters based upon the results of the previous run.

Initially, this process of refinement was achieved by reducing the limits of the search by 'zooming in' on the location of the minimum. Once an approximate location for a minimum was found, this method was in principal reasonably efficient at refining its position, since the step size could be halved during each search, reducing the parameter-space volume of the search quickly. In order for it to be useful, however, the location of the minimum had to be known with reasonable accuracy, and the size of the initial mesh had to be large enough that the minimum

would not end up being located on the edge of the parameter space being studied (or else the search would have to be repeated, without any reduction in the mesh spacing). In general, this required $N > 3$. As the location of the minimum became apparent, however, subsequent runs could be modified to use $N = 3$, reducing the processing time required to identify the minimum.

The efficiency of this method was not, however, guaranteed. A faster procedure was to assume that an individual slice through the chi-squared surface (following the variation in a single parameter) was smooth and approximately quadratic. The surface could then be fit, and the minimum value for the parameter along which the slice was being taken could be quickly located. This method could be repeated for all the parameters, and the analysis code run again (centred on the new cluster model) with a reduced step size for each of the parameters. The effectiveness of this method clearly relied on the assumption that the χ^2 surface could be approximated as a quadratic. As the step size around the minimum reduced, however, the quadratic assumption was expected to become increasingly accurate.

Initially, runs with $N > 3$ were still desirable in order to get a reasonably resolved curve to fit (for each parameter). Although this implies no improvement in efficiency in processing time, it was found that the method was useful for refining the position of the minimum even if it was located outside the parameter space explored in the initial search.

As the accuracy of the quadratic assumption improved, it became possible to examine the first derivatives of the χ^2 values instead of the χ^2 values themselves. Under the quadratic assumption the first derivative of the χ^2 curve for a single parameter is linear, which could, in general, be fit well, even for $N = 3$. This

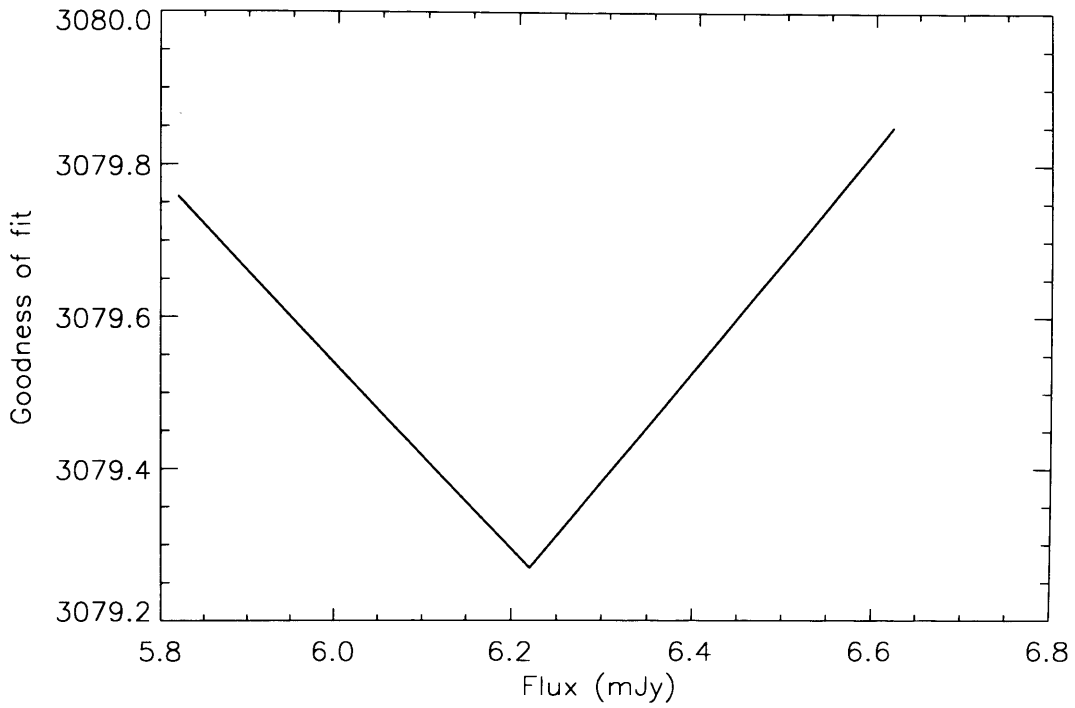

Figure 6.3: Set of χ^2 values for a three-parameter model ($\theta_c = 50.1$", $\beta = 0.69$). The values represent the goodness of fit obtained by varying the flux of one of the point sources in the field, while keeping the other model parameters (flux of the second point source and y_0) constant.

represented a substantial increase in the efficiency of the search.

The derivatives of the χ^2 values were obtained using a simple finite-difference scheme. For a representative set of χ^2 values (see, e.g. Fig. 6.3), the derivatives were calculated according to:

$$\mathbf{d} = (d1, d2, d3)$$

$$d1 = \Psi^2(1) - \Psi^2(0)$$

$$d2 = 0.5\left(\Psi^2(2) - \Psi^2(0)\right)$$

$$d3 = \Psi^2(2) - \Psi^2(1) \tag{6.8}$$

where $\mathbf{d}$ represents the array of values for the derivatives, and Ψ^2 the array of values for the χ^2.

A new estimate for the minimum value of the parameter being examined could then be calculated simply by using:

$$p_{new} = p_{old} + \Delta p \left(0.5 - \frac{\mathbf{d}(0)}{\mathbf{d}(2) - \mathbf{d}(0)} \right) \tag{6.9}$$

where p_{new} and p_{old} represent the old and new values of the parameter, and Δp is the step size being used for the analysis.

Where the linear trend was not exact, (6.9) was modified to:

$$p_{new} = p_{old} + \Delta p \left[0.5 - 0.5 \left(\frac{c}{m} \right) \right] \tag{6.10}$$

where c and m are found by solving the simultaneous equations:

$$\begin{aligned} 0 &= -2 \sum_i i\mathbf{d}(i) + 2c \sum_i i + 2m \sum_i i^2 \\ 0 &= -2 \sum_i \mathbf{d}(i) + 2m \sum_i i + \sum_i 2c \end{aligned} \tag{6.11}$$

These equations were derived by calculating the least-squared values of m and c that provided the best linear fit ($\mathbf{d}_{fit}(i)$) to the derivative values:

$$\mathbf{d}_{fit}(i) = m\ i + c \tag{6.12}$$

New values of m and c were then obtained by minimizing the difference, $\Delta = \mathbf{d} - \mathbf{d}_{fit}$:

$$\begin{aligned} \frac{\partial \Delta}{\partial m} &= 0 \\ \frac{\partial \Delta}{\partial c} &= 0 \end{aligned} \tag{6.13}$$

Despite this process being reasonably efficient, the parameter space remained large. The specific value of a parameter that minimized the χ^2 was deemed to have been found once its χ^2 derivatives met the conditions:

$$\begin{aligned} \frac{|d1|}{d1} &= -\frac{|d3|}{d3} \\ |d1| &= |d3| \\ d2 &= 0 \end{aligned} \tag{6.14}$$

where the values for $|d1|$ and $|d3|$ were ideally at least an order of magnitude

greater than $|d2|$.

The degree to which these conditions could be met, however, depended upon the time for processing and the validity of the underlying assumptions. At low values of θ or high values of β, for example, the χ^2 surface could become quite asymmetric. In this case, the step size had to be reduced in order to satisfy (6.14), but this required the minimum value for θ or β had to be known to a greater precision, which often meant that additional parameter-space searches had to be made. Inevitably, there was some level of compromise between the level of precision desired and the total time taken for an estimate of the parameters being investigated to be attained. In practice, the value for a given parameter was chosen once the conditions $\frac{|d1|}{d1} = -\frac{|d3|}{d3}$; $|d1| \sim |d3| \gg |d2|$, and $|d2| \sim 0$ were met.

6.1.4 Error Fitting

Once the set of parameters that produced the minimum χ^2 had been determined, it was possible to calculate the errors on their values by determining the associated Fisher matrix.

The Fisher matrix is useful for estimating errors in a model that contains several parameters. In general, the minimum variance, $V_{min}[a]$ of a statistical population, P, that varies in some dimension, x, the values of which are dependent upon a single parameter, a, can be determined using the Fisher (or Crámer-Rao) inequality:

$$V[a] = \left(1 + \frac{\partial b}{\partial a}\right)^2 / E\left(-\frac{\partial^2 \ln P}{\partial a^2}\right) \tag{6.15}$$

where b is the bias in the estimate of a [181]. The derivation of the Fisher inequality can be extended to the case where P depends on a number of parameters, $\mathbf{a} = a_0, a_1 \ldots a_m$. The variance is replaced by a covariance matrix, $V_{i,j}$, which is given by:

$$V_{i,j} = E\left(-\frac{\partial^2 lnP}{\partial a_i \partial a_j}\right)^{-1} = F_{i,j}^{-1} \tag{6.16}$$

where $F_{i,j}$ is referred to as the Fisher matrix.

In the ideal case, the errors in the values of the parameters $\mathbf{a}$ are given by the square root of the leading diagonal elements of $V_{i,j}$:

$$\delta a_i = \sqrt{V_{i,j}} \tag{6.17}$$

Assuming the errors on the parameter estimates to be Gaussian distributed, the Fisher Matrix is given by:

$$F_{ij} = \frac{1}{2}\left(\frac{\partial^2 \chi^2}{\partial p_i \partial p_j}\right)_{\mathbf{p_{min}}} \tag{6.18}$$

where the derivatives are evaluated for the set of parameters, $\mathbf{p_{min}}$, that minimize the χ^2. The covariance matrix of this set of parameters is then the inverse of the Fisher Matrix, and the standard errors on each parameter are simply found by taking the square root of the elements along the lead diagonal of this matrix, i.e.:

$$\sigma_i = \sqrt{F_{ii}^{-1}} \tag{6.19}$$

The matrix of second derivatives of χ^2 in 6.18 were evaluated again using a finite-element technique, written again in an IDL module. For a given set of parameter values, centred on some $\mathbf{p_{min}}$, the first derivatives with respect to p_1 were calculated at every point in the array of χ^2 values in the same way as described in (6.8). The second derivatives were then calculated by subtracting values for the first derivative with respect to parameter p_i in the direction of p_j and stored.

As discussed above, it had already been found that, once rough minimum values for the free parameters were determined, it was necessary to make even smaller pointing corrections in order to obtain the most accurate values. These were obtained by comparing values of χ^2 obtained by shifting the model map by 1" steps before convolving.

These shifts were also important in order to incorporate the errors in the pointing into the calculation of the errors of the fitted parameters. This was done by assimilating the pointing into the calculation of the Fisher Matrix. i.e. when calculating the grid of χ^2 values from which the Fisher Matrix was formed, values of the pointing offsets were also varied on arcsec scales and the procedure outlined above repeated.

Clearly, with five variables now being altered, the processing time increased once again, but in general the positional offsets were varied for a given set of parameters (usually the parameter set that had produced the original minimum in the χ^2), then their values were fixed and the other parameters allowed to vary once more. This speeded up the time for processing. The positional offsets also

appeared to be reasonably robust to variation in the other parameters, justifying this split in the fitting procedure. Once this iterative process produced a reasonable set of χ^2 parameters (see below), a single grid was formed with all five variables being varied, from which the Fisher Matrix could be calculated.

In this chapter, we have discussed the modelling of the cluster maps, and the methods chosen to obtain estimates for the parameters of these models that best fit the observation. In the next chapter we will discuss the results of this analysis, and further sources of error in the values of y_0 and flux obtained.

Chapter 7

Parameter fit results and errors

The results of the parameter estimation for Abell 1835 are given in Table 7.1. The set of parameters with the best value for the goodness of fit (minimum value of χ^2) were those obtained by fixing $\theta_c = 50.1$". The best fit values of the central Compton parameter and point source fluxes in this model were found to be: $y_0 = (4.19 \pm 0.48) \times 10^{-4}$; 7.17±1.84 mJy (SMM J140104+0252), and 12.18±1.77 mJy (SMM J14009+0252). These values were reasonable, and consistent with other published measurements.

The value of β obtained in this fit (1.6 ± 0.2) was, however, significantly different to typical published results. The next stage of the analysis was to involve combining the results obtained here with other published measurements of y_0 for Abell 1835 in order to produce a plot of the spectral form of the SZ signal from the cluster. A comparison of these results clearly required that the profile parameters for the experiments to be the same, since best fit estimates of the fluxes and y_0 will depend upon their values. If the physical model parameters were different, therefore, the comparison would not be 'like-for-like'. The process of converting

β_{model}	0.69	0.69	0.69	–	–
$(\theta_c)_{model}$ (″)	33.6	50.1	–	33.6	50.1
$\mathcal{F}_1$ (mJy)	6.48±2.00	6.22±2.08	7.16±1.88	7.09±1.89	7.17±1.84
$\mathcal{F}_2$ (mJy)	11.32±1.92	10.90±1.98	11.98±1.79	12.38±1.82	12.18±1.77
$y_0 \times 10^{-4}$	(4.68±0.48)	(4.43±0.49)	(6.52±0.64)	(4.85±0.47)	(4.19±0.40)
β	0.69	0.69	0.69	1.20 ± 0.2	1.60 ± 0.2
θ_c (″)	33.6	50.1	$14.7^{+2.4}_{-2.2}$	33.6	50.1
R.A. offset (″)	1.8	1.9	2.1	2.1	2.0
Decl. offset (″)	3.6	3.9	2.6	2.8	2.5
χ^2	3066	3079	3058	3056	3054

Table 7.1: Parameter estimates (1 mm Bolocam observations) and χ^2 values. $\mathcal{F}_1$ and $\mathcal{F}_2$ represent the fluxes for SMM J140104+0252 and SMM J14009+0252, respectively. Number of degrees of freedom = 3013.

results from one set of profile parameters to their equivalent values for another set of parameters is discussed further in Chapter 8: 'Multifrequency data: SZ fits and point source analysis'. It was decided, however, that the conversion would be most reliable if the profile parameters for the data points in the fit were as similar as possible. In practice, this meant choosing either the $\beta = 0.69$, $\theta_c = 33.6$" results or the $\beta = 0.69$, $\theta_c = 50.1$" results. Of these, the fit with the lowest χ^2 value was the combination $\beta = 0.69$, $\theta_c = 33.6$". It was decided, therefore, that this set of results - $y_0 = (4.68 \pm 0.48) \times 10^{-4}$, $\mathcal{F}_1 = 6.48 \pm 2.00$ mJy and $\mathcal{F}_2 = 11.32 \pm 1.92$ mJy - would be used for the spectral fitting.

7.1 Efficacy of fit.

While the χ^2 parameter provided a quantifiable measure of how reliable a fit is to the data it represents, further checks were prudent. In particular, it is important for estimating the values of flux and the associated errors that the signal from different pixels be independent. Since the scan strategy employs chopping, and the only cleaning of the data is performed with an average subtraction, however,

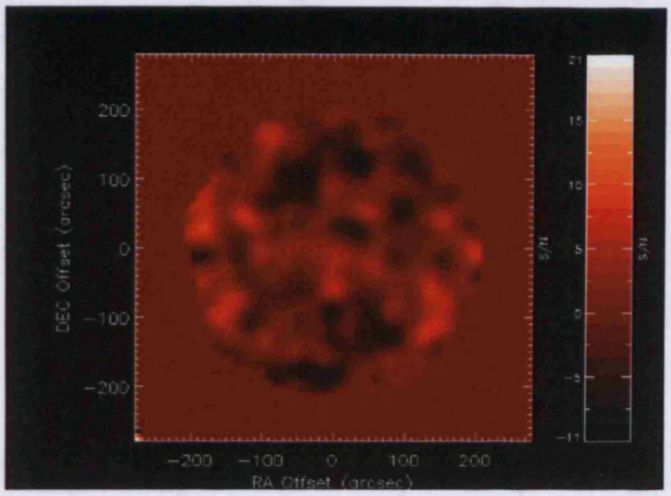

Figure 7.1: Map of residuals, formed by taking the difference between the convolved model and data S/N maps. If the model were a poor representation of the data, one would expect to see residual signal from the cluster location or the point sources. Instead, even after convolving, the science sources appear to have been accounted for well, and there is no evidence for additional sources in the field.

it was expected that the signal covariance between pixels should be low, relative to other scan strategies and cleaning methods.

Nevertheless, checks were made to ensure this was a reasonable assumption. One simple check was to subtract the simulated cluster S/N map, based upon the fitted model, from the data S/N map. The resulting S/N 'difference map' was then convolved once more with the telescope beam to exaggerate any correlated structure/ sources in it. The resulting map is given in Fig. 7.1. A rough examination of Fig. 7.1 suggested that there was no discernible residual signal from the point sources or cluster, implying that the fit was good. Furthermore, there did not appear to be any other strong point source candidates in the field that had not been included in the fit. There is a point source-like object located just below the centre of the map, but a search for sources in point source catalogues produce no

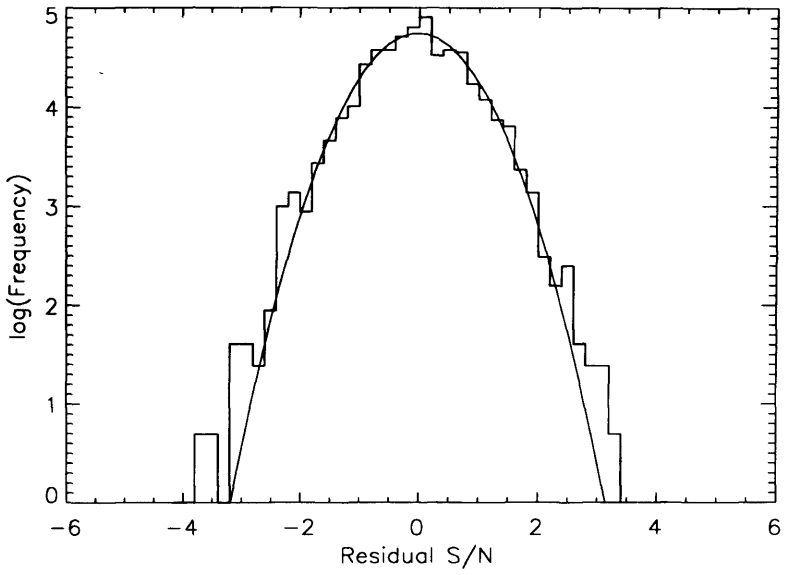

Figure 7.2: Signal to noise histogram of the residual map obtained by subtracting the best fit model from the data, plotted on logarithmic scales. The Gaussian best fit to the histogram (the solid line in the log plot) has $\sigma = 1.01$

matches, and it was concluded that the object was most likely to be an artifact of the noise, rather than a real source.

A more rigorous version of this testing is to examine the histogram of flux values for the (unconvolved) S/N difference map. The values were binned in 0.2 S/N intervals, centred on 0.0. The distribution of residual S/N was found to be approximately gaussian with a FWHM of 1.01, consistent with the residual signal in the maps being dominated by noise. An additional check was to plot the histogram on logarithmic axes and examine how accurate the fit was in the wings of the S/N distribution. Any excess of high S/N features would be obvious as a discrepancy between the fit and the data. The log-residual plot is given in Fig. 7.2, and demonstrates that the fit is reasonable, even at the high (or low) S/N ends of the histogram. It was concluded, therefore, that there were unlikely to be other point sources in the field.

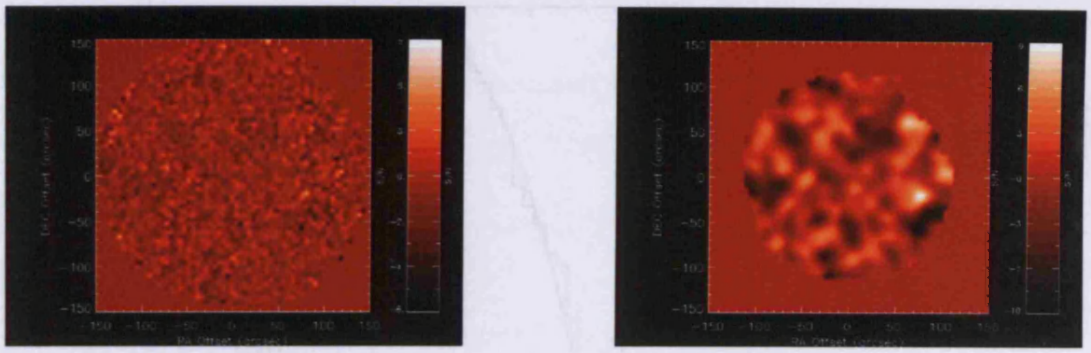

Figure 7.3: Jacknife maps for Abell 1835 data. The maps show no obvious structure, even when convolved with the telescope beam, and appear consistent with containing only noise.

A final test of the efficacy of the fit was to form a jacknife map of the data. Jacknife maps were produced by randomly changing the sign of half the data in the individual science maps, then stacking the maps in the same way as for the original science maps. The result of this, if there is no correlated signal in the map, should be noise with a mean value of 0.0. The jacknife map for the Abell 1835 data is given in Fig. 7.3, and a histogram of the jacknife flux in Fig. 7.4. It is clear that the map does not contain any correlated signal, confirming that the signal from individual pixels in the data map are uncorrelated to a good degree of accuracy.

7.2 Treatment of errors.

The errors in y_0, $\mathcal{F}_1$ and $\mathcal{F}_2$ quoted in Table 7.1 are those derived using the Fisher matrix method, outlined in Chapter 6: 'SZ Fitting: Analysis Code'. They include, therefore, errors in the pointing as well as errors due to variation in the other model parameters. Errors in the values of β and θ_c were, however, calculated differently,

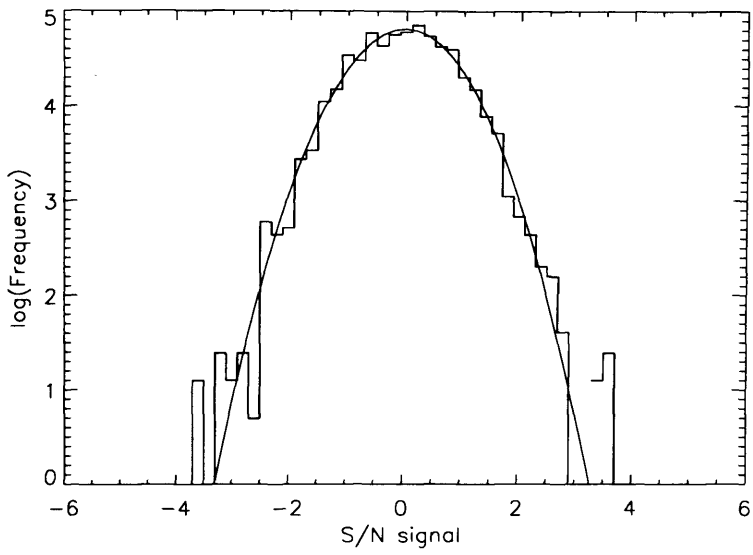

Figure 7.4: logarithmic histogram of the jacknife data, which was found to be fit well with a gaussian of mean -0.02 and standard deviation 1.06 (the solid line in the plot), supporting the conclusion that the model is an accurate representation of the Bolocam data.

by examining likelihood plots.

The likelihood plots were based upon the grids of χ^2 values obtained during the fitting. The normalised likelihood, $\mathcal{L}$ is given by:

$$\mathcal{L} = \exp\left(-\frac{1}{2}\delta\chi^2\right) \tag{7.1}$$

where the $\delta\chi^2$ is simply the difference between the χ^2 values in the grid and the minimum value of the χ^2: $\delta\chi^2 = \chi^2 - \chi^2_{min}$. The likelihood for a specific set of parameters represents the probability that those values are the *real* parameter values, given the set of observations. The locus of points at which the value of the likelihood drops to 68%, therefore, defines the the 1-σ set, and the maximum displacement of this set in a specific parameter 'direction' defines the error in that

parameter.

The error in the value of the central Compton parameter had to be modified to include other systematic effects that were present in the observations. The principal effects included:

- Calibration errors
- Kinematic effect
- Uncertainties in the physical model for the galaxy cluster
- Contamination from the CMB
- Confusion due to unresolved galaxy foregrounds
- Dust emission from individual galazies in Abell 1835

Some of these effects were relatively easy to quantize, while others required more work. The evaluation of each of these effects is described below.

7.2.1 Calibration errors

The calibration of the data was discussed in Chapter 5: 'Pipeline Development II: Pointing and Calibration'. Fig. 5.9 demonstrates that the pointing and calibration sources observed during the Jan 2006 run correlate reasonably well with the May 2004 calibration curve, but that there is also a reasonable level of scatter in the results. An estimate of the error due to calibration, Λ_c, was obtained, therefore, by calculating the noise-weighted dispersion of the sources about the May 2004 curve:

$$\Lambda_c^2 = \frac{\sum_i \frac{1}{\sigma_i^2} F_i^2}{\sum_i \frac{1}{\sigma_i^2}} \tag{7.2}$$

where the summation is over all datapoints in the calibration curve. F_i is the magnitude of the difference between data point i and the calibration curve, expressed as a fraction of the calibration curve value:

$$F_i = |d_i - C_i| \tag{7.3}$$

(with d_i and C_i the ith data point and corresponding value for the May 2004 curve, respectively), and σ_i is the error on the ith data point.)

This gave an error of 10.6% in the flux measurements due to the calibration uncertainty. This had to be added to the error in the May 2004 curve, which was due mainly to uncertainties in the model used to generate Mars' flux in the standard Bolocam pipeline. This error was estimated at 5% [77]. When combined, therefore, the overall error due to calibration uncertainty was found to be 11.7%.

7.2.2 Kinematic effect

The kinematic SZ effect was discussed in detail in Chapter 2: 'The Sunyaev Zel'dovich effect - theory and observation', and is due to the bulk motion of a cluster. The general form of the kinematic SZ can be expressed as:

$$I_{kin}(x) = -\left(\frac{mc^2}{k_B T_e}\right) y_0 \left(\frac{v_p}{c}\right) \left[\frac{x^4 e^x}{(e^x - 1)^2}\right] \tag{7.4}$$

Apart from at frequencies close to the null of the SZ spectrum, $\nu \sim 217$GHz, the kinematic effect is an order of magnitude smaller than the thermal effect. It is expected, based upon simulations of large-scale structure in a ΛCDM cosmology, that galaxy clusters should have an rms peculiar velocity of around 300 km/s. This leads to a kinematic effect that is of order 1 - 10% the thermal emission. [137] obtain a somewhat higher estimate of the velocity of Abell 1835 of ~500 km/s. Using this as a worse-case scenario, the kinematic emission for a cluster moving with this velocity at 273 GHz results in emission that is approximately 9% of the thermal effect.

7.2.3 Physical model uncertainties

The King model used in the modelling of the cluster assumes that the cluster has a spherically-symmetric density distribution and is isothermal. These assumptions are based on the idea that the cluster is dynamically relaxed and exists in a state of hydrostatic equilibrium. In reality, of course, neither of these assumptions are guaranteed to be correct, and it is possible that errors in the measurements of the Compton parameter could arise as a result. At the resolution of millimetre and sub-mm observations, however, the resolution is low enough that the spherically-symmetric approximation is reasonable. A similar conclusion can be drawn over the isothermal assumption.

At X-ray wavelengths the emission is more sensitive to variations in the density of gas than the SZ effect. This becomes more acute in the centre of clusters,

where more detailed physical processes are expected to be taking place in the gas. 'Clumping' of gas, for example, can be an important source of error in such observations. In general, however, because the form of the SZ effect has a relatively weak dependence upon the density distribution of the electrons in the cluster, it is not affected significantly by the detailed physics in the centre of the clusters. Similarly, although (as mentioned in Chapter 1: 'Introduction') sub-structure in the hot intra-cluster gas is observed in X-rays, this is unlikely to affect SZ measurements substantially. In particular it has been found that the pressure inside cavities is not significantly different to that outside them [29]. Since the SZ effect is also effectively a measure of the integrated pressure through the cluster gas the presence of cavities is unlikely, therefore, to affect the SZ signal. The low resolution of millimetre and sub-mm observations, once more, also reduces the impact of clumping and other forms of sub-structure on estimates of y_0. Nevertheless, there is likely to be some level of uncertainty in the measured cluster emission as a result of uncertainty in the physical model. The uncertainty in the value of y_0 due to clumping and departures of the cluster gas from the spherically-symmetric isothermal model were estimated at $\sim 2\%$.

The values of β and θ_c reported by [125] have associated measurement errors of ± 0.01 and ± 1.0", respectively. As with the error in T_e, these errors were incorporated into the analysis code, the other parameters fixed, and the minimisation repeated to calculate new values of y_0, which were then compared to the value determined in the original fit. The effect was, however, found to be small - on the level of 0.6%. As has already been noted (see Chapter 6: 'SZ Fitting: Analysis Code'), values of the King model parameters vary considerably in the literature. If these values are treated more generally as an additional error on β and θ_c, the effect of the uncertainty in the King model parameters on the value of y_0 is, clearly, likely

to be significantly larger. If information on the whole range of values reported in the literature had been included in the analysis, however, the values of β and θ_c themselves should have been representative of this distribution. As has already been outlined, this was not the approach chosen for the analysis and, as a result, it was not appropriate to include this kind of further information in the estimate of error in y_0.

Finally, uncertainty in the value of the electron temperature, T_e, was also expected to have an effect upon the observations. The relativistic corrections to the thermal SZ described in Chapter 6: 'SZ fitting: Analysis Code' depend on the value of the variable:

$$\theta_e = k_b T_e / mc^2 \tag{7.5}$$

which, in turn, depends on T_e. The value of T_e used in the analysis was $8.3^{+1.0}_{-0.6}$ keV. The value of T_e was, therefore, changed in the analysis code to 7.7 keV and 9.3 keV, the values of the other model parameters fixed, and the minimised performed to determine new best fit values of y_0. These new values could be compared to the best fit value already obtained. By this method, the error in y_0 due to uncertainty in the value of T_e was estimated as $\pm 2.5\%$ [1] .

7.2.4 Sources of confusion

There are a number of sources of confusion which could affect measurements of the SZ. At frequencies higher than the null however, the most important contributions

[1] The asymmetry in the error in T_e is removed in the corresponding error in y_0 because of the precision chosen for the estimate.

are expected to come from foreground galaxies and the CMB. Estimates of the flux from foreground galaxies give the rms signal to be about 0.3 mJy/beam [28]. For our analysis, we chose to assume a slightly higher signal of 0.5 mJy. A flux of 0.5 mJy in the real sky was found to correspond to 0.3 mJy once the chopping had been accounted for. By introducing this into the observations once more, the effect of this emission on the value of y_0 was thereby estimated to be $\sim 5.4\%$.

Determining the contribution from the CMB was more complicated. The power of the CMB at temperature, T, received by area, A, through solid angle, Ω, is given by:

$$P_{CMB} = \int \frac{2h\nu^3/c^2}{e^{h\nu/kT} - 1} A\Omega d\nu \tag{7.6}$$

where the integral is over frequency, ν. Differentiating 7.6 with respect to T gives:

$$\frac{dP_{CMB}}{dT} = \int -\left(\frac{h\nu}{kT^2}\right)\left(\frac{e^{h\nu/kT}}{e^{h\nu/kT} - 1}\right)\left(\frac{2h\nu^3/c^2}{e^{h\nu/kT} - 1}\right) A\Omega d\nu \tag{7.7}$$

The units of this equation are, clearly, (W/K). Since the CMB flux is generally characterised in terms of temperature, we need to obtain the factor which converts units of (K) into units of flux, (Jy). Units of (Jy) are equivalent to (W/m^2Hz), and we can, therefore, obtain the conversion by differentiating (7.7) with respect to ν, dividing by the area, A, and the factor 10^{-26}, which scales between (W) and (Jy). When this is done, we obtain:

$$Q = \frac{2x^2 k\nu^2}{(e^x - 1)^2 c^2} e^x \frac{\Omega}{10^{-26}} \tag{7.8}$$

where the dimensionless variable $x = \frac{h\nu}{kT}$ has been introduced to simplify the expression. Q, therefore, gives the conversion factor between (Jy) and (K).

This conversion could then be used to determine the approximate flux of the CMB and determine its effect upon estimates of y_0. The CMB signal is, of course, almost entirely constant across the sky, and will be mostly removed by the subtraction of signal from the extremes of the chop. It was only, therefore, the anisotropies that need to be considered as sources of confusion. The CMB anisotropies represent temperature variations of order μK. Evaluating (7.8) for the frequency of the Bolocam observations, we find $Q \sim 10.5$. Assuming temperature fluctuations of order 5 μK, the flux from the CMB was, therefore, found to be only $\sim 50\mu$Jy. This translates to an error in y_0 of $\sim 1.5\%$.

7.2.5 Dust emission

The final contribution to the systematic uncertainty in our determination of y_0 was emission from dusty sources in Abell 1835, and in particular from the cD galaxy in the cluster. Large clusters often contain a number of massive, dusty galaxies whose thermal emission can be significant. Measurements of the Balmer emission line ratio from Abell 1835's cD galaxy implies a significant amount of reddening, consistent with emission from warm dust [5]. Observations of prominent optical emission lines and a significant ultraviolet continuum also suggest that large amounts of star formation must be taking place in the galaxy, which supports the hypothesis that large reservoirs of dust exist there [5, 50].

In previous work [232] the contribution from dust emission from the cD galaxy was expected to dominate the SZ emission at 850μm. The SED from Abell 1835 including the 850μm signal is also, however, consistent with the SZ effect (e.g. [137]). In any case, accurate measurements of the SZ spectral distribution need to include the possibility of cD dust emission. The spectrum of galactic dust emission is expected to follow that of a greybody, $G(\nu)$:

$$G(\nu) = \epsilon(\nu)B(\nu) \tag{7.9}$$

where B is the idealised blackbody, ϵ is the emissivity of the dust, and ν is the frequency of the observations. ϵ is often assumed to the form of a power law, defined by index, α:

$$\epsilon(\nu) \propto \nu^{\alpha} \tag{7.10}$$

with values for α in the range 1.5 - 2.0.

Typical dust temperatures for dusty galaxies are expected to be in the approximate range 20 - 40 K (e.g. [157]). When this contribution is added to that from the SZ emission, the overall spectrum is expected to continue to rise after the SZ peak, leading to strong emission by 450μm. Observations at this wavelength may, therefore, be one way of identifying and estimating the dust emission at 1.1 mm.

Literature results for observations of Abell 1835 at 450μm do not, however, provide a consistent picture. [66,106] (who use the same set of data in their analysis) report strong emission at 450μm of around 20 ± 5mJy, consistent with significant

dust emission; whereas the 450 μm measurements from [232] was -2±13 mJy, consistent with no emission from the cluster at this wavelength. Both sets of data were obtained using the Submillimeter Common-User Bolometer Array (SCUBA) on the James-Clerk Maxwell Telescope (JCMT) on Mauna Kea, Hawaii. The 450 μm channel on SCUBA is not, however, considered as reliable as the 850 μm channel. At this wavelength, the results of [106] and [232] are more consistent, reporting emission 4.0 ± 1.2mJy and 4.5mJy (no error quoted), respectively.

Even at 850μm, however, the greybody dust spectrum has begun to contribute significantly, and one would expect the emission to be higher than would be predicted from the SZ alone. This effect would manifest itself either as a higher value for the central Compton parameter when modelling the 850μm results and minimising over y_0, or excess emission in the centre of the cluster when a 'standard' model is removed from the data. An 850μm map taken using SCUBA was kindly supplied by Mike Zemcov (Fig. 7.5).

Initially, the fit value of y_0 for the SCUBA map was examined. The fluxes of the point sources were fixed to the values reported in [232]; the King model parameters set to $\beta = 0.69$, $\theta_c = 33.6$", and the minimisation performed over just the y_0 value. This analysis, however, proved inconclusive, since the y_0 value was not found to be converging during the fit. After subtracting an approximate model, with a central Compton value of $y_0 \sim 4.0 \times 10^{-4}$ from the SCUBA map, however, it became clear that further processing had taken place on the SCUBA image (see Fig. 7.6), which we were not aware of. The nature of this processing could not be confirmed by the group that originally published the data. Unfortunately, therefore, further analysis of the SCUBA maps could not be carried out, and an alternative method of investigating the dust contribution from Abell 1835 had to be found.

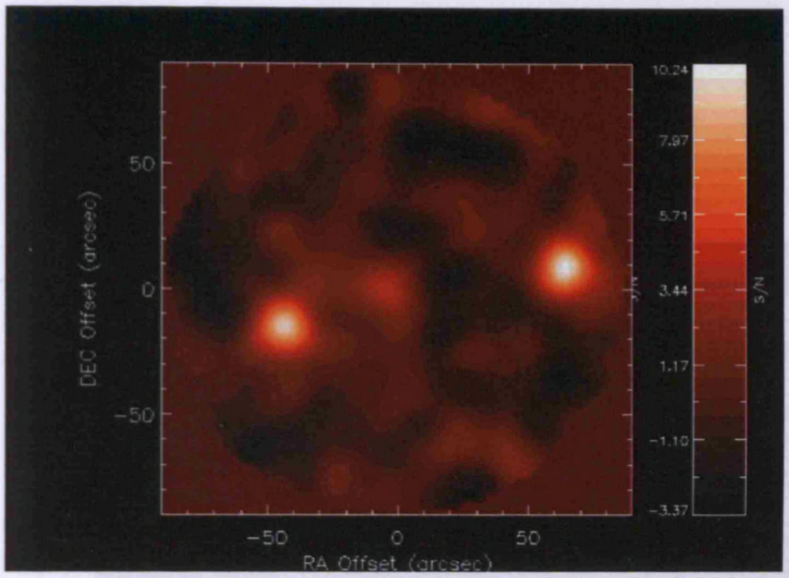

Figure 7.5: SCUBA 850μm map of Abell 1835. There is obvious emission from the cluster, which may be from dust or from SZ (or from both). The point sources are also clearly detected.

	Best fit model ($\beta = 1.6$, $\theta_c = 50.1$")	$\beta = 0.69$, $\theta_c = 33.6$"	$\beta = 0.69$, $\theta_c = 33.6$" (p)
y_0	$(4.19 \pm 0.40) \times 10^{-4}$	$(4.68 \pm 0.48) \times 10^{-4}$	$(4.34 \pm 0.52) \times 10^{-4}$)
χ^2	3054	3066	3062

Table 7.2: y_0 estimates based on different fit models. (p) denotes that the model included a 1.8 mJy point source at the cluster centre. Number of degrees of freedom = 3013.

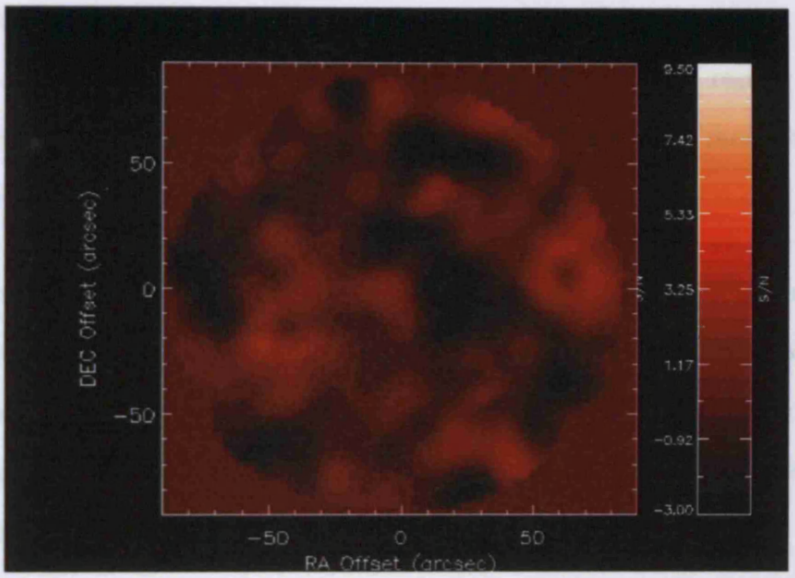

Figure 7.6: Difference map between a standard model for the map emission and the SCUBA data. There appears to be significant residual emission around both the point sources, despite the SCUBA beam having been modelled accurately. There appears, therefore, to have been additional processing on the map the nature of which was not clear, which prevented further analysis of the data.

An alternative approach to determining the effect of dust on the calculation of y_0 was to estimate the emission from the cD galaxy directly and incorporate it into the model itself. In this case, the results of [106] are ssumed to be correct (rather than the results given in [232], which are consistent with no emission). Assuming a greybody spectrum of the form given in (7.9) and (7.10), with a dust temperature of ~ 30 K, the expected flux from the cD galaxy at 1.1 mm was found to be $\sim 1.8 \pm 0.5$ mJy. Introducing a point source into the cluster model at the X-ray centre, therefore, and repeating the analysis, the best fit value for y_0 was found to be $(4.34 \pm 0.52) \times 10^{-4}$, with a χ^2 value of ~ 3062. These results are compared to those using the principal sets of results obtained using the model that did not include the point source in Table 7.2.

It is clear from this table that there is a small improvement in the χ^2 value as a result of introducing the point source in the cluster centre, but that it remains substantially higher than the best fit 4-parameter model fit. In keeping with the previous reasoning, however, the model with the most 'regular' King parameters and the best χ^2 value was chosen to proceed to the next stage of analysis, i.e. the model that included the point source, with $y_0 = (4.34 \pm 0.52) \times 10^{-4}$.

7.3 Total error

The total error budget for the observations, therefore, is given in Table 7.3. The additional systematic errors amounted to $\sim$ 16% of the value of y_0, while errors due to the modelling represented $\sim$ 12% of the value of y_0. For the model which incorporated a dusty point source in the centre of the cluster - simulating the emission from the central cD galaxy - the best fit value of y_0 was found to be

Systematic errors	Error (as % of result)
Calibration	11.7
Kinematic effect	9.0
CMB confusion	1.0
Galaxy foregrounds	5.4
Effective temperature	$^{+1.5}_{-2.6}$
Uncertainties in King model parameters	0.6
Others (clumping, etc)	2
Total errors	**Error (mJy)**
Pointing and model error (incl. point source)	0.52 mJy
Total systematic	0.69 mJy
Total error	0.87 mJy

Table 7.3: Error budget for Abell 1835 observations

$(4.34 \pm 0.52 \pm 0.69) \times 10^{-4}$. This then became the value of y_0 used for the next stage of analysis.

The calibration error and confusion from the kinematic SZ represent the largest individual components of the systematic errors outlined in Table 7.3, but it is clear that the emission from dusty galaxies in clusters remain an important source of error. Although it appears to be possible to incorporate such emission into the analysis through modelling, it seems likely that multi-wavelength observations of sources would be a clearer means of verifying the dust emission.

In this chapter, we have described the calculation of the systematic errors associated with the measurement of y_0 and described the process of deciding which value of y_0 to use for the next stage of analysis. This value was obtained for a model that included an estimate of dust emission from the central cD galaxy in Abell 1835. In the next chapter, we will describe the process of spectral fitting that led to the main conclusions of the research regarding SZ emission from Abell 1835 and an estimate of the cluster's peculiar velocity.

Chapter 8

Multifrequency Data: SZ Fits and Point Source Analysis

8.1 SZ spectrum

The final stage of the SZ analysis for Abell 1835 was to collate our result with measurements at other frequencies in order to form a spectrum, which could then be fit to obtain new estimates of y_0 and the peculiar velocity of the cluster, v_p.

Measurements of the SZ signal from Abell 1835 have been made by a number of different groups (see Table 8.1). In order to form a spectrum, the different measurements had to be converted into intensities. In the Rayleigh-Jeans limit, the temperature difference observed by an instrument can be related to the source intensity by:

Ref.	ν (GHz)	Param.	ΔT_{SZ} (mK)	y_0	v_p
[137]	142, 279	$\theta_c = 12.0 \pm 3.6$"	–	$4.9 \pm 0.6 \times 10^{-4}$	
		$\beta = 0.54 \pm 0.04$			
[137]	221	$\theta_c = 12.0 \pm 3.6$"	–	–	500 ± 1500
		$\beta = 0.54 \pm 0.04$			
[172]	30	$\theta_c = 12.2^{+0.6"}_{-0.5}$	$-2.502^{+0.150}_{-0.175}$	–	
		$\beta = 0.595^{0.007}_{-0.005}$			
[20]	145	$\theta_c = 12.2^{+0.6"}_{-0.5}$	–	$7.66^{+1.64}_{-1.66} \times 10^{-4}$	–
		$\beta = 0.595^{0.007}_{-0.005}$			
[19]	145	$\theta_c = 12.2^{+0.6"}_{-0.5}$	–	$6.70^{+0.112}_{-0.113} \times 10^{-4}$	–
		$\beta = 0.595^{0.007}_{-0.005}$			
[192] (1)	145, 279	–	–	4.2×10^{-4}	–
[30]	30		$-1.70^{0.10}_{0.11}$	–	–
[30]	30		$-2.90^{+0.21}_{-0.20}$	–	
[125] (2)	30	$\theta_c = 33.6$"	$-1.636^{+0.116}_{-0.114}$	–	–
		$\beta = 0.69$			
[125] (3)	30	$\theta_c = 50.1$"	$-1.590^{0.112}_{-0.113}$	–	–
		$\beta = 0.70$			

Table 8.1: Literature measurements of the SZ signal from Abell 1835. Individual results at a given frequency are not necessarily independent, since some of the results are obtained using the same datasets but different modelling and/ or analysis. Notes: 1. Results obtained using deprojection technique; 2. Profile obtained using X-ray and SZ data, 3. Profile obtained using SZ data only.

$$\Delta I(x) = \frac{-\Delta T g(x) I_0}{2T_{CMB}} = \frac{-\Delta T g(x) T_{CMB}^2 k^3}{c^2 h^2} \tag{8.1}$$

Individual measurements of y_0 and v_p could be converted to intensities using standard equations (see Chapter 2: 'The Sunyaev Zel'dovich Effect: theory and observation').

The values of y_0 and v_p derived by individual experiments will, as noted previously, depend on the model used in the processing. It is clear from Table 8.1, however, that values of the profile parameters can vary substantially between different papers. Furthermore, it was clear that not all the results in the literature were independent. [172], [20] and [19], for example, use the same original dataset. For this reason, it was decided to use one result from each frequency. The results chosen then had to be converted into equivalent measurements given the King model parameters used in this work (i.e. $\theta_c = 33.6$", $\beta = 0.69$). The 30 GHz measurements of [125] are the most recent and used the same King model parameters as in this work, so were chosen along with the 145 and 221 GHz measurements from [137].

The data presented by [137] was obtained using the Sunyaev-Zeldovich Infrared Experiment (SuZIE) instrument [94], mounted on the CSO. SuZIE uses two receivers: SuZIE I and SuZIE II. Both receivers consist of a number of beams separated on the sky (see Fig. 8.1). The FWHM of the beams vary between 1.4' and 1.7' and are separated by up to 5'. Differencing the signal between these beams simulates chopping with throws of between 2.1' and 5'. In the SuZIE I receiver, incoming radiation is measured at a single frequency (145, 221 or 279 GHz), whereas in the SuZIE II receiver, all three frequencies are monitored in each beam. The instrument is then drift scanned by $\sim 30'$ across the source being observed to pro-

Figure 8.1: The arrangement of the SuZIE I and SuZIE II beams. Whereas SuZIE I has a single bolometer, observing at a given frequency (145, 221 or 279 GHz), associated with each beam, SuZIE II can observe at three frequencies simultaneously. (Reproduced from [137].)

duce a 1-dimensional slice with each row of detectors [137]. The start of the scan is also offset by different amounts in different sets of observations so that the source alternates around the centre of the scan in different scans, indicated by the value of δRA

In this analysis, the programs used to simulate the Bolocam observations described previously were modified to reproduce the SuZIE scan strategy with the beam FWHM and separation described in [137] for the D3 and T123 channels (for observations at 145 GHz) and the D2 channel (at 221 GHz). The D3 channel was simulated by two 1.7' beams separated by 4.4'; the T123 channel by three 1.7' beams separated by 2.2', and the D2 channel by two 1.4' beams separated by 4.2'.

Channel	SuZIE measurement	Bolocam equivalent
D3 ($\delta RA = 1080$)	$y_0 = (3.14 \pm 1.11) \times 10^{-4}$	$y_0 = (2.10 \pm 0.74) \times 10^{-4}$
D3 ($\delta RA = 720$)	$y_0 = (3.59 \pm 0.99) \times 10^{-4}$	$y_0 = (2.40 \pm 0.66) \times 10^{-4}$
T123 ($\delta RA = 1080$)	$y_0 = (5.60 \pm 0.79) \times 10^{-4}$	$y_0 = (4.36 \pm 0.62) \times 10^{-4}$
T123 ($\delta RA = 720$)	$y_0 = (5.65 \pm 0.76) \times 10^{-4}$	$y_0 = (4.40 \pm 0.59) \times 10^{-4}$
D2	$v_p = 500 \pm 1000$ kms^{-1}	$v_p = 336 \pm 673$ kms^{-1}

Table 8.2: Literature measurements of the SZ signal from Abell 1835. Individual results at a given frequency are not necessarily independent, since some of the results are obtained using the same datasets but different modelling and/ or analysis.

Reference	Frequency (GHz)	Equivalent intensity ($\beta = 0.69$, $\theta_c = 33.6$")$/I_0$
[125]	30	$(-0.17 \pm 0.02) \times 10^{-3}$
[137]	142	$(-1.40 \pm 0.16) \times 10^{-3}$
[137]	221	$(0.13 \pm 0.26) \times 10^{-3}$
[96]	273	$(1.39 \pm 0.28) \times 10^{-3}$

Table 8.3: Equivalent intensity of results used in the spectral fit (i.e. intensities required to reproduce the results of each experiment using a King model with $\beta = 0.69$ and $\theta_c = 33.6$").

Equivalent values for y_0 and v_p for the Bolocam model could be obtained by first reconstructing maps of the flux of Abell 1835 observed by SuZIE using their King parameter values and their y_0 and v_p results. These models could be 'observed' to produce a simulation of the SuZIE data maps, which could finally be fit using the Bolocam King model parameters to deduce equivalent y_0 values. The final fitting was quick, since only the y_0 parameter needed to be fit for. The results of this analysis are given in Table 8.2.

The Bolocam equivalents give an error-weighted mean of $y_0 = (3.47 \pm 0.33) \times 10^{-4}$. The equivalent values of intensity for each literature result, expressed as a fraction of the reference intensity, I_0 are given in Table 8.3. The plot of these intensity values is given in Fig. 8.2.

The points in this plot were once again fitted, by parameterising the SZ spectrum as:

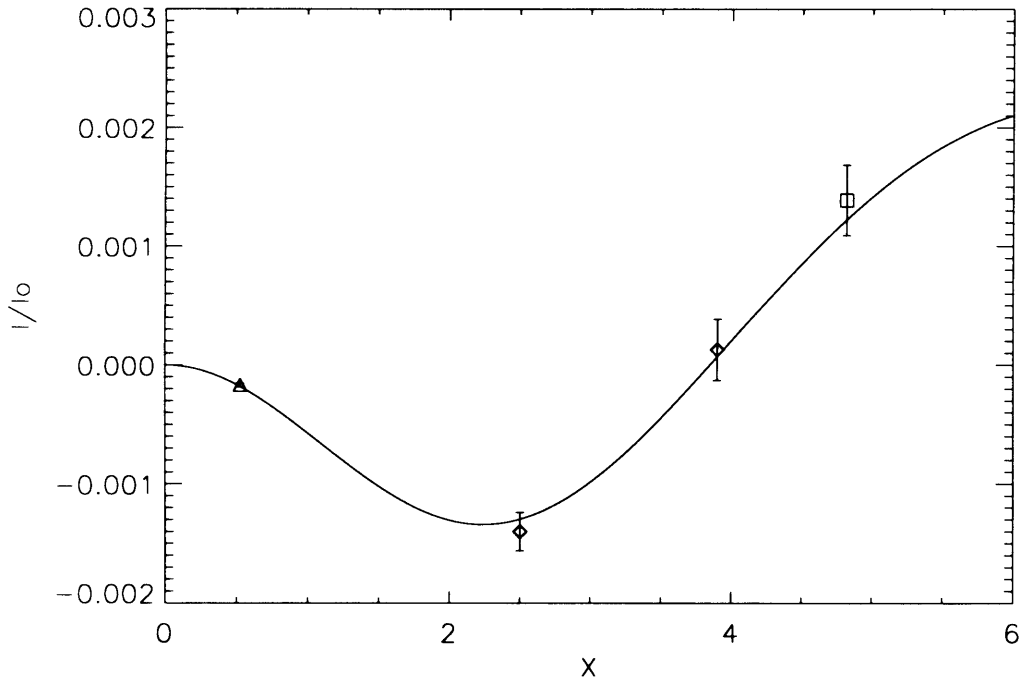

Figure 8.2: The SZ spectrum of Abell 1835. The 30 GHz results (x $\sim$ 0.5) are taken from [125]. The points at 142 and 221 GHz (open diamonds) are from [137], while the open square represents the result obtained here. All points have been renormalised to the central intensity of the SZ effect for a cluster model with $\theta_0 = 33.6''$ and $\beta = 0.69$. The line is the best fit SZ spectrum with $y_0 = 3.60 \times 10^{-4}$ and $v_z = -226$ km/s.

$$\frac{F(x)}{I_0} = A(0)g(x) + A(0)h(x)\mathcal{R}(x) + A(0)A(1)h(x) \tag{8.2}$$

The first term on the right hand side of (8.2) represents the first order thermal SZ; the second term accounts for relativistic corrections to the thermal SZ, and the last term calculates the contribution of the kinetic SZ. The parameters $A(0)$ and $A(1)$ are related to the Compton parameter and the cluster peculiar velocity according to:

$$A(0) \equiv y_0 \tag{8.3}$$

and

$$A(1) \equiv -\frac{k_B T_e}{m_e c^2}\frac{v_p}{c} \tag{8.4}$$

and the $\mathcal{R}(x)$ term represents the relativistic corrections to the thermal SZ described previously. $g(x)$ and $h(x)$ describe the spectral variation of the contributions: their functional form is identical to that described previously (see (2.29) and (2.38)).

The fit was conducted using the standard idl fitting procedure: curvefit.pro. Values of y_0 and v_p which optimize the fit to the spectrum were found to be:

$y_0 = (3.60 \pm 0.24) \times 10^{-4}$,

and $v_p = -226 \pm 275$ kms^{-1}.

These results are consistent with 'typical' values for the Compton parameter and velocity expected from clusters. The kinematic contribution to the SZ signal based on these values is $\sim$ 8% of the thermal contribution. The percentage change between the modelled value for y_0 and the value derived from the spectral fitting is $\sim$ 14%. It appears, therefore, that the kinematic term represents the biggest error on the modelled value of the Compton parameter. The remaining difference could easily be accounted for by dust emission from the central cD galaxy in Abell 1835, as discussed previously (see Chapter 7: 'Parameter fit results and errors').

8.2 Point source temperatures

It is clear that point sources in the field of SZ clusters need to be accurately characterised in order to obtain reliable estimates of the cluster Compton parameter (and associated measurements). In many cases, however, millimetre/ sub-mm point sources have not been studied extensively enough at a range of different frequencies to understand what range of spectral types might exist (and, therefore, to model their effect upon observations confidently).

The original motivation for the data used in this report was to study point sources and in keeping with this aim the measurements of the fluxes for SMM J14009+0252 and SMM J140104+0252 were combined with flux measurements obtained at other frequencies. Measurements of their flux between $\sim$ 200 and 700 GHz are given in Table 8.4 and Table 8.5.

The spectra for both sources were then derived based on this set of data. It has already been noted that the 450μm observations made of Abell 1835 [232] may suffer from problems with the analysis pipeline. It is clear from both Table 8.4

Reference	Wavelength (mm)	Flux (mJy)
[106]	1.35	5.57 ± 1.72
[96]	1.1	11.32 ± 1.92
[232]	0.85	16.0
[106]	0.85	15.6 ± 1.9
[106]	0.45	32.7 ± 8.9
[232]	0.45	-2.0 ± 13.0

Table 8.4: Measurements of flux for SMM J14009+0252, including the value derived in this report.

Reference	Wavelength (mm)	Flux (mJy)
[106]	1.35	6.06 ± 1.46
[64]	1.3	2.5 ± 0.8
[96]	1.1	6.48 ± 2.00
[232]	0.85	13.4
[106]	0.85	14.6 ± 1.8
[106]	0.45	41.9 ± 6.9
[232]	0.45	6 ± 8

Table 8.5: Measurements of flux for SMM J140104+0252, including the value derived in this report.

and Table 8.5, the 450μm points are not consistent with the overall trend of the other results. For the purposes of the initial fitting, therefore, the Zemcov 450μm results were excluded from both spectra.

The spectra were then both fitted with a greybody, as described in Chapter 7: 'Parameter fit results and errors', using a value of $\alpha = 1.5$ [154]:

$$G(\nu, T) \propto \nu^{1.5} B(\nu, T) \tag{8.5}$$

where $B(\nu, T)$ is the ordinary blackbody curve at frequency ν and temperature T. The explicit spectral and temperature dependence of $G(\nu, T)$ is given by:

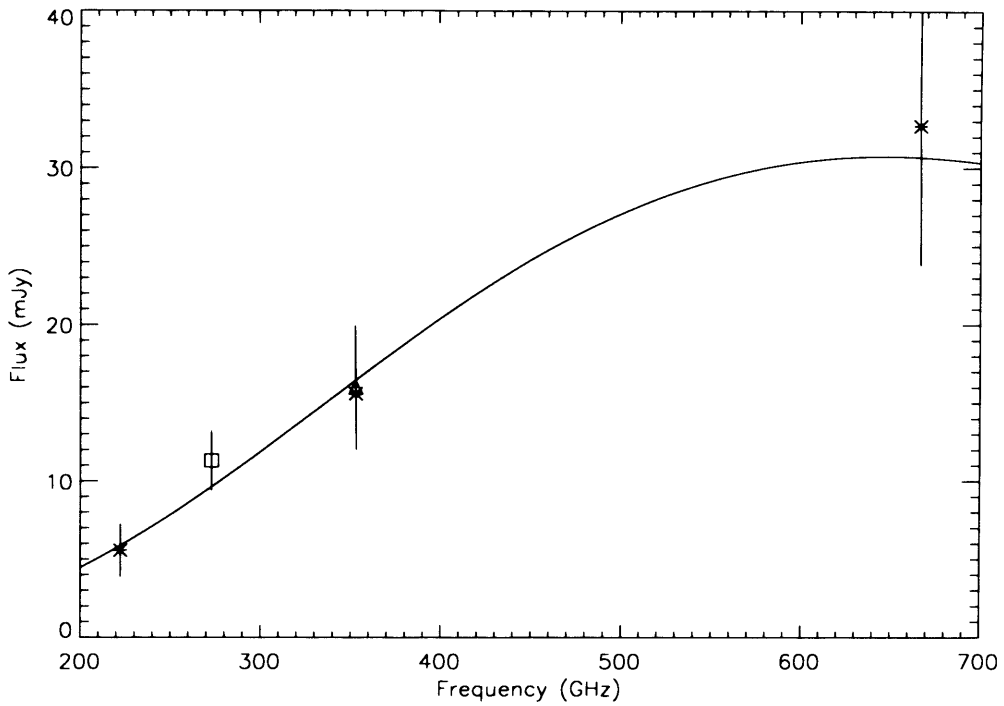

Figure 8.3: Spectrum of SMM J14009+0252 based on the flux measurements given in 8.2. The solid line represents the best-fit greybody spectrum for this set of data, using an index of 1.5. The best fit temperature for the source is found to be 27.5 ± 0.8K. Legend for the plot is: open triangle: [232]; open square: [96], and diagonal-vertical cross: [106].

$$G(\nu, T) \propto \frac{\nu^{4.5}}{expA_1\left(\frac{\nu}{T}\right) - 1} \tag{8.6}$$

with:

$$A_1 = \frac{h}{k_B} \tag{8.7}$$

The results of a simple fit to the spectra using this model are shown in Fig. 8.3 and Fig. 8.4. The effective temperature of the sources, based on these fits were found to be:

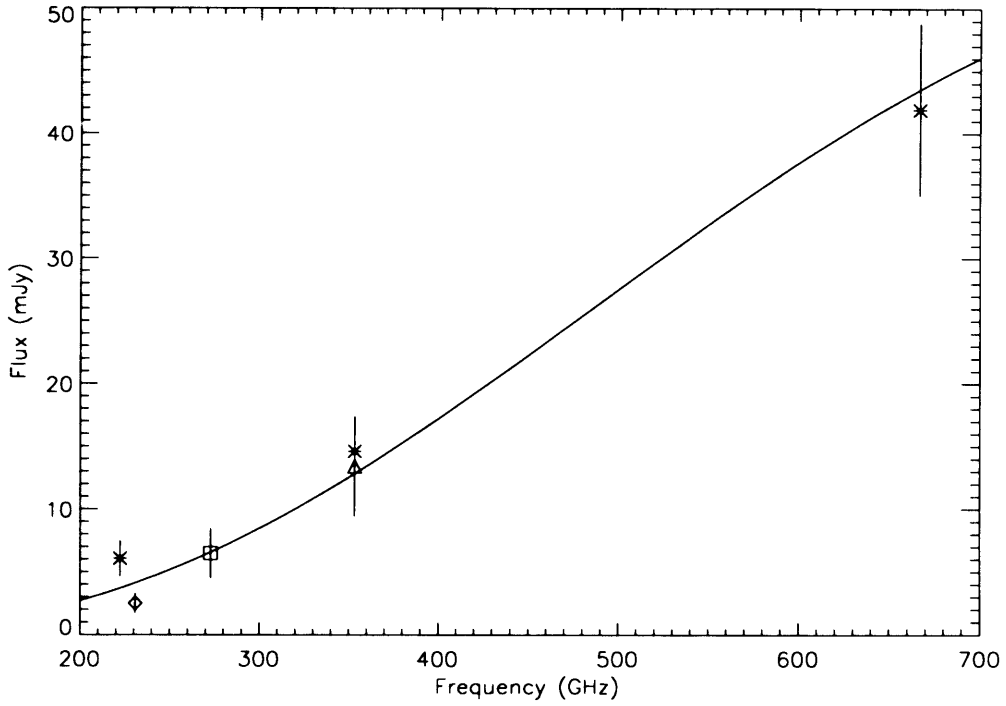

Figure 8.4: Spectrum of SMM J140104+0252 based on the flux measurements given in 8.2. The solid line represents the best-fit greybody spectrum for this set of data, using an index of 1.5. The best fit temperature for the source is found to be 36.6 ± 1.4K. Legend for the plot is: open diamond: [64]; open triangle: [232]; open square: [96], and diagonal-vertical cross: [106].

SMM J14009+0252: 27.5 ± 0.8 K,

and SMM J140104+0252: 36.6 ± 1.4 K.

When corrected for the redshift of the sources, however, these temperatures correspond to 63.3 K and 94.1 K, respectively, which are significantly higher than typical gas temperatures in galaxy clusters.

If the 450μm results of [232] are assumed to be correct, the fits are found to be poor. In order to reproduce the values of flux reported, however, it was found that SMM J14009+0252 would need to have a dust temperature of < 15.8K, whereas SMM J140104+0252 would need to have a dust temperature of < 51.2K (both figures based on the upper value of source flux reported in [232]), which are reasonably consistent with temperatures for these sources derived by *Herschel* [157]. The corresponding upper limits on the flux of the sources at 1.1mm were found to be 3.8 and 14.0 mJy for SMM J14009+0252 and SMM J140104+0252, respectively.

SMM J140104+0252 has been the subject of a number of research papers and is believed to be an ultra-luminous infra-red galaxy (ULIRG) at redshift 2.56 which is being lensed by Abell 1835. The degree to which emission from the galaxy is magnified is a matter of debate. [107] argue that the galaxy is magnified by Abell 1835 as a whole by a factor of ~ 2.5, whereas [64] report evidence that the emission is magnified further by an individual member of Abell 1835 by a factor of ~ 25. In either case, the source is believed to be undergoing intense star-formation: [211] report that the one of the components of SMM J140104+0252 appears to be converting a large proportion of baryonic mass into stars over a relatively short period of time. They also report that the metallicity of the source appears to be high.

There is less information available on SMM J14009+0252. The work that has been done, however, appears to imply that the source has the characteristics of an Extremely Red Oject (ERO) [107], a class of objects which are believed to account for around half of bright sub-mm point sources.

The results presented in this chapter represent the main conclusions of the analysis. In the final chapter, we discuss the results in more detail; describe further work that could be undertaken to extend this study, and present the final conclusions of this thesis.

Chapter 9

Discussion and Conclusions

The results outlined in the previous chapter represent the final results of the data analysis. Even though Abell 1835 is a well-known and well-studied cluster, our estimate of v_p is only the second measurement in the literature. The value derived for v_p also represents the most precise estimate of a cluster's peculiar velocity to date. There are a number of areas of discussion that are raised by our analysis, and several directions in which further research could be carried out. In this chapter, some of these areas are outlined in detail and the final conclusions of the research are presented.

9.1 Further discussion: y_0 and v_p

It is clear from our analysis that one of the greatest sources of error in the accurate determination of the thermal SZ emission in the region of the spectrum where $g(\nu)$ is positive remains dust emission from the cD galaxies in clusters. This is partic-

ularly important at millimetre wavelengths and shorter, where the SZ and dust contribution are expected to be of a similar magnitude. A total characterisation of the SZ spectrum for Abell 1835 also, therefore, requires detailed observations of dust emission, in particular at 850 and 450 μm. While the data at these wavelengths remains inconsistent, it will be difficult to reliably construct and model the dust and SZ contributions using multi-frequency spectral fits. Nevertheless, our results show that there is still good potential for reasonable accuracy to be achieved.

One potential source of error not considered in the analysis of the Bolocam data is due to molecular line emission from galaxies within Abell 1835 at the frequency of observation, in particular due to rotational transitions from Carbon-monoxide (CO). CO is commonly used as a tracer of dust, and is expected to be present in significant quantities in star-forming regions. The J $(3 \rightarrow 2)$ transition, in particular, has a rest frequency of 346 GHz. At the redshift of Abell 1835 ($z = 0.2532$) this corresponds to 276 GHz, which is close to the frequency of observation.

It has already been noted that the value for y_0 derived from the modelling is somewhat higher than that derived from the multifrequency fit. If the observations were to coincide directly with CO J $(3 \rightarrow 2)$ emission, it would seem, based upon preliminary work from the Z-Spec spectrometer [3], that a substantially higher signal would be expected. Nevertheless, it is possible that further spectroscopic work is necessary to rule out the possibility of excess signal from line emission. Z-Spec [75] is ideally suited to this kind of study, capable of observing between 195 and 310 GHz with moderate resolution.

The principal source of error in most measurements of v_p comes from the

CMB (e.g. [85]). The kSZ and the CMB have the same spectral dependence, and are therefore hard to separate. This places strong limits on the precision of measurements of v_p of order 400 - 1600 kms^{-1}. The method of spectral fitting has a clear advantage, therefore, over measurements of v_p based on single observations from single-frequency observations.

As always, however, the accuracy of the fit will be improved significantly by observations at a larger range of frequencies. Observations in the region of the electromagnetic spectrum in which the SZ dominates are limited by the transmission of the atmosphere and so tend to be restricted to a finite number of frequencies. There are several atmospheric windows in the frequency range 30 - 300 GHz and the overall transmission according to atmospheric models remains at a reasonable level. Nevertheless, there are regions in which the transmission falls off rapidly due to absorption by water vapour [153], and these are, naturally, avoided in experiments.

With improved detector technology and analysis techniques, however, there would appear to be good reason to design dedicated SZ experiments which observe at a greater number of frequency bands, even if compromise is required by accepting a slightly reduced atmospheric transmission. Alternatively, space-based detectors should be capable of extending the observations to a greater number of frequencies, as will be possible with the Planck mission.

There already, however, exists data on Abell 1835 from Bolocam which remains unprocessed or has not yet been analysed, which could be used to obtain additional data points on the cluster SZ spectrum. In particular, 2 mm lissajous maps of the cluster made using Bolocam have been constructed but not yet been modelled. In lissajous scanning, the x and y-positions of the telescope beam on the sky are

allowed to vary sinusoidally. Studying this data would not only allow an additional data point to be added to the SZ spectrum of Abell 1835, but allow for a comparison between the different scanning modes.

With greater precision measurements, relativistic corrections to the kinematic SZ will also need to be considered. Analytic formulae for these have been derived by, e.g., [148,149] and compared to direct numerical integration of the collision term of the Boltzmann equation. The agreement between the results is reported to be good. The two highest order terms in the corrections are expected to represent $\sim 8.2\%$ and $\sim 1.3\%$ of the total kinematic contribution.

9.2 Further work

The research presented here has the potential to be improved and extended in a variety of ways.

First, it is likely that the efficiency of the analysis pipeline code could be improved significantly. In particular, the modelling was seriously restricted by the poor sampling of each parameter in the data simulation. This was due mainly to the long time taken to run the modelling code. The section of the code that dealt with reconstructing the chopping using the data R.A. and decl. data took the longest to process. Alternative methods of replicating the chopping that improve the speed of the analysis could, for example, include generating a simulation of the telescope on and off beams, which, when convolved with the ideal sky cluster map, should replicate the chopped data.

Convolving is still a relatively lengthy process in IDL, but it is likely that this

approach would still prove faster than the current code, which involves large nested loops. The potential advantages of improving the coding are substantial. Models where all the fitting parameters are allowed to vary could, for example, be tested. While these kinds of models had been attempted during the analysis, they were abandoned for taking too much time to complete. Larger samples of parameter values could also be sampled, and alternative methods of searching for parameter values which minimise the χ^2 between model and data maps tested.

This may prove important since there remains the possibility that the minima identified in our searches are local rather than global minima in the χ^2 values, and do not, therefore, respresent the real best fit parameters. The only way to increase confidence in the results obtained is to investigate a larger range of parameter values.

Improved processing speed is also essential to repeating the analysis presented here for the other cluster maps. Of the other clusters, Abell 851 contains five point sources, which would need to be included in the map model. Although Abell 851 appears to contain no SZ emission, it would still need to be included in the analysis, bringing the number of parameters characterising the model to eight. MS0451.6-0305 contains four point sources, as well as the cluster emission. As discussed previously, the cluster also contains a lensed arc, which would complicate the modelling further.

As a result, the data maps for MS0451.6-0305 and Abell 1835 would probably be best analysed in order to characterise the point sources in the field. As has already been discussed, extending our knowledge of the spectral characteristics of point sources at millimetre wavelengths is essential to improving our understanding of potential contaminating signal in the field.

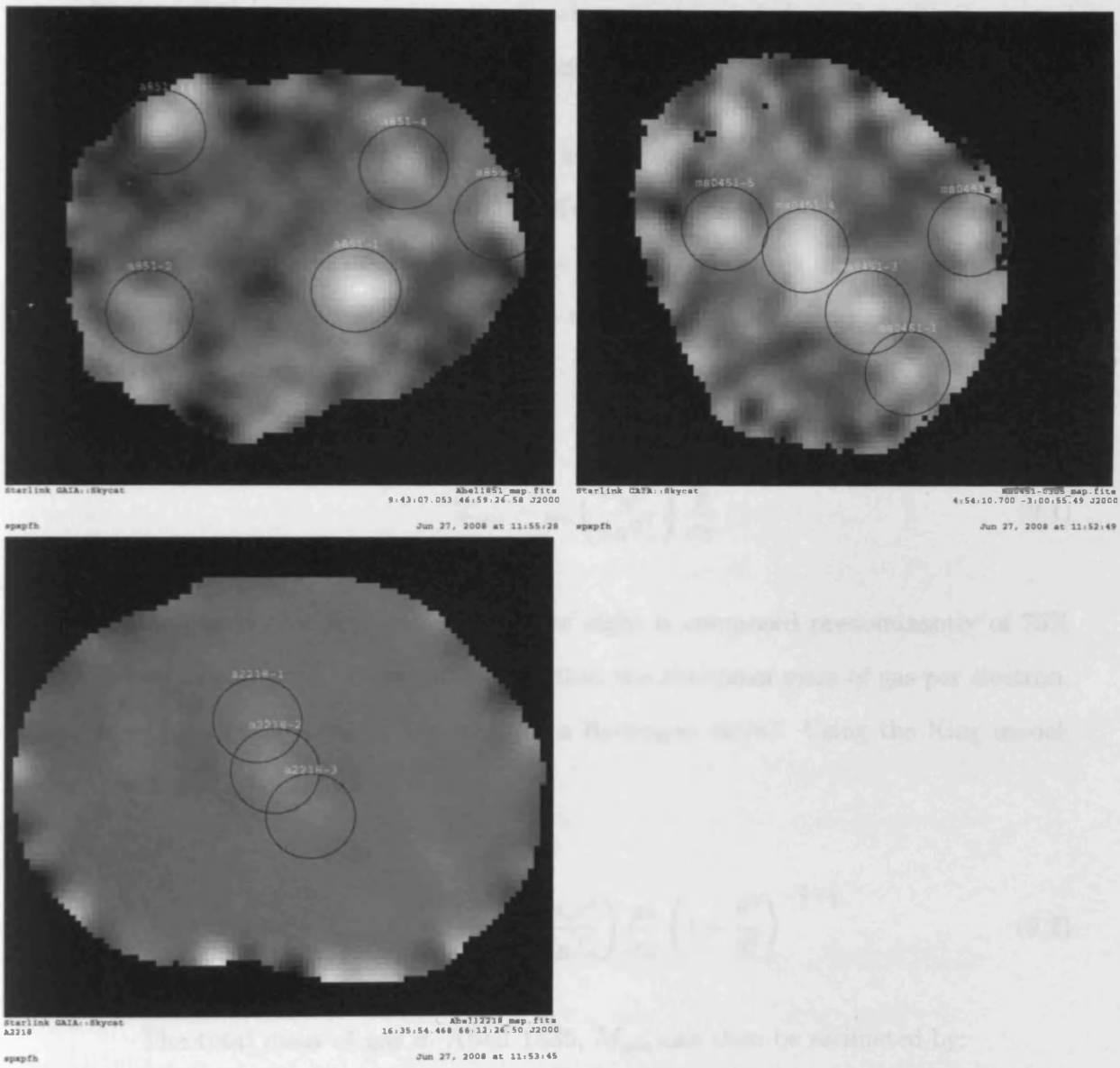

Figure 9.1: SCUBA images of Abell 851 (top left); MS0451.6-0305 (top right), and Abell 2218 (bottom), with the point sources circled. In the cases of MS0451.6-0305 and Abell 2218, the cluster SZ/ dust emission is also circled. Abell 851 appears to contain no significant SZ emission.

Of the four other science sources, however, Abell 2218 is the most similar to Abell 1835. The field contains two point sources as well as the cluster and could be modelled in the same way as already outlined to derive values for its central Compton parameter and peculiar velocity.

There remains, however, much work that could be done to study Abell 1835. In Chapter 2: 'The Sunyaev Zel'dovich effect - theory and observation', for example, it was discussed how observations of the SZ could lead to estimates of the gas mass fraction for a cluster. Recalling (2.41), the surface mass density along a particular line of sight can be given by:

$$\Sigma_{gas} = \mu_e \left(\frac{m_e c^2}{k_B T_e}\right) \frac{y}{\sigma_T} \tag{9.1}$$

Assuming the gas along the line of sight is composed predominantly of 75% Hydrogen and 25% Helium, it follows that the the mean mass of gas per electron, $\mu_e \sim \frac{7}{5} m_H$ (where m_H is the mass of a Hydrogen atom). Using the King model, therefore, (9.1) becomes:

$$\Sigma_{gas}(\theta) = \frac{7}{5} m_H \left(\frac{m_e c^2}{k_B T_e}\right) \frac{y_0}{\sigma_T} \left(1 + \frac{\theta^2}{\theta_c^2}\right)^{-\frac{3}{2}+\frac{\beta}{2}} \tag{9.2}$$

The total mass of gas in Abell 1835, M_{gas} can then be estimated by:

$$M_{gas} = \int \Sigma_{gas}\, 2\pi r dr \tag{9.3}$$

where the integration is over the projected distance from the cluster centre,

r, which, in a flat Universe, is simply related to the angle from the cluster centre by: $r = \theta D$ (where D is the distance of the cluster from Earth). Substituting (9.2) into (9.3) then gives:

$$M_{gas} = \frac{14}{5}\pi D^2 m_H \left(\frac{m_e c^2}{k_B T_e}\right) \frac{y_0}{\sigma_T} \int \theta \left(1 + \frac{\theta^2}{\theta_c^2}\right)^{-\frac{3}{2}+\frac{\beta}{2}} d\theta \tag{9.4}$$

The integral can be evaluated numerically to obtain M_{gas}, and the result compared to the virial mass of the cluster calculated from, for example, weak and strong lensing experiments (see [151, 180]) to estimate the gas mass fraction.

As described in Chapter 2, it should also be possible to combine the SZ observations with X-ray data to obtain an estimate of the Hubble constant. This is, however, likely to be the only cosmologically significant result that can be derived from the measurements obtained here. The true cosmological power of the SZ effect, as has already been outlined, is in the context of cluster surveys.

There remain, however, a number of other lines of research that can be pursued in investigating the physics of Abell 1835 itself, which could provide powerful insights into the process of cluster formation and evolution.

In particular, it is believed that non-gravitational processes within a cluster can lead to an "entropy floor", which has a strong effect upon scaling relationships between different cluster properties [138]. The scaling between X-ray luminosity and emission-weighted electron temperature, for example, are expected to be particularly sensitive to the presence of an entropy floor, and studies of this scaling have provided evidence for complex processes occurring within the ICM of some local clusters ($z < 0.2$). Studies of clusters at higher redshift are, however, hampered

by the rapid decrease in X-ray surface brightness with redshift. As mentioned previously, however, the SZ effect surface brightness does not suffer this degradation with redshift.

[138] discuss how the scaling between SZ parameters and cluster properties are expected to vary with the level of the entropy floor. They find, for example, that the relations between y_0 and the mean emission-weighted gas temperature (T_X); total bolometric X-ray luminosity (L_X), and the mass of dark matter within the radius r_{500} (the radius within which the mean dark matter density is 500 times the critical redshift at the present epoch), $M(r_{500})$, can be parametrised in terms of the 'central entropy', $K_2 = kT_e(0)n_e(0)^{-2/3}$ (where $T_e(0)$ and $n_e(0)$ are the electron temperature and number density, respectively, at the cluster centre) in units of 100 keV cm^2. They characterise these relationships according to:

$$y_0 = A(1+z)^{\gamma} K_2^{\alpha} X^{\beta} \tag{9.5}$$

where $X = T_X$, L_X or $M(r_{500})$; A is a constant (whose value depends on the scaling relationship being examined), and α, γ and β are functions of K_2 and/ or z. In a standard 'self-similar' model of cluster formation, for example, [138] find that y_0 and T_X scale as:

$$y_0 \propto T_X^{1.5} \tag{9.6}$$

whereas in models that include entropy injection (preheating of ICM gas), y_0 and T_X scale as:

$$y_0 \propto T_X^{2.0} \tag{9.7}$$

at $z = 0.2$. At higher redshift the index is also expected to change according to the model, providing an alternative means of distinguishing evolutionary models. Examining the scaling relationships between SZ variable and cluster properties could, therefore, prove an important tool for investigating non-gravitational processes in clusters at earlier times in the Universe's history and provide insight into the role of non-gravitational processes in cluster evolution.

Once more, this application relies on obtaining a sample of clusters at different redshifts. Gaining some insight into the role of non-gravitational processes in Abell 1835 would, however, be of intrinsic worth. Indeed, in this regard, Abell 1835 is particularly interesting, since its mass distribution and X-ray morphology suggests it is not undergoing merger [158]. It could, therefore, serve as a tool for studying 'undisturbed' cluster formation processes. Furthermore, a study of the entropy floor in Abell 1835 would class as the highest redshift observation of its kind, providing 'proof of principle' for this method of studying cluster evolution.

Finally, additional research could be carried out to study the point sources around Abell 1835. It should be possible to estimate the star-formation rate in both SMM J14009+0252 and SMM J140104+0252 by correcting for the magnification produced by gravitational lensing to determine their intrinsic luminosities (at the redshifted frequency of observation). An extended search for measurements of the sources at other wavelengths may also allow an extended SED to be fitted for both, which would have the potential to provide further information on the processes taking place within them, and help our general understanding of sub-mm point sources.

9.3 Concluding remarks

In this report, the mapping and simulation of a set of observations of the X-ray luminous galaxy cluster Abell 1835 has been described. The data on this cluster was based on a set of observations taken in January 2006 using the Bolocam detector, mounted on the CSO, and operating at 1.1 mm (273 GHz). These observations targeted four clusters: MS0451.6-0305; Abell 2218; Abell 851 and Abell 1835. They utilised a jiggle-mapping scan strategy, in which the telescope primary nods between different positions on the sky while the secondary simultaneously chops either side of the main beam. This type of scan strategy is particularly effective at imaging point sources in the field (which were the original targets of the January 2001 run), and is an efficient means of removing sky and telescope noise from the data. Extended sources can also be imaged with jiggle-mapping as long as the size of the source is less than the chop throw.

Since the adopted scan strategy was relatively new for Bolocam, no analysis pipeline existed prior to this project. In the course of the research, therefore, a pipeline was written in IDL which cleaned; deconvolved and mapped individual observation files. In order to obtain fully calibrated science files with accurate pointing reconstruction, it was necessary to observe a number of pointing and calibration sources. Once maps had been generated for each science source observed during the run, they were stacked to produce higher S/N images.

Of the four clusters observed, Abell 1835 was chosen as being the most suitable for SZ analysis. Ideal sky maps were generated based upon a King model for the cluster's SZ profile, then 'observed' by reproducing the telescope chopping during the observations to produce a simulation of the data maps. This process was repeated for different sets of the parameters defining the model. Each map was

compared to the real data by determining a goodness-of-fit (χ^2) value. The set of parameters that minimised the value of the χ^2 was chosen as the best fit model for the cluster.

By this means, the best fit value for the central Compton parameter was found to be $y_0 = (4.19 \pm 0.48) \times 10^{-4}$, while the best fit fluxes of the point sources in the same field as Abell 1835, SMM J140104+0252 and SMM J14009+0252 were found to be 7.17±1.84 mJy, and 12.18±1.77 mJy, respectively. It was found, however, that the best fit set of parameters that defined the King model for these values of y_0 and point source flux were substantially different to typical literature results based on X-ray observations. Since the next stage of the analysis involved comparing different literature values for the SZ emission for Abell 1835 to produce a spectrum, and since this comparison required transferring results obtained using one model into results obtained using the same model as this analysis, it was considered desirable that the King model parameters for all the results in the spectrum should be as close to one another as possible. In this case the set of results with the lowest χ^2 and the most 'standard' set of King model parameters - $\beta = 0.69$ and $\theta_c = 33.6''$ - were chosen to represent our data.

The value of y_0 and point source fluxes in this case were found to be $y_0 = (4.68 \pm 0.48) \times 10^{-4}$; 6.48±2.00, and 11.32±1.92 mJy, respectively. After evaluating other sources of error in the measurement of y_0 and factoring in the effect of dust emission from the central cD galaxy in Abell 1835, the final result for the central Compton parameter based on the Bolocam observations was found to be $y_0 = (4.34 \pm 0.87) \times 10^{-4}$. Other literature values for the SZ intensity from Abell 1835 were obtained by once again simulating ideal sky maps (using our own King model), then observing them using the scan strategy and beam arrangements for each of the experiments whose results were being compared. Given the results

reported by those experiments, it was possible to find the value for y_0 with the standard King model which reproduced the intensity observed by each group.

These individual results were collated to form a spectrum for Abell 1835 which was fit with a SZ function that included both thermal and kinematic components (where the thermal contribution also contained relativistic corrections). Best fit values for y_0 and the cluster peculiar velocity v_p were found to be $y_0 = (3.60 \pm 0.24) \times 10^{-4}$ and $v_p = -226 \pm 275$ kms^{-1}.

Both these results are reasonable and consistent with other literature values. The value derived for v_p in particular represents one of the most precise estimates of cluster peculiar velocity to date. The measurements of the point source fluxes have also been fit with a greybody spectrum with index 1.5 and effective temperatures of 27.5 ± 0.8 and 36.6 ± 1.4 K for SMM J14009+0252 and SMM J140104+0252, respectively. When corrected for redshift, however, these temperatures are higher than would normally be expected for clusters. This may be linked to the physical processes occuring in the sources, although further work would be required to draw any firm conclusions.

In this concluding chapter, the implications of these results and some of the opportunities for further research have been discussed. The substantial amount of interest in SZ research recently has been generated principally because of the potential cosmological results that could be obtained from SZ cluster surveys. It is clear from our analysis, however, that the dust emission from galaxies within clusters has to be accurately removed or modelled in order to obtain reliable estimates of the SZ effect. If single-dish observations are to be used, this may require observations of sources to be made over a large frequency range.

If this issue can be overcome, however, there is good scope for the potential of SZ surveys to be met. While general studies of the SZ effect are likely to be able to provide limits on fundamental cosmological parameters, large scale surveys of the kinematic effect have been cited as a means of investigating the nature of dark energy. Results from large experiments such as ACT, SPT and Planck appear to be best placed to take advantage of this. SZ research on a smaller scale could also, however, have an important role to play in studying the physics and evolution of clusters themselves. One of the most promising extensions of the current work, for example, is to look for evidence of an 'entropy floor' in Abell 1835, which could indicate that non-gravitational processes are occurring (or having occurred) within the cluster. It is clear, therefore, that SZ research is a versatile tool for studying a whole range of astrophysical problems, and is likely to become one of the most important areas in astrophysics research in the next decade.

Appendix A

Relativistic corrections

The relativistic correction to the thermal Sunyaev Zel'dovich effect, $\mathcal{R}(x)$ (as described in Chapter 2: 'Sunyaev Zel'dovich effect: theory and observation'), can be expressed as:

$$\mathcal{R}(x) = \frac{I_0 y x^4 e^x}{(e^x - 1)^2}(\theta_e Y_1 + \theta_e^2 Y_2 + \theta_e^3 Y_3 + \theta_e^4 Y_4) \tag{A.1}$$

where x, y and θ_e have the same definitions as for (2.31). We recall that y also depends linearly on θ_e. The first term in parentheses is, therefore, actually *second*-order in θ_e. The remaining co-efficients, as derived by [105], are lengthy funcions of the variables $\tilde{X} = xcoth(x/2)$ and $\tilde{S} = x/sinh(x/2)$. They are found to be:

$$Y_1 = -10 + \frac{47}{2}\tilde{X} - \frac{42}{5}\tilde{X}^2 + \frac{7}{10}\tilde{X}^3 + \tilde{S}^2\left(-\frac{21}{5} + \frac{7}{5}\tilde{X}\right) \tag{A.2}$$

$$Y_2 = -\frac{15}{2} + \frac{1023}{8}\tilde{X} - \frac{868}{6}\tilde{X}^2 + \frac{329}{5}\tilde{X}^3 - \frac{44}{5}\tilde{X}^4 + \frac{11}{30}\tilde{X}^5 + \tilde{S}^2\left(-\frac{434}{5} + \frac{658}{5}\tilde{X} - \frac{242}{5}\tilde{X}^2 + \frac{143}{30}\tilde{X}^3\right) + \tilde{S}^4\left(-\frac{44}{5} + \frac{187}{60}\tilde{X}\right) \tag{A.3}$$

$$Y_3 = A_{30} + A_{31}\tilde{S}^2 + A_{32}\tilde{S}^4 + A_{33}\tilde{S}^6 \tag{A.4}$$

where:

$$A_{30} = \frac{15}{2} + \frac{2505}{8}\tilde{X} - \frac{7098}{5}\tilde{X}^2 + \frac{14253}{10}\tilde{X}^3 - \frac{18594}{35}\tilde{X}^4 + \frac{12059}{140}\tilde{X}^5 - \frac{128}{21}\tilde{X}^6 + \frac{16}{105}\tilde{X}^7 \tag{A.5}$$

$$A_{31} = -\frac{7098}{10} + \frac{14253}{5}\tilde{X} - \frac{102267}{35}\tilde{X}^2 + \frac{156767}{140}\tilde{X}^3 - \frac{1216}{7}\tilde{X}^4 + \frac{64}{7}\tilde{X}^5 \tag{A.6}$$

$$A_{32} = -\frac{18594}{35} + \frac{205003}{280}\tilde{X} - \frac{1920}{7}\tilde{X}^2 + \frac{1024}{35}\tilde{X}^3 \tag{A.7}$$

and

$$A_{33} = -\frac{544}{21} + \frac{992}{105}\tilde{X} \tag{A.8}$$

Finally:

$$Y_4 = A_{40} + A_{41}\tilde{S}^2 + A_{42}\tilde{S}^4 + A_{43}\tilde{S}^6 + A_{44}\tilde{S}^8 \tag{A.9}$$

where:

$$A_{40} = -\frac{135}{32} + \frac{30375}{128}\tilde{X} - \frac{62391}{10}\tilde{X}^2 + \frac{614727}{40}\tilde{X}^3 - \frac{124389}{10}\tilde{X}^4 + \frac{355703}{80}\tilde{X}^5 - \frac{16568}{21}\tilde{X}^6 + \frac{7516}{105}\tilde{X}^7 - \frac{22}{7}\tilde{X}^8 + \frac{11}{210}\tilde{X}^9 \tag{A.10}$$

$$A_{41} = -\frac{62391}{20} + \frac{614727}{20}\tilde{X} - \frac{1368279}{20}\tilde{X}^2 + \frac{4624139}{80}\tilde{X}^3 - \frac{157396}{7}\tilde{X}^4 + \frac{30064}{7}\tilde{X}^5 - \frac{2717}{7}\tilde{X}^6 + \frac{2761}{210}\tilde{X}^7 \tag{A.11}$$

Order (θ_e)	Intensity/$I_0 y_0$	Contribution of term (% of the first-order intensity)
$\theta_e(non-rel.)$	3.936	–
θ_e^2	-0.865	-22.00
θ_e^3	0.145	3.68
θ_e^4	-0.027	-0.70
θ_e^5	0.006	0.14

Table A.1: Contribution of each term in the relativistic corrections for a standard model for Abell 1835 ($y_0 = 4.34 \times 10^{-4}$; $\mathcal{F}_1 = 6.48$ Jy; $\mathcal{F}_2 = 11.32$ Jy; $\beta = 0.69$, and $\theta_c = 33.6''$). The first column gives the contribution to the dimensionless intensity (unscaled by the central Compton parameter), while the second column gives the contribution of each term as a percentage of the first-order (non-relativistic) term.

$$A_{42} = -\frac{124389}{10} + \frac{6046951}{160}\tilde{X} - \frac{248520}{7}\tilde{X}^2 + \frac{481024}{35}\tilde{X}^3 - \frac{15972}{7}\tilde{X}^4 + \frac{18689}{140}\tilde{X}^5 \tag{A.12}$$

$$A_{43} = -\frac{70414}{21} + \frac{465992}{105}\tilde{X} - \frac{11792}{7}\tilde{X}^2 + \frac{19778}{105}\tilde{X}^3 \tag{A.13}$$

and

$$A_{44} = -\frac{682}{7} + \frac{7601}{210}\tilde{X} \tag{A.14}$$

In the course of the processing the contribution of each term, as a percentage of the non-relativistic thermal SZ intensity (first-order in θ_e), were evaluated for an electron temperature of $8.3keV$. The relative contribution of each of the terms are given in Table A.1.

Appendix B

200601 Bolocam observing run

The complete list of observations for the January 2006 Bolocam run, including the observation period for each file, is included below.

Date	Filename	Source	Type	Observing duration (s)
31 Jan 2006	060131_o29	0923p392_4cp39.25	Pointing/ calibration	551.0
31 Jan 2006	060131_o30	Abell 851	Cluster	2896.0
31 Jan 2006	060131_o31	0923p392_4cp39.25	Pointing/ calibration	389.0
31 Jan 2006	060131_o32	0923p392_4cp39.25	Pointing/ calibration	502.0
31 Jan 2006	060131_o33	0923p392_4cp39.25	Pointing/ calibration	659.0
31 Jan 2006	060131_o34	0923p392_4cp39.25	Pointing/ calibration	567.0
31 Jan 2006	060131_o35	Abell 851	Cluster	2916.0
31 Jan 2006	060131_o36	0923p392_4cp39.25	Pointing/ calibration	524.0
31 Jan 2006	060131_o37	Abell 851	Cluster	2919.0
31 Jan 2006	060131_o38	0923p392_4cp39.25	Pointing/ calibration	513.0
31 Jan 2006	060131_o39	Abell 851	Cluster	2922.0
31 Jan 2006	060131_o40	0923p392_4cp39.25	Pointing/ calibration	528.0
31 Jan 2006	060131_o41	Abell 851	Cluster	3011.0
31 Jan 2006	060131_o42	0923p392_4cp39.25	Pointing/ calibration	668.0
31 Jan 2006	060131_o43	Abell 851	Cluster	3044.0
31 Jan 2006	060131_o44	0923p392_4cp39.25	Pointing/ calibration	951.0
31 Jan 2006	060131_o45	1334-127	Pointing/ cluster	553.0
31 Jan 2006	060131_o46	Abell 1835	Cluster	3033.0
31 Jan 2006	060131_o47	1334-127	Pointing/ cluster	566.0
31 Jan 2006	060131_o48	Abell 1835	Cluster	2957.0
31 Jan 2006	060131_o49	1334-127	Pointing/ cluster	555.0
01 Feb 2006	060201_ob9	0458m020	Pointing/ cluster	559.0
01 Feb 2006	060201_o10	ms0451	Cluster	2956.0
01 Feb 2006	060201_o11	0420m014	Pointing/ calibration	681.0
01 Feb 2006	060201_o12	Mars	Pointing/ calibration	21872.0
01 Feb 2006	060201_o13	0923p392_4cp39.25	Pointing/ calibration	590.0
01 Feb 2006	060201_o14	Abell 851	Cluster	3079.0
01 Feb 2006	060201_o15	0923p392_4cp39.25	Pointing/ calibration	959.0
01 Feb 2006	060201_o16	1334-127	Pointing/ cluster	586.0
01 Feb 2006	060201_o17	Abell 1835	Cluster	3095.0
01 Feb 2006	060201_o18	1334-127	Pointing/ cluster	566.0
01 Feb 2006	060201_o19	Abell 1835	Cluster	3012.0
01 Feb 2006	060201_o20	1334-127	Pointing/ cluster	717.0
01 Feb 2006	060201_o21	Abell 1835	Cluster	3104.0
01 Feb 2006	060201_o22	1334-127	Pointing/ cluster	579.0
01 Feb 2006	060201_o23	Abell 1835	Cluster	3179.0
02 Feb 2006	060202_ob1	1334-127	Pointing/ cluster	562.0
02 Feb 2006	060202_ob2	Abell 1835	Cluster	3050.0
02 Feb 2006	060202_ob3	1334-127	Pointing/ cluster	571.0

03 Feb 2006	060203_ob1	0458m020	Pointing/ cluster	536.0
03 Feb 2006	060203_ob2	ms0451	Cluster	3092.0
03 Feb 2006	060203_ob3	0420m014	Pointing/ calibration	520.0
03 Feb 2006	060203_ob4	ms0451	Cluster	2964.0
03 Feb 2006	060203_ob5	0420m014	Pointing/ calibration	27088.0
03 Feb 2006	060203_ob6	1334-127	Pointing/ cluster	554.0
03 Feb 2006	060203_ob7	Abell 1835	Cluster	3043.0
03 Feb 2006	060203_ob8	1334-127	Pointing/ cluster	567.0
03 Feb 2006	060203_ob9	Abell 1835	Cluster	2956.0
03 Feb 2006	060203_o10	1334-127	Pointing/ cluster	560.0
03 Feb 2006	060203_o11	Abell 1835	Cluster	3057.0
03 Feb 2006	060203_o12	1334-127	Pointing/ cluster	600.0
03 Feb 2006	060203_o13	Abell 1835	Cluster	3102.0
04 Feb 2006	060204_ob1	0420m014	Pointing/ calibration	531.0
04 Feb 2006	060204_ob2	ms0451	Cluster	3012.0
04 Feb 2006	060204_ob3	0420m014	Pointing/ calibration	623. 0
04 Feb 2006	060204_ob4	ms0451	Cluster	2944.0
04 Feb 2006	060204_ob5	0420m014	Pointing/ calibration	504.0
04 Feb 2006	060204_ob6	ms0451	Cluster	2926.0
04 Feb 2006	060204_ob7	0420m014	Pointing/ calibration	557.0
04 Feb 2006	060204_ob8	Mars	Pointing/ calibration	25105.0
04 Feb 2006	060204_ob9	1334-127	Pointing/ cluster	563.0
04 Feb 2006	060204_o10	Abell 1835	Cluster	3064.0
04 Feb 2006	060204_o11	1334-127	Pointing/ cluster	562.0
04 Feb 2006	060204_o12	Abell 1835	Cluster	3000.0
04 Feb 2006	060204_o13	1334-127	Pointing/ cluster	589.0
04 Feb 2006	060204_o14	Abell 1835	Cluster	3079.0
04 Feb 2006	060204_o16	Abell 1835	Cluster	3078.0
05 Feb 2006	060205_ob1	0420m014	Pointing/ calibration	565.0
05 Feb 2006	060205_ob2	ms0451	Cluster	3002.0
05 Feb 2006	060205_ob3	0420m014	Pointing/ calibration	527.0
05 Feb 2006	060205_ob4	ms0451	Cluster	2945.0
05 Feb 2006	060205_ob5	0420m014	Pointing/ calibration	605.0
05 Feb 2006	060205_ob6	Mars	Pointing/ calibration	485.0
05 Feb 2006	060205_ob7	Mars	Pointing/ calibration	2878.0
05 Feb 2006	060205_ob8	0420m014	Pointing/ calibration	550.0
05 Feb 2006	060205_ob9	ms0451	Cluster	2487.0
06 Feb 2006	060206_ob1	0420m014	Pointing/ calibration	541.0
06 Feb 2006	060206_ob2	ms0451	Cluster	3011.0
06 Feb 2006	060206_ob3	0420m014	Pointing/ calibration	518.0
06 Feb 2006	060206_ob4	ms0451	Cluster	2944.0

06 Feb 2006	060206_ob5	0420m014	Pointing/ calibration	506.0
06 Feb 2006	060206_ob6	ms0451	Cluster	2957.0
06 Feb 2006	060206_ob7	0420m014	Pointing/ calibration	620.0
06 Feb 2006	060206_ob8	Mars	Pointing/ calibration	24759
06 Feb 2006	060206_ob9	1334-127	Pointing/ cluster	814.0
06 Feb 2006	060206_o10	3c371	Pointing/ calibration	605.0
06 Feb 2006	060206_o11	Abell 2218	Cluster	3081.0
06 Feb 2006	060206_o12	3c371	Pointing/ calibration	574.0
06 Feb 2006	060206_o13	Abell 2218	Cluster	3069.0
06 Feb 2006	060206_o14	3c371	Pointing/ calibration	549.0
06 Feb 2006	060206_o15	Abell 2218	Cluster	3058.0
06 Feb 2006	060206_o16	3c371	Pointing/ calibration	618.0
07 Feb 2006	060207_ob1	3c371	Pointing/ calibration	526.0
07 Feb 2006	060207_ob2	Abell 2218	Cluster	2754.0
08 Feb 2006	060208_ob1	0923p392_4cp39.25	Pointing/ calibration	532.0
08 Feb 2006	060208_ob2	Abell 851	Cluster	2927.0
08 Feb 2006	060208_ob3	0923p392_4cp39.25	Pointing/ calibration	518.0
08 Feb 2006	060208_ob4	Abell 851	Cluster	2997.0
08 Feb 2006	060208_ob5	0923p392_4cp39.25	Pointing/ calibration	511.0
08 Feb 2006	060208_ob6	Abell 851	Cluster	3037.0
08 Feb 2006	060208_ob7	0923p392_4cp39.25	Pointing/ calibration	523.0
08 Feb 2006	060208_ob8	Abell 851	Cluster	3029.0
08 Feb 2006	060208_ob9	0923p392_4cp39.25	Pointing/ calibration	463.0
08 Feb 2006	060208_o14	3c371	Pointing/ calibration	550.0
08 Feb 2006	060208_o15	Abell 2218	Cluster	3089
08 Feb 2006	060208_o16	3c371	Pointing/ calibration	424.0
09 Feb 2006	060209_ob1	3c371	Pointing/ calibration	534.0
09 Feb 2006	060209_ob2	Abell 2218	Cluster	3071.0
09 Feb 2006	060209_ob3	3c371	Pointing/ calibration	438.0
10 Feb 2006	060210_ob1	3c371	Pointing/ calibration	533.0
10 Feb 2006	060210_ob2	Abell 2218	Cluster	3087.0
10 Feb 2006	060210_ob3	3c371	Pointing/ calibration	531.0
10 Feb 2006	060210_ob4	Abell 2218	Cluster	3073.0
10 Feb 2006	060210_ob5	3c371	Pointing/ calibration	507.0

Table B.1: Complete observing run for the Jan/ Feb 2006 Bolocam observing run, headed by E. Egami. Observations of science sources (clusters) are bracketed by observations of pointing/ calibration sources. Most of these sources are secondary, although there are also a number of observations of Mars. Clearly, since pointing and calibration sources are intrinsically brighter, observations of these sources need not be as long as for the individual science sources. Indeed, individual observations of the science sources do not produce a high enough signal-to-noise map for the sources to be distinguished.

Bibliography

[1] N. Aghanim, S. H. Hansen, and G. Lagache. Trouble for cluster parameter estimation from blind SZ surveys? A&A, 439:901–912, September 2005.

[2] N. Aghanim, S. Majumdar, and J. Silk. Secondary anisotropies of the CMB. *Reports on Progress in Physics*, 71(6):066902–+, June 2008.

[3] Ass. Prof. James Aguirre. Private Communication.

[4] A. Albrecht, G. Bernstein, R. Cahn, W. L. Freedman, J. Hewitt, W. Hu, J. Huth, M. Kamionkowski, E. W. Kolb, L. Knox, J. C. Mather, S. Staggs, and N. B. Suntzeff. Report of the Dark Energy Task Force. *ArXiv Astrophysics e-prints*, September 2006.

[5] S. W. Allen. Starbursts in cooling flows: blue continua and emission-line nebulae in central cluster galaxies. MNRAS, 276:947–960, October 1995.

[6] S. W. Allen and A. C. Fabian. The impact of cooling flows on the T_X-L_Bol relation for the most luminous clusters. MNRAS, 297:L57–L62, July 1998.

[7] H. Andernach, R. Wielebinski, D. Schallwich, and G. B. Sholomitskii. A search for microwave background diminution towards the cluster 0016 + 16. A&A, 124:326–330, August 1983.

[8] N. A. Bahcall and R. Cen. The mass function of clusters of galaxies. ApJ, 407:L49–L52, April 1993.

[9] A. Balbi. Cosmology from Planck. *New Astronomy Review*, 51:281–286, March 2007.

[10] L. Ball and J. G. Kirk. Probing pulsar winds using inverse compton scattering. *Astroparticle Physics*, 12:335–349, January 2000.

[11] D. Barbosa, J. G. Bartlett, A. Blanchard, and J. Oukbir. The Sunyaev-Zel'dovich effect and the value of Ω_0. A&A, 314:13–17, October 1996.

[12] J. G. Bartlett. SZ Surveys are Coming: What should we do? *ArXiv Astrophysics e-prints*, June 2006.

[13] N. Battaglia, J. R. Bond, C. Pfrommer, J. L. Sievers, and D. Sijacki. Simulations of the Sunyaev-Zel'dovich Power Spectrum with AGN Feedback. *ArXiv e-prints*, March 2010.

[14] E. S. Battistelli, M. De Petris, L. Lamagna, G. Luzzi, R. Maoli, A. Melchiorri, F. Melchiorri, A. Orlando, E. Palladino, G. Savini, Y. Rephaeli, M. Shimon, M. Signore, and S. Colafrancesco. Triple Experiment Spectrum of the Sunyaev-Zel'dovich Effect in the Coma Cluster: H_0. ApJ, 598 : $L75 - -L78, December 2003$.

[15] R. A. Battye and J. Weller. Constraining cosmological parameters using Sunyaev-Zel'dovich cluster surveys. Phys. Rev. D, 68(8):083506–+, October 2003.

[16] W. Bednarek. Inverse Compton scattering model for gamma-ray production in MeV blazars. MNRAS, 294:439–+, March 1998.

[17] C. L. Bennett, M. Bay, M. Halpern, G. Hinshaw, C. Jackson, N. Jarosik, A. Kogut, M. Limon, S. S. Meyer, L. Page, D. N. Spergel, G. S. Tucker, D. T. Wilkinson, E. Wollack, and E. L. Wright. The Microwave Anisotropy Probe Mission. ApJ, 583:1–23, January 2003.

[18] A. J. Benson, C. Reichardt, and M. Kamionkowski. Statistics of Sunyaev-Zel'dovich cluster surveys. MNRAS, 331:71–84, March 2002.

[19] B. A. Benson, S. E. Church, P. A. R. Ade, J. J. Bock, K. M. Ganga, C. N. Henson, and K. L. Thompson. Measurements of Sunyaev-Zel'dovich Effect Scaling Relations for Clusters of Galaxies. ApJ, 617:829–846, December 2004.

[20] B. A. Benson, S. E. Church, P. A. R. Ade, J. J. Bock, K. M. Ganga, J. R. Hinderks, P. D. Mauskopf, B. Philhour, M. C. Runyan, and K. L. Thompson. Peculiar Velocity Limits from Measurements of the Spectrum of the Sunyaev-Zeldovich Effect in Six Clusters of Galaxies. ApJ, 592:674–691, August 2003.

[21] S. Bhattacharya and A. Kosowsky. Dark energy constraints from galaxy cluster peculiar velocities. Phys. Rev. D, 77(8):083004–+, April 2008.

[22] R. M. Bielby and T. Shanks. Anomalous SZ contribution to three-year WMAP data. MNRAS, 382:1196–1202, December 2007.

[23] M. Birkinshaw. The Sunyaev-Zel'dovich effect. Phys. Rep., 310:97–195, March 1999.

[24] M. Birkinshaw. Using the Sunyaev-Zel'dovich Effect to Probe the Gas in Clusters. *Clusters of Galaxies: Probes of Cosmological Structure and Galaxy Evolution*, pages 161–+, 2004.

[25] M. Birkinshaw, S. F. Gull, and H. Hardebeck. The Sunyaev-Zeldovich effect towards three clusters of galaxies. Nature, 309:34–+, May 1984.

[26] M. Birkinshaw, J. P. Hughes, and K. A. Arnaud. A measurement of the value of the Hubble constant from the X-ray properties and the Sunyaev-Zel'dovich effect of Abell 665. ApJ, 379:466–481, October 1991.

[27] C.-I. Björnsson and C. Fransson. The X-Ray and Radio Emission from SN 2002ap: The Importance of Compton Scattering. ApJ, 605:823–829, April 2004.

[28] A. W. Blain. Gravitational lensing and the Sunyaev-Zel'dovich effect in the millimetre/submillimetre waveband. MNRAS, 297:502–510, June 1998.

[29] Prof. Andrew Blain. Private Communication.

[30] M. Bonamente, M. K. Joy, S. J. LaRoque, J. E. Carlstrom, E. D. Reese, and K. S. Dawson. Determination of the Cosmic Distance Scale from Sunyaev-Zel'dovich Effect and Chandra X-Ray Measurements of High-Redshift Galaxy Clusters. ApJ, 647:25–54, August 2006.

[31] C. Borys, S. Chapman, M. Donahue, G. Fahlman, M. Halpern, J.-P. Kneib, P. Newbury, D. Scott, and G. P. Smith. The nature of a gravitationally lensed submillimetre arc in MS0451.6-0305: two interacting galaxies at z~ 2.9? MNRAS, 352:759–767, August 2004.

[32] F. R. Bouchet. The Planck Satellite: Status Perspectives. *ArXiv e-prints*, November 2009.

[33] S. Bowyer and T. W. Berghöfer. Inverse Compton Scattering as the Source of Diffuse Extreme-Ultraviolet Emission in the Coma Cluster of Galaxies. ApJ, 506:502–508, October 1998.

[34] D. B. Cannon, T. J. Ponman, and I. S. Hobbs. The mass and dynamical state of Abell 2218. MNRAS, 302:9–21, January 1999.

[35] J. E. Carlstrom, P. A. R. Ade, K. A. Aird, B. A. Benson, L. E. Bleem, S. Busetti, C. L. Chang, E. Chauvin, H. -. Cho, T. M. Crawford, A. T. Crites, M. A. Dobbs, N. W. Halverson, S. Heimsath, W. L. Holzapfel, J. D. Hrubes, M. Joy, R. Keisler, T. M. Lanting, A. T. Lee, E. M. Leitch, J. Leong, W. Lu, M. Lueker, J. J. McMahon, J. Mehl, S. S. Meyer, J. J. Mohr, T. E. Montroy, S. Padin, T. Plagge, C. Pryke, J. E. Ruhl, K. K. Schaffer, D. Schwan, E. Shirokoff, H. G. Spieler, Z. Staniszewski, A. A. Stark, and K. V. J. D. Vieira. The 10 Meter South Pole Telescope. *ArXiv e-prints*, July 2009.

[36] J. E. Carlstrom, G. P. Holder, and E. D. Reese. Cosmology with the Sunyaev-Zel'dovich Effect. ARA&A, 40:643–680, 2002.

[37] A. Cavaliere, L. Danese, and G. de Zotti. Cosmic distances from X-ray and microwave observations of clusters of galaxies. A&A, 75:322–325, June 1979.

[38] R. Cen. Decaying Cold Dark Matter Model and Small-Scale Power. ApJ, 546:L77–L80, January 2001.

[39] A. Challinor and A. Lasenby. Relativistic Corrections to the Sunyaev-Zeldovich Effect. ApJ, 499:1–+, May 1998.

[40] S. Chandrasekhar. *Radiative Transfer.* Dover, 1950.

[41] S. Chatterjee, T. Di Matteo, A. Kosowsky, and I. Pelupessy. Simulations of the Sunyaev-Zel'dovich effect from quasars. MNRAS, 390:535–544, October 2008.

[42] S. Chatterjee and A. Kosowsky. The Sunyaev-Zel'dovich Effect from Quasar Feedback. ApJ, 661:L113–L116, June 2007.

[43] S. Colafrancesco. The SZ effect from cluster cavities. A&A, 435:L9–L12, May 2005.

[44] S. Colafrancesco. Beyond the standard lore of the SZ effect. *New Astronomy Review*, 51:394–405, March 2007.

[45] S. Colafrancesco. SZ effect from radio-galaxy lobes: astrophysical and cosmological relevance. MNRAS, 385:2041–2048, April 2008.

[46] S. Colafrancesco and P. Marchegiani. On the ability of spectroscopic SZ effect measurements to determine the temperature structure of galaxy clusters. *ArXiv e-prints*, December 2009.

[47] S. Colafrancesco, P. Marchegiani, and E. Palladino. The non-thermal Sunyaev-Zel'dovich effect in clusters of galaxies. A&A, 397:27–52, January 2003.

[48] A. Cooray, D. Baumann, and K. Sigurdson. Statistical imprints of SZ effects in the cosmic microwave background. In F. Melchiorri & Y. Rephaeli, editor, *Background Microwave Radiation and Intracluster Cosmology*, pages 309–+, 2005.

[49] A. R. Cooray, L. Grego, W. L. Holzapfel, M. Joy, and J. E. Carlstrom. Radio Sources in Galaxy Clusters at 28.5 GHz. AJ, 115:1388–1399, April 1998.

[50] C. S. Crawford, S. W. Allen, H. Ebeling, A. C. Edge, and A. C. Fabian. The ROSAT Brightest Cluster Sample - III. Optical spectra of the central cluster galaxies. MNRAS, 306:857–896, July 1999.

[51] J. V. Cunha, L. Marassi, and J. A. S. Lima. Constraining H_0 from the Sunyaev-Zel'dovich effect, galaxy cluster X-ray data and baryon oscillations. MNRAS, 379:L1–L5, July 2007.

[52] A. J. C. da Silva. SZ scaling relations in Galaxy Clusters: Results from hydrodynamical N-body simulations. Ap&SS, 290:167–176, February 2004.

[53] Z. G. Dai, B. Zhang, and E. W. Liang. GRB 060218/SN 2006aj: Prompt Emission from Inverse-Compton Scattering of Shock Breakout Thermal Photons. *ArXiv Astrophysics e-prints*, April 2006.

[54] K. S. Dawson, W. L. Holzapfel, J. E. Carlstrom, M. Joy, S. J. LaRoque, A. D. Miller, and D. Nagai. Measurement of Arcminute-Scale Cosmic Microwave Background Anisotropy with the Berkeley-Illinois-Maryland Association Array. ApJ, 581:86–95, December 2002.

[55] P. de Bernardis, P. A. R. Ade, R. Artusa, J. J. Bock, A. Boscaleri, B. P. Crill, G. De Troia, P. C. Farese, M. Giacometti, V. V. Hristov, A. Iacoangeli, A. E. Lange, A. T. Lee, S. Masi, L. Martinis, P. V. Mason, P. D. Mauskopf, F. Melchiorri, L. Miglio, T. Montroy, C. B. Netterfield, E. Pascale, F. Piacentini, P. L. Richards, J. E. Ruhl, and F. Scaramuzzi. Mapping the CMB sky: THE BOOMERanG experiment. *New Astronomy Review*, 43:289–296, July 1999.

[56] E. de Filippis, S. Schindler, and A. Castillo-Morales. XMM observation of the dynamically young galaxy cluster CL 0939+4713. A&A, 404:63–74, June 2003.

[57] G. de Zotti, C. Burigana, A. Cavaliere, L. Danese, G. L. Granato, A. Lapi, P. Platania, and L. Silva. The Sunyaev-Zeldovich effect as a probe of the galaxy formation process. In G. Bertin, D. Farina, & R. Pozzoli, editor, *Plasmas in the Laboratory and in the Universe: New Insights and New Challenges*, volume 703 of *American Institute of Physics Conference Series*, pages 375–384, April 2004.

[58] S. DeDeo, D. N. Spergel, and H. Trac. The kinetic Sunyaev-Zel'dovitch effect as a dark energy probe. *ArXiv Astrophysics e-prints*, November 2005.

[59] R. H. Dicke, P. J. E. Peebles, P. G. Roll, and D. T. Wilkinson. Cosmic Black-Body Radiation. ApJ, 142:414–419, July 1965.

[60] J. M. Diego. Cosmology with Galaxy Clusters through the Sunyaev-Zel'dovich effect. *ArXiv Astrophysics e-prints*, November 2002.

[61] J. M. Diego, E. Martínez-González, J. L. Sanz, N. Benitez, and J. Silk. The Sunyaev-Zel'dovich effect as a cosmological discriminator. MNRAS, 331:556–568, April 2002.

[62] J. M. Diego, E. Martínez-González, J. L. Sanz, L. Cayón, and J. Silk. Constraining our Universe with X-ray and optical cluster data. MNRAS, 325:1533–1545, August 2001.

[63] S. Dodelson. *Modern Cosmology.* Elsevier, 2003.

[64] D. Downes and P. M. Solomon. Molecular Gas and Dust at z=2.6 in SMM J14011+0252: A Strongly Lensed Ultraluminous Galaxy, Not a Huge Massive Disk. ApJ, 582:37–48, January 2003.

[65] A. Dressler, J. Rigby, A. Oemler, J. Fritz, B. M. Poggianti, G. Rieke, and L. Bai. Spitzer 24 μm Detections of Starburst Galaxies in Abell 851. ApJ, 693:140–151, March 2009.

[66] A. C. Edge, R. J. Ivison, I. Smail, A. W. Blain, and J.-P. Kneib. The detection of dust in the central galaxies of distant cooling-flow clusters. MNRAS, 306:599–606, July 1999.

[67] E. Egami, J.-P. Kneib, G. H. Rieke, R. S. Ellis, J. Richard, J. Rigby, C. Papovich, D. Stark, M. R. Santos, J.-S. Huang, H. Dole, E. Le Floc'h, and P. G. Pérez-González. Spitzer and Hubble Space Telescope Constraints on the Physical Properties of the z $\sim$ 7 Galaxy Strongly Lensed by A2218. ApJ, 618:L5–L8, January 2005.

[68] A. E. Evrard. The intracluster gas fraction in X-ray clusters - Constraints on the clustered mass density. MNRAS, 292:289–+, December 1997.

[69] J. W. Fowler, V. Acquaviva, P. A. R. Ade, P. Aguirre, M. Amiri, J. W. Appel, L. F. Barrientos, E. S. Battistelli, J. R. Bond, B. Brown, B. Burger, J. Chervenak, S. Das, M. J. Devlin, S. R. Dicker, W. B. Doriese, J. Dunkley, R. Dünner, T. Essinger-Hileman, R. P. Fisher, A. Hajian, M. Halpern, M. Hasselfield, C. Hernández-Monteagudo, G. C. Hilton, M. Hilton, A. D. Hincks, R. Hlozek, K. M. Huffenberger, D. H. Hughes, J. P. Hughes, L. Infante, K. D. Irwin, R. Jimenez, J. B. Juin, M. Kaul, J. Klein, A. Kosowsky, J. M. Lau, M. Limon, Y.-T. Lin, R. H. Lupton, T. A. Marriage, D. Marsden, K. Martocci, P. Mauskopf, F. Menanteau, K. Moodley, H. Moseley, C. B. Netterfield, M. D. Niemack, M. R. Nolta, L. A. Page, L. Parker, B. Partridge, H. Quintana, B. Reid, N. Sehgal, J. Sievers, D. N. Spergel, S. T. Staggs, D. S. Swetz, E. R. Switzer, R. Thornton, H. Trac, C. Tucker, L. Verde, R. Warne, G. Wilson, E. Wollack, and Y. Zhao. The Atacama Cosmology Telescope: A Measurement of the 600 ell 8000 Cosmic Microwave Background Power Spec trum at 148 GHz. ApJ, 722:1148–1161, October 2010.

[70] J. W. Fowler, M. D. Niemack, S. R. Dicker, A. M. Aboobaker, P. A. R. Ade, E. S. Battistelli, M. J. Devlin, R. P. Fisher, M. Halpern, P. C. Hargrave, A. D. Hincks, M. Kaul, J. Klein, J. M. Lau, M. Limon, T. A. Marriage, P. D. Mauskopf, L. Page, S. T. Staggs, D. S. Swetz, E. R. Switzer, R. J. Thornton, and C. E. Tucker. Optical design of the Atacama Cosmology Telescope and the Millimeter Bolometric Array Camera. Appl. Opt., 46:3444–3454, June 2007.

[71] J. Geisbüsch and M. P. Hobson. Cosmology with the Planck cluster sample. MNRAS, 382:158–176, November 2007.

[72] J. Geisbüsch, R. Kneissl, and M. Hobson. Sunyaev-Zel'dovich cluster survey simulations for Planck. MNRAS, 360:41–59, June 2005.

[73] R. Génova-Santos, F. Atrio-Barandela, J. P. Mücket, and J. S. Klar. The Contribution of the Kinematic Sunyaev-Zel'dovich Effect from the Warm-Hot Intergalactic Medium to the Five-Year Wilkinson Microwave Anisotropy Probe Data. ApJ, 700:447–453, July 2009.

[74] M. Girardi, S. Borgani, G. Giuricin, F. Mardirossian, and M. Mezzetti. The Observational Mass Function of Nearby Galaxy Clusters. ApJ, 506:45–52, October 1998.

[75] J. Glenn, R. Aikin, J. Aguirre, L. Earle, P. Maloney, J. J. Bock, C. M. Bradford, M. Dragovan, H. Nguyen, B. Naylor, J. Zmuidzinas, L. Duband, H. Matsuhara, and P. A. R. Ade. Z-Spec: A Dispersive Millimeter-Wave Spectrometer. In A. J. Baker, J. Glenn, A. I. Harris, J. G. Mangum, & M. S. Yun , editor, *From Z-Machines to ALMA: (Sub)Millimeter Spectroscopy of Galaxies*, volume 375 of *Astronomical Society of the Pacific Conference Series*, pages 63–+, October 2007.

[76] J. Glenn, J. J. Bock, G. Chattopadhyay, S. F. Edgington, A. E. Lange, J. Zmuidzinas, P. D. Mauskopf, B. Rownd, L. Yuen, and P. A. Ade. Bolocam: a millimeter-wave bolometric camera. In T. G. Phillips, editor, *Society of Photo-Optical Instrumentation Engineers (SPIE) Conference Series*, volume 3357 of *Society of Photo-Optical Instrumentation Engineers (SPIE) Conference Series*, pages 326–334, July 1998.

[77] Prof. Sunil Golwala. Private Communication.

[78] G. L. Granato, L. Silva, P. Monaco, P. Panuzzo, P. Salucci, G. De Zotti, and L. Danese. Joint formation of QSOs and spheroids: QSOs as clocks of star formation in spheroids. MNRAS, 324:757–768, June 2001.

[79] G. L. Granato, L. Silva, P. Monaco, P. Panuzzo, P. Salucci, G. De Zotti, and L. Danese. Joint formation of QSOs and spheroids: QSOs as clocks of star formation in spheroids. MNRAS, 324:757–768, June 2001.

[80] L. Grego, J. E. Carlstrom, E. D. Reese, G. P. Holder, W. L. Holzapfel, M. K. Joy, J. J. Mohr, and S. Patel. Galaxy Cluster Gas Mass Fractions from Sunyaev-Zeldovich Effect Measurements: Constraints on Ω_M. ApJ, 552:2–14, May 2001.

[81] S. F. Gull and K. J. E. Northover. Detection of hot gas in clusters of galaxies by observation of the microwave background radiation. Nature, 263:572–+, October 1976.

[82] J. E. Gunn. *Observational Cosmology.* Geneva Observatory, 1978.

[83] H. P. Gush, M. Halpern, and E. H. Wishnow. Rocket measurement of the cosmic-background-radiation mm-wave spectrum. *Physical Review Letters*, 65:537–540, July 1990.

[84] M. G. Haehnelt and M. Tegmark. Using the Kinematic Sunyaev-Zeldovich effect to determine the peculiar velocities of clusters of galaxies. MNRAS, 279:545–+, March 1996.

[85] M. G. Haehnelt and M. Tegmark. Using the Kinematic Sunyaev-Zeldovich effect to determine the peculiar velocities of clusters of galaxies. MNRAS, 279:545–+, March 1996.

[86] E. J. Hallman, J. O. Burns, P. M. Motl, and M. L. Norman. The β-Model Problem: The Incompatibility of X-Ray and Sunyaev-Zeldovich Effect Model Fitting for Galaxy Clusters. ApJ, 665:911–920, August 2007.

[87] S. H. Hansen. SZ cluster science with the Planck HFI experiment. In F. Melchiorri & Y. Rephaeli, editor, *Background Microwave Radiation and Intracluster Cosmology*, pages 199–+, 2005.

[88] D. E. Harris and W. Romanishin. Inverse Compton Radiation and the Magnetic Field in Clusters of Galaxies. ApJ, 188:209–216, March 1974.

[89] F. A. Harrison, S. A. Yost, R. Sari, E. Berger, T. J. G. J. Holtzmann, T. Axelrod, J. S. Bloom, R. Chevalier, E. Costa, A. Diercks, S. G. Djorgovski, D. A. Frail, F. Frontera, K. Hurley, S. R. Kulkarni, P. McCarthy, L. Piro, G. G. Pooley, P. A. Price, D. Reichart, G. R. R. D. Shepard, B. Schmidt, F. Walter, and C. Wheeler. Broadband Observations of the Afterglow of GRB 000926: Observing the Effect of Inverse Compton Scattering and Evidence for a High-Density Environment. *ArXiv Astrophysics e-prints*, March 2001.

[90] C. Hernández-Monteagudo, J. F. Macías-Pérez, M. Tristram, and F.-X. Désert. Spectral indications of thermal Sunyaev-Zel'dovich effect in ARCHEOPS and WMAP data. A&A, 449:41–48, April 2006.

[91] F. W. High, B. Stalder, J. Song, P. A. R. Ade, K. A. Aird, S. S. Allam, R. Armstrong, W. A. Barkhouse, B. A. Benson, E. Bertin, S. Bhattacharya, L. E. Bleem, M. Brodwin, E. J. Buckley-Geer, J. E. Carlstrom, P. Challis, C. L. Chang, T. M. Crawford, A. T. Crites, T. de Haan, S. Desai, M. A. Dobbs, J. P. Dudley, R. J. Foley, E. M. George, M. Gladders, N. W. Halverson, M. Hamuy, S. M. Hansen, G. P. Holder, W. L. Holzapfel, J. D. Hrubes, M. Joy, R. Keisler, A. T. Lee, E. M. Leitch, H. Lin, Y. -. Lin, A. Loehr, M. Lueker, D. Marrone, J. J. McMahon, J. Mehl, S. S. Meyer, J. J. Mohr, T. E. Montroy, N. Morell, C. -. Ngeow, S. Padin, T. Plagge, C. Pryke, C. L.

Reichardt, A. Rest, J. Ruel, J. E. Ruhl, K. K. Schaffer, L. Shaw, E. Shirokoff, R. C. Smith, H. G. Spieler, Z. Staniszewski, A. A. Stark, C. W. Stubbs, D. L. Tucker, K. Vanderlinde, J. D. Vieira, R. Williamson, W. M. Wood-Vasey, Y. Yang, O. Zahn, and A. Zenteno. Optical Redshift and Richness Estimates for Galaxy Clusters Selected with the Sunyaev-Zel'dovich Effect from 2008 South Pole Telescope Observations. *ArXiv e-prints*, March 2010.

[92] A. D. Hincks, V. Acquaviva, P. Ade, P. Aguirre, M. Amiri, J. W. Appel, L. F. Barrientos, E. S. Battistelli, J. R. Bond, B. Brown, B. Burger, J. Chervenak, S. Das, M. J. Devlin, S. Dicker, W. B. Doriese, J. Dunkley, R. Dünner, T. Essinger-Hileman, R. P. Fisher, J. W. Fowler, A. Hajian, M. Halpern, M. Hasselfield, C. Hernández-Monteagudo, G. C. Hilton, M. Hilton, R. Hlozek, K. Huffenberger, D. Hughes, J. P. Hughes, L. Infante, K. D. Irwin, R. Jimenez, J. B. Juin, M. Kaul, J. Klein, A. Kosowsky, J. M. Lau, M. Limon, Y. -. Lin, R. H. Lupton, T. Marriage, D. Marsden, K. Martocci, P. Mauskopf, F. Menanteau, K. Moodley, H. Moseley, C. B. Netterfield, M. D. Niemack, M. R. Nolta, L. A. Page, L. Parker, B. Partridge, H. Quintana, B. Reid, N. Sehgal, J. Sievers, D. N. Spergel, S. T. Staggs, O. Stryzak, D. Swetz, E. Switzer, R. Thornton, H. Trac, C. Tucker, L. Verde, R. Warne, G. Wilson, E. Wollack, and Y. Zhao. The Atacama Cosmology Telescope (ACT): Beam Profiles and First SZ Cluster Maps. *ArXiv e-prints*, July 2009.

[93] G. P. Holder, J. E. Carlstrom, and A. E. Evrard. Combining Interferometric Sunyaev-Zel'dovich Effect Measurements and Weak Lensing. In *Constructing the Universe with Clusters of Galaxies*, 2000.

[94] W. L. Holzapfel, M. Arnaud, P. A. R. Ade, S. E. Church, M. L. Fischer, P. D. Mauskopf, Y. Rephaeli, T. M. Wilbanks, and A. E. Lange. Measurement of the Hubble Constant from X-Ray and 2.1 Millimeter Observations of Abell 2163. ApJ, 480:449–+, May 1997.

[95] W. L. Holzapfel, T. M. Wilbanks, P. A. R. Ade, S. E. Church, M. L. Fischer, P. D. Mauskopf, D. E. Osgood, and A. E. Lange. The Sunyaev-Zeldovich Infrared Experiment: A Millimeter-Wave Receiver for Cluster Cosmology. ApJ, 479:17–+, April 1997.

[96] P. Horner, P. Mauskopf, J. Aguirre, J. Bock, E. Egami, J. Glenn, S. Golwala, G. Laurent, H. Nguyen, and J. Sayers. A high signal to noise ratio map of the Sunyaev-Zel'dovich increment at 1.1 mm wavelength in Abell 1835. *ArXiv e-prints*, May 2010.

[97] F. Hoyle. A New Model for the Expanding Universe. MNRAS, 108:372–+, 1948.

[98] C.-M. Hsu and O. Blaes. Compton Scattering of Polarized Radiation in Two-Phase Accretion Disks in Active Galactic Nuclei. ApJ, 506:658–672, October 1998.

[99] W. Hu. CMB temperature and polarization anisotropy fundamentals. *Annals of Physics*, 303:203–225, January 2003.

[100] W. T. Hu. *Wandering in the Background: a Cosmic Microwave Background Explorer*. PhD thesis, UNIVERSITY OF CALIFORNIA, BERKELEY., January 1995.

[101] E. Hubble. A Relation between Distance and Radial Velocity among Extra-Galactic Nebulae. *Proceedings of the National Academy of Science*, 15:168–173, March 1929.

[102] I. Hubeny, O. Blaes, J. H. Krolik, and E. Agol. Non-LTE Models and Theoretical Spectra of Accretion Disks in Active Galactic Nuclei. IV. Effects of Compton Scattering and Metal Opacities. ApJ, 559:680–702, October 2001.

[103] K. M. Huffenberger, U. Seljak, and A. Makarov. Sunyaev-Zeldovich effect in WMAP and its effect on cosmological parameters. Phys. Rev. D, 70(6):063002–+, September 2004.

[104] J. P. Hughes and M. Birkinshaw. A Measurement of the Hubble Constant from the X-Ray Properties and the Sunyaev-Zeldovich Effect of CL 0016+16. ApJ, 501:1–+, July 1998.

[105] N. Itoh, Y. Kohyama, and S. Nozawa. Relativistic Corrections to the Sunyaev-Zeldovich Effect for Clusters of Galaxies. ApJ, 502:7–+, July 1998.

[106] R. J. Ivison, I. Smail, A. J. Barger, J.-P. Kneib, A. W. Blain, F. N. Owen, T. H. Kerr, and L. L. Cowie. The diversity of SCUBA-selected galaxies. MNRAS, 315:209–222, June 2000.

[107] R. J. Ivison, I. Smail, D. T. Frayer, J.-P. Kneib, and A. W. Blain. Locating the Starburst in the SCUBA Galaxy SMM J14011+0252. ApJ, 561:L45–L49, November 2001.

[108] A. Jenkins, C. S. Frenk, S. D. M. White, J. M. Colberg, S. Cole, A. E. Evrard, H. M. P. Couchman, and N. Yoshida. The mass function of dark matter haloes. MNRAS, 321:372–384, February 2001.

[109] S. M. Jia, Y. Chen, F. J. Lu, L. Chen, and F. Xiang. The analysis of Abell 1835 using a deprojection technique. A&A, 423:65–73, August 2004.

[110] S. Joudaki, J. Smidt, A. Amblard, and A. Cooray. Evidence for a Galactic Sunyaev-Zel'dovich-like Signal in WMAP Data. *ArXiv e-prints*, February 2010.

[111] J. B. Juin, D. Yvon, A. Refregier, and C. Yeche. Cosmology with wide-field SZ cluster surveys: Selection and Systematic Effects. *ArXiv Astrophysics e-prints*, December 2005.

[112] H. Katayama and K. Hayashida. X-ray measurements of the dark matter distribution in clusters of galaxies with Chandra. *Advances in Space Research*, 34:2519–2524, 2004.

[113] H. Kawahara, T. Kitayama, S. Sasaki, and Y. Suto. Systematic Errors in the Hubble Constant Measurement from the Sunyaev-Zel'dovich Effect. ApJ, 674:11–21, February 2008.

[114] J. D. P. Kenney, J. H. van Gorkom, and B. Vollmer. VLA H I Observations of Gas Stripping in the Virgo Cluster Spiral NGC 4522. AJ, 127:3361–3374, June 2004.

[115] I. R. King. The structure of star clusters. III. Some simple dynamical models. AJ, 71:64–+, February 1966.

[116] T. Kitayama, E. Komatsu, N. Ota, T. Kuwabara, Y. Suto, K. Yoshikawa, M. Hattori, and H. Matsuo. Exploring Cluster Physics with High-Resolution Sunyaev–Zel'dovich Effect Images and X-Ray Data: The Case of the Most X-Ray-Luminous Galaxy Cluster RX J1347-1145. PASJ, 56:17–28, February 2004.

[117] K. K. Knudsen, J.-P. Kneib, J. Richard, G. Petitpas, and E. Egami. Physical Properties and Morphology of a Newly Identified Compact z = 4.04 Lensed Submillimeter Galaxy in Abell 2218. ApJ, 709:210–217, January 2010.

[118] J. Ko, M. Im, H. M. Lee, M. G. Lee, R. H. Hopwood, S. Serjeant, I. Smail, H. S. Hwang, N. Hwang, H. Shim, S. J. Kim, J. C. Lee, S. Lim, H. Seo, T. Goto, H. Hanami, H. Matsuhara, T. Takagi, and T. Wada. The Mid-infrared View of Red Sequence Galaxies in Abell 2218 with AKARI. ApJ, 695:L198–L202, April 2009.

[119] E. Komatsu and T. Kitayama. Sunyaev-Zeldovich Fluctuations from Spatial Correlations between Clusters of Galaxies. ApJ, 526:L1–L4, November 1999.

[120] E. Komatsu and U. Seljak. The Sunyaev-Zel'dovich angular power spectrum as a probe of cosmological parameters. MNRAS, 336:1256–1270, November 2002.

[121] A. S. Kompaneets, 1957.

[122] J. Kotoku, K. Makishima, Y. Matsumoto, M. Kohama, Y. Terada, and T. Tamagawa. Effects of Compton Scattering on the Gamma-Ray Spectra of Solar Flares. PASJ, 59:1161–, December 2007.

[123] G. Lake and R. B. Partridge. Microwave search for ionized gas in clusters of galaxies. ApJ, 237:378–389, April 1980.

[124] A. Lapi, A. Cavaliere, and G. De Zotti. Sunyaev-Zel'dovich Effects from Quasars in Galaxies and Groups. ApJ, 597:L93–L96, November 2003.

[125] S. J. LaRoque, M. Bonamente, J. E. Carlstrom, M. K. Joy, D. Nagai, E. D. Reese, and K. S. Dawson. X-Ray and Sunyaev-Zel'dovich Effect Measurements of the Gas Mass Fraction in Galaxy Clusters. ApJ, 652:917–936, December 2006.

[126] G. T. Laurent, J. E. Aguirre, J. Glenn, P. A. R. Ade, J. J. Bock, S. F. Edgington, A. Goldin, S. R. Golwala, D. Haig, A. E. Lange, P. R. Maloney, P. D. Mauskopf, H. Nguyen, P. Rossinot, J. Sayers, and P. Stover. The Bolocam Lockman Hole Millimeter-Wave Galaxy Survey: Galaxy Candidates and Number Counts. ApJ, 623:742–762, April 2005.

[127] A. Levinson and D. Eichler. Polarization of Gamma-Ray Bursts by Scattering off Relativistically Moving Material: Compton Sailing and High Polarization. ApJ, 613:1079–1087, October 2004.

[128] M. Lueker, C. L. Reichardt, K. K. Schaffer, O. Zahn, P. A. R. Ade, K. A. Aird, B. A. Benson, L. E. Bleem, J. E. Carlstrom, C. L. Chang, H.-M. Cho, T. M. Crawford, A. T. Crites, T. de Haan, M. A. Dobbs, E. M. George, N. R. Hall, N. W. Halverson, G. P. Holder, W. L. Holzapfel, J. D. Hrubes, M. Joy, R. Keisler, L. Knox, A. T. Lee, E. M. Leitch, J. J. McMahon, J. Mehl, S. S. Meyer, J. J. Mohr, T. E. Montroy, S. Padin, T. Plagge, C. Pryke, J. E. Ruhl, L. Shaw, E. Shirokoff, H. G. Spieler, B. Stalder, Z. Staniszewski, A. A. Stark, K. Vanderlinde, J. D. Vieira, and R. Williamson. Measurements of Secondary Cosmic Microwave Background Anisotropies with the South Pole Telescope. ApJ, 719:1045–1066, August 2010.

[129] M. Lyutikov and F. P. Gavriil. Resonant cyclotron scattering and Comptonization in neutron star magnetospheres. MNRAS, 368:690–706, May 2006.

[130] M. Machacek, C. Jones, W. R. Forman, and P. Nulsen. Chandra Observations of Gas Stripping in the Elliptical Galaxy NGC 4552 in the Virgo Cluster. ApJ, 644:155–166, June 2006.

[131] S. Majerowicz, D. M. Neumann, and T. H. Reiprich. XMM-NEWTON observation of Abell 1835: Temperature, mass and gas mass fraction profiles. A&A, 394:77–87, October 2002.

[132] B. Malte Schäfer and M. Bartelmann. Detecting Sunyaev-Zel'dovich clusters with Planck - III. Properties of the expected SZ cluster sample. MNRAS, 377:253–268, May 2007.

[133] D. P. Marrone, G. P. Smith, J. Richard, M. Joy, M. Bonamente, N. Hasler, V. Hamilton-Morris, J.-P. Kneib, T. Culverhouse, J. E. Carlstrom, C. Greer, D. Hawkins, R. Hennessy, J. W. Lamb, E. M. Leitch, M. Loh, A. Miller, T. Mroczkowski, S. Muchovej, C. Pryke, M. K. Sharp, and D. Woody. LoCuSS: A Comparison of Sunyaev-Zel'dovich Effect and Gravitational-Lensing Measurements of Galaxy Clusters. ApJ, 701:L114–L118, August 2009.

[134] B. S. Mason, T. J. Pearson, A. C. S. Readhead, M. C. Shepherd, J. Sievers, P. S. Udomprasert, J. K. Cartwright, A. J. Farmer, S. Padin, S. T. Myers, J. R. Bond, C. R. Contaldi, U. Pen, S. Prunet, D. Pogosyan, J. E. Carlstrom, J. Kovac, E. M. Leitch, C. Pryke, N. W. Halverson, W. L. Holzapfel, P. Altamirano, L. Bronfman, S. Casassus, J. May, and M. Joy. The Anisotropy of the Microwave Background to l = 3500: Deep Field Observations with the Cosmic Background Imager. ApJ, 591:540–555, July 2003.

[135] M. Massardi and G. De Zotti. Radio source contamination of the Sunyaev-Zeldovich effect in galaxy clusters. A&A, 424:409–414, September 2004.

[136] J. C. Mather, E. S. Cheng, R. E. Eplee, Jr., R. B. Isaacman, S. S. Meyer, R. A. Shafer, R. Weiss, E. L. Wright, C. L. Bennett, N. W. Boggess, E. Dwek, S. Gulkis, M. G. Hauser, M. Janssen, T. Kelsall, P. M. Lubin, S. H. Moseley, Jr., T. L. Murdock, R. F. Silverberg, G. F. Smoot, and D. T. Wilkinson. A preliminary measurement of the cosmic microwave background spectrum by the Cosmic Background Explorer (COBE) satellite. ApJ, 354:L37–L40, May 1990.

[137] P. D. Mauskopf, P. A. R. Ade, S. W. Allen, S. E. Church, A. C. Edge, K. M. Ganga, W. L. Holzapfel, A. E. Lange, B. K. Rownd, B. J. Philhour, and M. C. Runyan. A Determination of the Hubble Constant Using Measurements of X-Ray Emission and the Sunyaev-Zeldovich Effect at Millimeter Wavelengths in the Cluster Abell 1835. ApJ, 538:505–516, August 2000.

[138] I. G. McCarthy, A. Babul, G. P. Holder, and M. L. Balogh. Cluster Sunyaev-Zeldovich Effect Scaling Relations. ApJ, 591:515–525, July 2003.

[139] K. Moodley, R. Warne, N. Goheer, and H. Trac. Detection of Hot Gas in Galaxy Groups Via the Thermal Sunyaev-Zel'Dovich Effect. ApJ, 697:1392–1409, June 2009.

[140] I. V. Moskalenko, T. A. Porter, and S. W. Digel. Inverse Compton Scattering on Solar Photons, Heliospheric Modulation, and Neutrino Astrophysics. ApJ, 652:L65–L68, November 2006.

[141] P. M. Motl, E. J. Hallman, J. O. Burns, and M. L. Norman. The Integrated Sunyaev-Zeldovich Effect as a Superior Method for Measuring the Mass of Clusters of Galaxies. ApJ, 623:L63–L66, April 2005.

[142] R. F. Mushotzky and C. A. Scharf. The Luminosity-Temperature Relation at z=0.4 for Clusters of Galaxies. ApJ, 482:L13+, June 1997.

[143] A. D. Myers, T. Shanks, P. J. Outram, W. J. Frith, and A. W. Wolfendale. Evidence for an extended Sunyaev-Zel'dovich effect in WMAP data. MNRAS, 347:L67–L72, February 2004.

[144] S. T. Myers, J. E. Baker, A. C. S. Readhead, E. M. Leitch, and T. Herbig. Measurements of the Sunyaev-Zeldovich Effect in the Nearby Clusters A478, A2142, and A2256. ApJ, 485:1–+, August 1997.

[145] D. Nagai. The Impact of Galaxy Formation on the Sunyaev-Zel'dovich Effect of Galaxy Clusters. ApJ, 650:538–549, October 2006.

[146] N. P. H. Nesvadba, M. D. Lehnert, R. Genzel, F. Eisenhauer, A. J. Baker, S. Seitz, R. Davies, D. Lutz, L. Tacconi, M. Tecza, R. Bender, and R. Abuter. Intense Star Formation and Feedback at High Redshift: Spatially Resolved Properties of the z = 2.6 Submillimeter Galaxy SMM J14011+0252. ApJ, 657:725–737, March 2007.

[147] S. Nozawa, N. Itoh, Y. Kawana, and Y. Kohyama. Relativistic Corrections to the Sunyaev-Zeldovich Effect for Clusters of Galaxies. IV. Analytic Fitting Formula for the Numerical Results. ApJ, 536:31–35, June 2000.

[148] S. Nozawa, N. Itoh, and Y. Kohyama. Relativistic Corrections to the Sunyaev-Zeldovich Effect for Clusters of Galaxies. II. Inclusion of Peculiar Velocities. ApJ, 508:17–24, November 1998.

[149] S. Nozawa, N. Itoh, Y. Suda, and Y. Ohhata. An improved formula for the relativistic corrections to the kinematical Sunyaev-Zeldovich effect for clusters of galaxies. *Nuovo Cimento B Serie*, 121:487–500, May 2006.

[150] A. Oemler, A. Dressler, D. Kelson, J. Rigby, B. M. Poggianti, J. Fritz, G. Morrison, and I. Smail. Abell 851 and the Role of Starbursts in Cluster Galaxy Evolution. ApJ, 693:152–173, March 2009.

[151] N. Okabe, M. Takada, K. Umetsu, T. Futamase, and G. P. Smith. LoCuSS: Subaru Weak Lensing Study of 30 Galaxy Clusters. PASJ, 62:811–, June 2010.

[152] S. Padin, Z. Staniszewski, R. Keisler, M. Joy, A. A. Stark, P. A. R. Ade, K. A. Aird, B. A. Benson, L. E. Bleem, J. E. Carlstrom, C. L. Chang, T. M. Crawford, A. T. Crites, M. A. Dobbs, N. W. Halverson, S. Heimsath, R. E. Hills, W. L. Holzapfel, C. Lawrie, A. T. Lee, E. M. Leitch, J. Leong, W. Lu, M. Lueker, J. J. McMahon, S. S. Meyer, J. J. Mohr, T. E. Montroy, T. Plagge, C. Pryke, J. E. Ruhl, K. K. Schaffer, E. Shirokoff, H. G. Spieler, and J. D. Vieira. South Pole Telescope optics. Appl. Opt., 47:4418–+, August 2008.

[153] J. R. Pardo, J. Cernicharo, and E. Serabyn. Atmospheric transmission at microwaves (ATM): an improved model for millimeter/submillimeter applications. *IEEE Transactions on Antennas and Propagation*, 49:1683–1694, December 2001.

[154] Dr E. Pascale, 2009. Private Communication.

[155] R. Pelló, D. Schaerer, J. Richard, J.-F. Le Borgne, and J.-P. Kneib. ISAAC/VLT observations of a lensed galaxy at z = 10.0. A&A, 416:L35–L40, March 2004.

[156] A. A. Penzias and R. W. Wilson. A Measurement of Excess Antenna Temperature at 4080 Mc/s. ApJ, 142:419–421, July 1965.

[157] M. J. Pereira, C. P. Haines, G. P. Smith, E. Egami, S. M. Moran, A. Finoguenov, E. Hardegree-Ullman, N. Okabe, T. Rawle, and M. Rex. LoCuSS: A Herschel view of obscured star formation in Abell 1835. A&A, 518:L40+, July 2010.

[158] M. J. Pereira, C. P. Haines, G. P. Smith, E. Egami, S. M. Moran, A. Finoguenov, E. Hardegree-Ullman, N. Okabe, T. Rawle, and M. Rex. LoCuSS: A Herschel view of obscured star formation in Abell 1835. A&A, 518:L40+, July 2010.

[159] S. Perlmutter, G. Aldering, G. Goldhaber, R. A. Knop, P. Nugent, P. G. Castro, S. Deustua, S. Fabbro, A. Goobar, D. E. Groom, I. M. Hook, A. G. Kim, M. Y. Kim, J. C. Lee, N. J. Nunes, R. Pain, C. R. Pennypacker, R. Quimby, C. Lidman, R. S. Ellis, M. Irwin, R. G. McMahon, P. Ruiz-Lapuente, N. Walton, B. Schaefer, B. J. Boyle, A. V. Filippenko, T. Matheson, A. S. Fruchter, N. Panagia, H. J. M. Newberg, W. J. Couch, and The Supernova Cosmology Project. Measurements of Omega and Lambda from 42 High-Redshift Supernovae. ApJ, 517:565–586, June 1999.

[160] J. R. Peterson, F. B. S. Paerels, J. S. Kaastra, M. Arnaud, T. H. Reiprich, A. C. Fabian, R. F. Mushotzky, J. G. Jernigan, and I. Sakelliou. X-ray imaging-spectroscopy of Abell 1835. A&A, 365:L104–L109, January 2001.

[161] C. Pfrommer, T. A. Enßlin, and C. L. Sarazin. Unveiling the composition of radio plasma bubbles in galaxy clusters with the Sunyaev-Zel'dovich effect. A&A, 430:799–810, February 2005.

[162] A. Pipino and E. Pierpaoli. Signature of cool core in Sunyaev-Zeldovich clusters: a multiwavelength approach. MNRAS, 404:1603–1616, May 2010.

[163] T. Plagge, B. A. Benson, P. A. R. Ade, K. A. Aird, L. E. Bleem, J. E. Carlstrom, C. L. Chang, H.-M. Cho, T. M. Crawford, A. T. Crites, T. de Haan, M. A. Dobbs, E. M. George, N. R. Hall, N. W. Halverson, G. P. Holder, W. L. Holzapfel, J. D. Hrubes, M. Joy, R. Keisler, L. Knox, A. T.

Lee, E. M. Leitch, M. Lueker, D. Marrone, J. J. McMahon, J. Mehl, S. S. Meyer, J. J. Mohr, T. E. Montroy, S. Padin, C. Pryke, C. L. Reichardt, J. E. Ruhl, K. K. Schaffer, L. Shaw, E. Shirokoff, H. G. Spieler, B. Stalder, Z. Staniszewski, A. A. Stark, K. Vanderlinde, J. D. Vieira, R. Williamson, and O. Zahn. Sunyaev-Zel'dovich Cluster Profiles Measured with the South Pole Telescope. ApJ, 716:1118–1135, June 2010.

[164] P. Platania, C. Burigana, G. De Zotti, E. Lazzaro, and M. Bersanelli. Sunyaev-Zel'dovich effect from quasar-driven blast waves. MNRAS, 337:242–246, November 2002.

[165] G. W. Pratt, H. Böhringer, and A. Finoguenov. Further evidence for a merger in Abell 2218 from an XMM-Newton observation. A&A, 433:777–785, April 2005.

[166] W. H. Press and P. Schechter. Formation of Galaxies and Clusters of Galaxies by Self-Similar Gravitational Condensation. ApJ, 187:425–438, February 1974.

[167] G. J. Qiao and W. P. Lin. An inverse Compton scattering (ICS) model of pulsar emission. I. Core and conal emission beams. A&A, 333:172–180, May 1998.

[168] G. J. Qiao, R. X. Xu, J. F. Liu, B. Zhang, and J. L. Han. Recent developments of inverse Compton scattering model of pulsar radio emission. In M. Kramer, N. Wex, & R. Wielebinski, editor, *IAU Colloq. 177: Pulsar Astronomy - 2000 and Beyond*, volume 202 of *Astronomical Society of the Pacific Conference Series*, pages 405–+, 2000.

[169] N. Rahman and S. F. Shandarin. Constraining Cosmological Models by the Cluster Mass Function. ApJ, 550:L121–L124, April 2001.

[170] K. Rakos and J. Schombert. Cluster Populations in Abell 2125 and 2218. AJ, 130:1002–1021, September 2005.

[171] E. D. Reese. Measuring the Hubble Constant with the Sunyaev-Zel'dovich Effect. *Measuring and Modeling the Universe*, pages 138–+, 2004.

[172] E. D. Reese, J. E. Carlstrom, M. Joy, J. J. Mohr, L. Grego, and W. L. Holzapfel. Determining the Cosmic Distance Scale from Interferometric Measurements of the Sunyaev-Zeldovich Effect. ApJ, 581:53–85, December 2002.

[173] E. D. Reese, J. J. Mohr, J. E. Carlstrom, M. Joy, L. Grego, G. P. Holder, W. L. Holzapfel, J. P. Hughes, S. K. Patel, and M. Donahue. Sunyaev-Zeldovich Effect-derived Distances to the High-Redshift Clusters MS 0451.6-0305 and CL 0016+16. ApJ, 533:38–49, April 2000.

[174] A. Refregier, E. Komatsu, D. N. Spergel, and U.-L. Pen. Power spectrum of the Sunyaev-Zel'dovich effect. Phys. Rev. D, 61(12):123001–+, June 2000.

[175] A. Refregier, D. N. Spergel, and T. Herbig. Extragalactic Foregrounds of the Cosmic Microwave Background: Prospects for the MAP Mission. ApJ, 531:31–41, March 2000.

[176] B. A. Reid and D. N. Spergel. Sunyaev-Zel'dovich Effect Signals in Cluster Models. ApJ, 651:643–657, November 2006.

[177] T. H. Reiprich. Gas Temperature Profile of the Medium-Distant Galaxy Cluster Abell 1835 Observed with XMM-Newton. In H. Inoue & H. Kunieda, editor, *New Century of X-ray Astronomy*, volume 251 of *Astronomical Society of the Pacific Conference Series*, pages 480–+, 2001.

[178] Y. Rephaeli. Comptonization Of The Cosmic Microwave Background: The Sunyaev-Zeldovich Effect. ARA&A, 33:541–580, 1995.

[179] Y. Rephaeli. The Sunyaev-Zeldovich Effect and its Cosmological Significance. In M. M. Shapiro, T. Stanev, & J. P. Wefel, editor, *Astrophysical Sources of High Energy Particles and Radiation*, pages 161–+, 2001.

[180] J. Richard, G. P. Smith, J.-P. Kneib, R. S. Ellis, A. J. R. Sanderson, L. Pei, T. A. Targett, D. J. Sand, A. M. Swinbank, H. Dannerbauer, P. Mazzotta, M. Limousin, E. Egami, E. Jullo, V. Hamilton-Morris, and S. M. Moran. LoCuSS: first results from strong-lensing analysis of 20 massive galaxy clusters at z = 0.2. MNRAS, 404:325–349, May 2010.

[181] K. F. Riley, M. P. Hobson, and S. J. Bence. *Mathematical Methods for Physics and Engineering (Second Edition)*. Cambridge University Press, 2002.

[182] K. Rines, M. J. Geller, and A. Diaferio. Comparison of Hectospec Virial Masses with Sunyaev-Zel'Dovich Effect Measurements. ApJ, 715:L180–L184, June 2010.

[183] M. Roncarelli, L. Moscardini, E. Branchini, K. Dolag, M. Grossi, F. Iannuzzi, and S. Matarrese. Imprints of primordial non-Gaussianities in X-ray and SZ signals from galaxy clusters. MNRAS, 402:923–933, February 2010.

[184] D. Rosa-González, R. Terlevich, E. Terlevich, A. Friaça, and E. Gaztañaga. On the detectability of the Sunyaev-Zel'dovich effect of massive young galaxies. MNRAS, 348:669–678, February 2004.

[185] D. H. Rudd and D. Nagai. Nonequilibrium Electrons and the Sunyaev-Zel'Dovich Effect of Galaxy Clusters. ApJ, 701:L16–L19, August 2009.

[186] L. Rudnick. Ionized gas in X-ray clusters of galaxies - Radio limits. ApJ, 223:37–46, July 1978.

[187] J. Ruhl, P. A. R. Ade, J. E. Carlstrom, H.-M. Cho, T. Crawford, M. Dobbs, C. H. Greer, N. w. Halverson, W. L. Holzapfel, T. M. Lanting, A. T. Lee, E. M. Leitch, J. Leong, W. Lu, M. Lueker, J. Mehl, S. S. Meyer, J. J. Mohr, S. Padin, T. Plagge, C. Pryke, M. C. Runyan, D. Schwan, M. K. Sharp, H. Spieler, Z. Staniszewski, and A. A. Stark. The South Pole Telescope. In C. M. Bradford, P. A. R. Ade, J. E. Aguirre, J. J. Bock, M. Dragovan, L. Duband, L. Earle, J. Glenn, H. Matsuhara, B. J. Naylor, H. T. Nguyen, M. Yun, & J. Zmuidzinas, editor, *Society of Photo-Optical Instrumentation Engineers (SPIE) Conference Series*, volume 5498 of *Presented at the Society of Photo-Optical Instrumentation Engineers (SPIE) Conference*, pages 11–29, October 2004.

[188] S. F. Sánchez, N. Cardiel, M. A. W. Verheijen, S. Pedraz, and G. Covone. Morphologies and stellar populations of galaxies in the core of Abell 2218. MNRAS, 376:125–150, March 2007.

[189] S. Y. Sazonov and R. A. Sunyaev. Gas Heating Inside Radio Sources to Mildly Relativistic Temperatures via Induced Compton Scattering. *Astronomy Letters*, 27:481–492, August 2001.

[190] B. M. Schäfer, C. Pfrommer, M. Bartelmann, V. Springel, and L. Hernquist. Detecting Sunyaev-Zel'dovich clusters with Planck - I. Construction of all-sky thermal and kinetic SZ maps. MNRAS, 370:1309–1323, August 2006.

[191] B. M. Schäfer, C. Pfrommer, R. M. Hell, and M. Bartelmann. Detecting Sunyaev-Zel'dovich clusters with Planck - II. Foreground components and optimized filtering schemes. MNRAS, 370:1713–1736, August 2006.

[192] R. W. Schmidt, S. W. Allen, and A. C. Fabian. An improved approach to measuring H_0 using X-ray and SZ observations of galaxy clusters. MNRAS, 352:1413–1420, August 2004.

[193] D. A. Schwartz. The Development and Scientific Impact of the Chandra X-Ray Observatory. *International Journal of Modern Physics D*, 13:1239–1247, 2004.

[194] C. Shang, Z. Haiman, and L. Verde. Probing cosmology and galaxy cluster structure with the Sunyaev-Zel'dovich decrement ver sus X-ray temperature scaling relation. MNRAS, 400:1085–1104, December 2009.

[195] J. Silk and S. D. M. White. The determination of Q_0 using X-ray and microwave observations of galaxy clusters. ApJ, 226:L103–L106, December 1978.

[196] J. B. Skibo, C. D. Dermer, and R. L. Kinzer. Is the high-energy emission from Centaurus A compton-scattered jet radiation? ApJ, 426:L23–L26, May 1994.

[197] J. G. Skibo, C. D. Dermer, and R. Ramaty. Compton scattering in jets: A mechanism for approximately 0.4 and less than or approximately 0.2 MeV line production. ApJ, 431:L39–L42, August 1994.

[198] G. P. Smith, D. J. Sand, E. Egami, D. Stern, and P. R. Eisenhardt. Optical and Infrared Nondetection of the z = 10 Galaxy behind Abell 1835. ApJ, 636:575–581, January 2006.

[199] G. F. Smoot, C. L. Bennett, A. Kogut, E. L. Wright, J. Aymon, N. W. Boggess, E. S. Cheng, G. de Amici, S. Gulkis, M. G. Hauser, G. Hinshaw, P. D. Jackson, M. Janssen, E. Kaita, T. Kelsall, P. Keegstra, C. Lineweaver, K. Loewenstein, P. Lubin, J. Mather, S. S. Meyer, S. H. Moseley, T. Murdock, L. Rokke, R. F. Silverberg, L. Tenorio, R. Weiss, and D. T. Wilkinson. Structure in the COBE differential microwave radiometer first-year maps. ApJ, 396:L1–L5, September 1992.

[200] V. Springel, S. D. M. White, A. Jenkins, C. S. Frenk, N. Yoshida, L. Gao, J. Navarro, R. Thacker, D. Croton, J. Helly, J. A. Peacock, S. Cole, P. Thomas, H. Couchman, A. Evrard, J. Colberg, and F. Pearce. Simulations of the formation, evolution and clustering of galaxies and quasars. Nature, 435:629–636, June 2005.

[201] Z. Staniszewski, P. A. R. Ade, K. A. Aird, B. A. Benson, L. E. Bleem, J. E. Carlstrom, C. L. Chang, H.-M. Cho, T. M. Crawford, A. T. Crites, T. de Haan, M. A. Dobbs, N. W. Halverson, G. P. Holder, W. L. Holzapfel, J. D. Hrubes, M. Joy, R. Keisler, T. M. Lanting, A. T. Lee, E. M. Leitch, A. Loehr, M. Lueker, J. J. McMahon, J. Mehl, S. S. Meyer, J. J. Mohr, T. E. Montroy, C.-C. Ngeow, S. Padin, T. Plagge, C. Pryke, C. L. Reichardt, J. E. Ruhl, K. K. Schaffer, L. Shaw, E. Shirokoff, H. G. Spieler, B. Stalder, A. A. Stark, K. Vanderlinde, J. D. Vieira, O. Zahn, and A. Zenteno. Galaxy Clusters Discovered with a Sunyaev-Zel'dovich Effect Survey. ApJ, 701:32–41, August 2009.

[202] A. Stebbins. The CMBR Spectrum. *ArXiv Astrophysics e-prints*, May 1997.

[203] V. Suleimanov and K. Werner. Importance of Compton scattering for radiation spectra of isolated neutron stars with weak magnetic fields. A&A, 466:661–666, May 2007.

[204] R. A. Sunyaev and Y. B. Zeldovich. Small-Scale Fluctuations of Relic Radiation. Ap&SS, 7:3–19, April 1970.

[205] R. A. Sunyaev and Y. B. Zeldovich. The Observations of Relic Radiation as a Test of the Nature of X-Ray Radiation from the Clusters of Galaxies. *Comments on Astrophysics and Space Physics*, 4:173–+, November 1972.

[206] E. R. Switzer, C. Allen, M. Amiri, J. W. Appel, E. S. Battistelli, B. Burger, J. A. Chervenak, A. J. Dahlen, S. Das, M. J. Devlin, S. R. Dicker, W. B. Doriese, R. Dünner, T. Essinger-Hileman, X. Gao, M. Halpern, M. Hasselfield, G. C. Hilton, A. D. Hincks, K. D. Irwin, S. Knotek, R. P. Fisher, J. W. Fowler, N. Jarosik, M. Kaul, J. Klein, J. M. Lau, M. Limon, R. H. Lupton, T. A. Marriage, K. L. Martocci, S. H. Moseley, C. B. Netterfield, M. D. Niemack, M. R. Nolta, L. Page, L. P. Parker, B. A. Reid, C. D. Reintsema, A. J. Sederberg, J. L. Sievers, D. N. Spergel, S. T. Staggs, O. R. Stryzak, D. S. Swetz, R. J. Thornton, E. J. Wollack, and Y. Zhao. Systems and control software for the Atacama Cosmology Telescope. In *Society of Photo-Optical Instrumentation Engineers (SPIE) Conference Series*, volume 7019 of *Society of Photo-Optical Instrumentation Engineers (SPIE) Conference Series*, August 2008.

[207] R. A. Syunyaev. The microwave background radiation in the direction toward clusters of galaxies. *Pis ma Astronomicheskii Zhurnal*, 6:387–393, August 1980.

[208] K. Takahashi, M. Oguri, and K. Ichiki. Sunyaev-Zel'dovich power spectrum with decaying cold dark matter. MNRAS, 352:311–317, July 2004.

[209] M. Takizawa. Evolution of Hard X-Ray Radiation from Clusters of Galaxies: Bremsstrahlung or Inverse Compton Scattering? PASJ, 54:363–371, June 2002.

[210] G. B. Taylor and E. L. Wright. Effects of a hot intergalactic medium. ApJ, 339:619–628, April 1989.

[211] M. Tecza, A. J. Baker, R. I. Davies, R. Genzel, M. D. Lehnert, F. Eisenhauer, D. Lutz, N. Nesvadba, S. Seitz, L. J. Tacconi, N. A. Thatte, R. Abuter, and R. Bender. SPIFFI Observations of the Starburst SMM J14011+0252:Already Old, Fat, and Rich by z=2.5 65. ApJ, 605:L109–L112, April 2004.

[212] The Planck Collaboration. The Scientific Programme of Planck. *ArXiv Astrophysics e-prints*, April 2006.

[213] K. Tomita. Cluster Abundance Evolution and the Sunyaev-Zeldovich Effect in Various CosmologiModels. *Progress of Theoretical Physics*, 111:1–12, January 2004.

[214] M. Tsuboi, A. Miyazaki, T. Kasuga, H. Matsuo, and N. Kuno. Measurement of the Sunyaev-Zel'dovich Effect toward Abell 2218 at 36GHz. PASJ, 50:169–173, February 1998.

[215] P. S. Udomprasert, B. S. Mason, A. C. S. Readhead, and T. J. Pearson. An Unbiased Measurement of H_0 through Cosmic Background Imager Obser-

vations of the Sunyaev-Zel'dovich Effect in Nearby Galaxy Clusters. ApJ, 615:63–81, November 2004.

[216] J. M. Uson. The Sunyaev-Zel'dovich effect - Measurements and implications. *Radio continuum processes in clusters of galaxies; Proceedings of the Workshop, Green Bank, WV, Aug. 4-8, 1986 (A88-38551 15-90). Charlottesville, VA, National Radio Astronomy Observatory, 1986, p. 255-260.*, 16:255–260, 1986.

[217] J. M. Uson and D. T. Wilkinson. The microwave background radiation, 1988.

[218] R. Šuhada, J. Song, H. Böhringer, B. A. Benson, J. Mohr, R. Fassbender, A. Finoguenov, D. Pierini, G. W. Pratt, K. Andersson, R. Armstrong, and S. Desai. XMM-Newton detection of two clusters of galaxies with strong SPT Sunyaev-Zel'dovich effect signatures. A&A, 514:L3+, May 2010.

[219] M. Veneziani, A. Amblard, A. Cooray, F. Piacentini, D. Pietrobon, P. Serra, P. A. R. Ade, J. J. Bock, J. R. Bond, J. Borrill, A. Boscaleri, P. Cabella, C. R. Contaldi, B. P. Crill, P. de Bernardis, G. DeGasperis, A. de Oliveira-Costa, G. DeTroia, G. Di Stefano, K. M. Ganga, E. Hivon, W. C. Jones, T. S. Kisner, A. E. Lange, C. J. MacTavish, S. Masi, P. D. Mauskopf, A. Melchiorri, T. E. Montroy, P. Natoli, C. B. Netterfield, E. Pascale, G. Polenta, S. Ricciardi, G. Romeo, J. E. Ruhl, P. Santini, M. Tegmark, and N. Vittorio. Subdegree Sunyaev-Zel'dovich Signal from Multifrequency BOOMERANG Observations. ApJ, 702:L61–L65, September 2009.

[220] Y.-G. Wang and Z.-H. Fan. Systematic Errors in the Determination of Hubble Constant due to the Asphericity and Nonisothermality of Clusters of Galaxies. ApJ, 643:630–640, June 2006.

[221] D. M. Wei and T. Lu. The influence of inverse Compton scattering on GRB afterglows: one possible way to flatten and steepen the light curves. A&A, 360:L13–L16, August 2000.

[222] J. Weller, R. A. Battye, and R. Kneissl. Constraining Dark Energy with Sunyaev-Zel'dovich Cluster Surveys. *Physical Review Letters*, 88(23):231301–+, June 2002.

[223] D. A. White. Deconvolution of ASCA X-ray data - II. Radial temperature and metallicity profiles for 106 galaxy clusters. MNRAS, 312:663–688, March 2000.

[224] M. White. Cosmological science enabled by Planck. *New Astronomy Review*, 50:938–944, December 2006.

[225] D. R. Wik, C. L. Sarazin, P. M. Ricker, and S. W. Randall. The Impact of Galaxy Cluster Mergers on Cosmological Parameter Estimation from Surveys of the Sunyaev-Zel'dovich Effect. ApJ, 680:17–31, June 2008.

[226] E. L. Wright. Distortion of the microwave background by a hot intergalactic medium. ApJ, 232:348–351, September 1979.

[227] J.-Q. Xia, H. Li, G.-B. Zhao, and X. Zhang. Probing for the Cosmological Parameters with Planck Measurement. *International Journal of Modern Physics D*, 17:2025–2048, 2008.

[228] R. X. Xu, J. F. Liu, J. L. Han, and G. J. Qiao. An Inverse Compton Scattering Model of Pulsar Emission. III. Polarization. ApJ, 535:354–364, May 2000.

[229] K. Yoshikawa, M. Itoh, and Y. Suto. Hydrodynamical Simulation of Clusters of Galaxies in X-Ray, mm, and submm Bands: Determination of Peculiar Velocity and the Hubble Constant. PASJ, 50:203–211, April 1998.

[230] Q. Yuan, H.-Y. Wan, T.-J. Zhang, J.-R. Liu, L.-L. Feng, and L.-Z. Fang. Scaling relation between Sunyaev Zeldovich effect and X-ray luminosity and scale-free evolution of cosmic baryon field. *New Astronomy*, 14:152–159, February 2009.

[231] M. Zaldarriaga. The Polarization of the Cosmic Microwave Background. *Measuring and Modeling the Universe*, pages 309–+, 2004.

[232] M. Zemcov, C. Borys, M. Halpern, P. Mauskopf, and D. Scott. A study of the Sunyaev-Zel'dovich increment using archival SCUBA data. MNRAS, 376:1073–1098, April 2007.

[233] P. Zhang. Dimming of Supernovae and Gamma-Ray Busts by Compton Scattering and Its Cosmological Implications. ApJ, 682:721–723, August 2008.